University of Salford

School of Science, Engineering and Environment

A Study of the Polarimetric Characteristics of Planar Chiral Mesoscopic Structures

Huda Atiah M. Alzahrani

Submitted in Partial Fulfilment of the Requirement of the Degree of

Doctor of Philosophy

March 2021

Contents

List of Figures

List of Tables

Table of Symbols

Symbols	Definition
PEM	The photoelastic modulator
2D, 3D	Two-dimensional, three-dimensional
E	Electric field vector
E_0	Electric field amplitude
t	Time
ω	The angular frequency ($\omega = 2\pi f$)
δ	The retardation phase produced by the PEM
k	The wavenumber ($k = 2\pi/\lambda$)
J	Jones Matrix
I, Q, U, V	Stokes parameters
I	The total light intensity ($I = E^2/c\mu_0$)
I_θ	The light intensity when the linear polariser at θ^0
I_R	The intensity of right polarised components
I_L	The intensity of left polarised components
I_p	The intensity of the polarised component
I_{dp}	The intensity of the depolarised component
DOP	The degree of polarisation
DOLP	The degree of linear polarisation
DOCP	The degree of circular polarisation
Ψ	Azimuth angle
e	ellipticity
χ	The ellipticity angle
ϵ	Eccentricity
S	Stokes vector
M	Mueller matrix
D	The electric displacement
B	The magnetic induction

H	Magnetic field vector
ε_0	The permittivity of free space, electric constant $= 8.8541878 \times 10^{-12}$ F/m
μ_0	Permeability of free space, magnetic constant $= 4\pi \times 10^{-7}$ N/A^2
K	Chirality index
R, T	reflection and transmission matrices for a linear polariser
PSG	polarisation state generator
PSA	polarisation state analyser
WP	wave plate
HWP	half-wave plate
QWP	quarter-wave plate
Δn	birefringence
$M_{analyser}$	Müller matrix for the analyser
M_{PEM}	Müller matrix for the PEM
Ω	The modulating frequency
α	The angle between the fast axis of the PEM and the x-axis
β	The angle between the passing axis of the analyser and the x-axis.
C_{LMS}	Clockwise ordering of Large, Medium, and Small sides of a triangle
A_{LMS}	Anticlockwise ordering of Large, Medium, and Small sides of a triangle
ai, aj, ak	The lengths of the triangle's sides
θi, θj, θk	The triangle's angles
Δ	The triangle's area
r	The ratio between two sides of a triangle
L	The arm length of the gammadion shape
q, u, v	Normalised Stokes parameters

Acknowledgements

First and foremost, I would like to praise the Almighty God for His blessing throughout all of my life.

I would like to express my sincere gratitude and deep appreciation to my supervisor, Dr Tiehan Shen, for his constant feedback and help. He directed me to pursue different scientific ideas and encouraged me until I got to this stage. I am incredibly grateful for his kindness and the creation of a pleasant atmosphere during scientific discussions. Many thanks for his willingness to solve all sorts of issues, including personal problems which sometimes became more complex than the research. He is one of the most ambitious people I have ever met.

I am also grateful to Dr Grenville Jones for their insightful contributions to our research. On many occasions, he expanded my perspective, directing me toward more rewarding directions. This served to improve my work to a considerable extent. He influenced my thinking in relation to different points which I was previously unaware of.

Thanks for all the friendly discussions and helpfulness to my friends Jorge L. Ramos Angulo and Jie Gou. Without them, some areas of my studies would have been difficult. Thank you for your patience in helping me to conduct the microscopic experiments and generously sharing their experience with me. It was a pleasure to work together as a team.

Additionally, I would like to acknowledge Prof. W.X. Lu, Prof. C.Z Gu and their research team at the Institute of Physics, Chinese Academy of Sciences, Beijing, China, for fabrication of the 2D mesoscopic chiral patterned samples. Also, My acknowledgements to Dr Zeljka Krpetic for providing the gold and copper nanoparticles.

Many thanks to the University of Salford for providing a supportive environment and essential services to students. In particular, during the COVID-19 pandemic, they launched various resources designed to support the students' learning and training activities.

Dedication

With love and gratitude, this for my husband Ahmad.

Abstract

Previous work has shown that chiral materials can change the state of polarisation of incident light. The focus of this current work is thus to explore new ways of investigating the polarisation response of mesoscopic structures, with a focus on chiral metamaterial structures and nanoparticles.

In the theoretical part of this work, fundamental concepts related to chirality are thus defined. Previous studies on the quantifying chirality of planar patterns are reviewed. The prospects of developing different expressions based on triangle models are consequently highlighted.

A dual photoelastic modulator polarimeter, incorporating the lock-in amplifier technique, was used to measure the polarisation states of light. Subsequently, these polarisation states were mathematically analysed using Stokes parameters and Mueller matrices. This technique allowed to quantify the full polarisation state of light, including the intensity of both the polarised component and the depolarised component, the degree of polarisation, the degree of linear polarisation, the degree of circular polarisation, the polarisation orientation, and the ellipticity angle.

Furthermore, a dual photo elastic modulator-based Stokes polarimetric microscope developed in the laboratory undertaking the current work was then used to study the polarisation states locally at the sample surface. This polarimetric imaging system provided quantitative measurements of the four Stokes parameters for each pixel and hence enabling the determination of the full range of polarisation states across the focusing plane. The polarimetric imaging performed by the microscope was automated by using Laboratory Virtual Instrument Engineering Workbench (LabView) 'virtual instrument' (vi) codes. In addition, relevant algorithms written in Python were used for analysing the collected data from both the calibration process and the sample measurements.

The Stokes polarimetric microscopy is applicable to a wide variety of material studies and provides insights information about the structure of various samples. Based on the experimental investigations by using the polarimetric microscope in transmission mode, the results of several selected samples are thus presented: (i) chiral

metamaterials; (ii) achiral metamaterials; (iii) copper nanoparticles; and (iv) gold nanoparticles. In general, the results show good ability for the dual photoelastic modulator based polarimetric microscope in terms of exploring the polarisation characteristics of light at the sample surface by means of the measurements of relevant Stokes parameters.

The polarisation characteristics of the Fraunhofer diffractions of mesoscopic structures were also further explored within the context of Fourier optics. Preliminary results suggested that a combination of the mapping of the Stokes parameters at the surface of the mesoscopic structures and subsequent Fourier analysis may offer a new and an alternative technique for the study of the polarisation signatures of the diffracted light beams, making it possible for high throughput polarisation characterisations to be developed.

1   Introduction

Planar chiral metamaterials are a particular class of metamaterials created from artificial arrays of the same chiral pattern in two dimensions. A chiral pattern is defined as a pattern that cannot be superimposed congruently on its mirror image under any possible rotation or translation operation.

The primary aim of the current work is to investigate the effects of planar chiral metamaterial structures on the polarisation state of light travelling through them by applying polarimetry; the general characterisation technique of the polarisation state measurements. The polarised light and its resultant propagation through matter can be represented by Mueller-Stokes formalism. In this work, a polarimetric microscope based on a dual-photoelastic modulator (PEM) was used to acquire the four Stokes parameters in the form of images.

The present research is largely motivated by the earlier work of Potts, Bagnall, and Zheludev (2003) on the construction of a mathematical function to measure the chirality of planar structures. Initially, considerable effort was focused on the investigation of different models that quantify such chirality. However, polarimetric microscopy was observed to be more attractive in the long term due to its potential importance in determining the optical properties of various samples. In this way, the polarimetric microscope was used to measure Stokes parameters as a way to study polarisation variations of light beams transmitted through planar chiral materials.

The Stokes parameters are sets of four intensities and intensity differences; hence, optical imaging theories must be expected to be applicable to them. For example, it is well known that the Fraunhofer diffraction effect of an aperture may be explored by developing the Fourier transform of the aperture function (Goodman, 2005). Therefore, the application of a Fourier transform to the Stokes parameters images of the specimen may similarly enable evaluation of the polarisation characteristics of the Fraunhofer diffractions of chiral pattern arrays.

This thesis is organised into seven chapters. Following this introduction, Chapter Two describes the theoretical background underlying the concept of chirality, including

a literature review of quantification of the chirality and offer a brief introduction to metamaterials.

Chapter Three then provides an overview of the relevant theoretical principles of light, including the idea behind Jones calculus, Stokes parameters, and Mueller matrices. Moreover, a basic overview of the Poincare Sphere is also offered.

The optical properties of chiral materials are presented in Chapter Four along with some of the basic concepts about light polarisation and its propagation in chiral media. The principles of light-matter interaction with planar chiral metamaterials, including optical activity, dichroism, and birefringence, are described.

Chapter Five is devoted to describing the experimental methodologies used to study the samples in the current work. The instruments that required to build a dual photoelastic modulator polarimeter are thus introduced. Some aspects of the calibration procedures are discussed. Then, the chapter explains the process of adapting a light microscope to act as a polarimetric microscope.

Chapter Six focuses on the simulation results obtained by using MATLAB to compare four different theoretical models that quantify the chirality of planar shapes. The limitations of these expressions are then highlighted. Using these models, the chirality indices of gammadion patterns were calculated.

The last chapter, Chapter Seven, presents the main outcomes of the related experimental work. It discusses the investigation of the polarisation response of planar chiral metamaterials fabricated in various gammadion shapes. In addition, the measurements of nanoparticles fabricated in gold and copper are offered. Preliminary work on the application of Fourier analysis suggests that such steps are likely to open up new methods for evaluating the polarisation characteristics in the diffraction of the chiral pattern arrays.

I believe that this work introduces a degree of novelty in two aspects: quantifying chirality and examining the use of Stokes polarimetry microscopy to study planar structures. Furthermore, this research offered opportunities for several professional and personal improvements for a researcher, based on the acquisition and application of various new skills during the PhD journey. From my respective point of

view, the most essential skill that has already improved is programming in both MATLAB and Python.

2   Chirality

A great deal of effort has been made into quantifying chirality based on its status as a significant parameter since most natural materials possess chiral characteristics. Of Greek origin, the term 'chiral' means 'hand', which is the most well-known chiral objects, as it exists in clear left and right 'mirror' versions. Chiral material can basically be described as a substance that cannot be superimposed congruently on its mirror image under any rotation or translation operation. Any chiral material and its reflected form are both known as enantiomers, which is also derived from another Greek word, meaning 'the opposite' (Brandt, Salerno, and Fuchter, 2017; Schwanecke, 2009). Figure 2-1 below illustrates the chemical structure of two molecules of the amino acid alanine, which serve as an example of enantiomers.
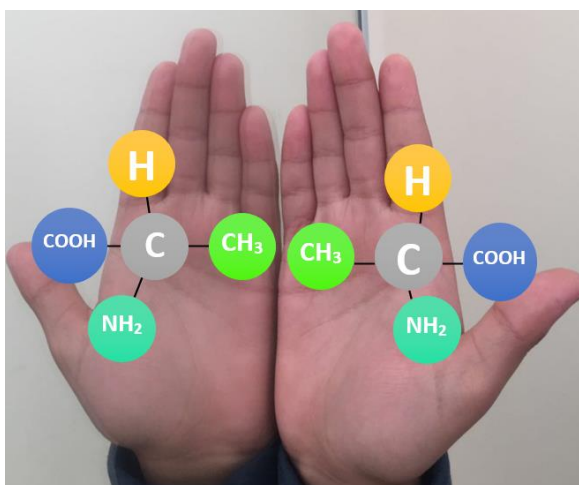
Figure 2-1: Two molecules of the amino acid alanine considered as enantiomers

Enantiomers behave differently under the same physical conditions in certain circumstances, despite having almost identical chemical and physical properties, such as chemical formula, density, and weight. For example, enantiomers of several specific chiral drugs must be viewed and treated as two distinct drugs, as one enantiomer may be biologically active while the other is inactive, such as ibuprofen (Brooks, Guida, and Daniel, 2011; McConathy and Owens, 2003; Wang, Cheng, Winsor, and Liu, 2016). Another example is seen in the interactions with light for some enantiomeric (left-right) forms of chiral structures, yielding different polarisation changes (Papakostas *et al.*, 2003; Zhang, Potts, and Bagnall, 2006).

These behavioural deviations have significant ramifications for several scientific fields, including chemistry, physics, biology, and pharmacology. Therefore, it is crucial to conduct more studies that facilitate the acquisition of high-quality knowledge and understanding of chirality. Such knowledge should make valuable contributions to the development of the materials industry, particularly where chirality is critical to optical applications.

2.1 Handedness

Quantitative approaches have frequently been used to measure chirality, while qualitative methods have been employed to ascertain the 'handedness' of various structures. The term 'handedness' stems from the root hand, and it is the characteristic of chirality in which each enantiomer can be classified as being either one of two versions: left-handed or right-handed, as depicted below in Figure 2-2. The underlying theory of handedness can best be explained in terms of the concept of molecule parity (Potts, 2003).
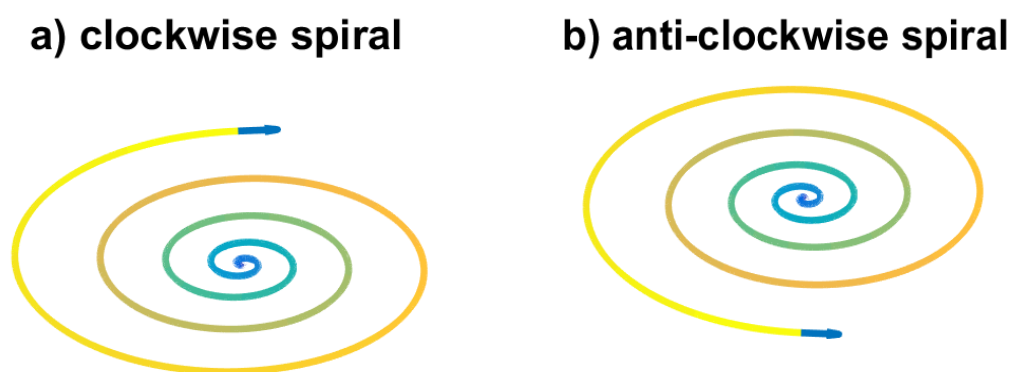
Figure 2-2: Two enantiomer spirals. a) clockwise spiral; b) anticlockwise spiral. (the figure code is in Appendix A-1)

It is sensible to classify objects as chiral or non-chiral based on the presence of symmetry. At the same time, more comprehensive approaches are available for categorising particular chiral objects (e.g., shoes, gloves, screws, and spirals) as either left- or right-handed, according to an acceptable definition. Taking the spirals in Figure 2-2 as an example: if we start from the centre of the spiral, the spiral in Figure 2-2a is a clockwise spiral and can be considered as a right-handed spiral; hence, the anticlockwise spiral in Figure 2-2b is the left-handed form.

However, there is no acceptable method of categorising the majority of chiral objects (e.g., stones, potatoes, and shells) as right- or left-handed (Fowler and Rassat, 2006). A series of theoretical rules have been proposed for defining the handedness of a structure, but these almost are only applicable to certain structures and not necessarily to others. Numerous studies have examined handedness with regard to metamaterials and natural materials both theoretically and experimentally (Schwanecke, 2009).

2.2 **Previous Research**

Osipov, Pickup, Fehervari, and Dunmur (1998) proposed a theoretical applicable chirality expression. By considering a triangle as the simplest 2D form, this expression could be used to numerically calculate the chirality index of 2D chiral structure based on the position and arrangement of three points. Subsequently, the chirality index of any structure could be thus obtained by dividing the structure into points and summing up the chirality index of each set of three points. A chirality index should vanish for achiral structures while possessing the same value with opposite signs for each pair of chiral enantiomers. Similarly, a tetrahedron is the most basic 3D structure, consisting of four triangles. So, the chirality index thereby can be measured in either two or three dimensions based on a similar approach (Boruhovich, 2006; Osipov, Pickup, Fehervari, and Dunmur, 1998).

Similar to Osipov *et al.* methodology, Potts, Bagnall, and Zheludev (2003) offset certain conditions for constructing the chirality index for a triangular form. They then used three different models to calculate the antisymmetric area (i.e. the difference in areas) when a triangle was placed above its mirror-image form. One of these models (the angular bisection model) was the only model, out of the three employed models, found to satisfy all of their required conditions (Potts *et al.*, 2003). A theoretical attempt to extend their models to larger systems was performed using a gammadion-shaped object with four-fold rotational symmetry. They evaluated their theoretical study by conducting experiments on different gammadion-shaped samples to calculate the polarisation rotation. Eventually, they claimed that the experimental results supported their theoretical results (Papakostas *et al.*, 2003; Potts *et al.*, 2002; Zhang *et al.*, 2006).

In order to explore the behaviour of planar chiral materials, several empirical examinations of gammadion-shaped samples were undertaken by Zhang *et al.* (2005,

2006). These demonstrated that when both sides of a planar structure are illuminated, the polarisation rotation of one side is opposite in handedness to that of the other side. Zhang *et al.* (2005, 2006) additionally claimed that the polarisation-changing properties of the dielectric planar chiral metamaterial in transmission were similar to those of the metallic planar chiral metamaterial in reflection (Zhang *et al.*, 2006).

In line with the above-mentioned studies, Fedotov *et al.* (2006) conducted experimental research on a fish-scale structure. Their findings showed that there was greater transparency on one of the planar chiral structure sides under a circularly polarised light than the other. Similarly, when examining the Faraday Effect, the rotation of the elliptically polarised states is reversed when the light propagates through both sides of a planar structure. However, these phenomena are not observable in achiral planar or bulk materials (Fedotov *et al.*, 2006).

During the last decade, the optical properties of several different planar chiral metamaterial structures have been studied, such as: U-shaped (Li *et al.*, 2010), two cross-wires (Li, Alici, Colak, and Ozbay, 2011), G-shaped (Valev *et al.,* 2011), Z-shaped (Kim *et al.*, 2014), nanorods (Wen *et al.*, 2015), L-shaped (Ye *et al.*, 2017), split ring structure (Huang *et al.*, 2017), and spiral structure (Zhao and Cheng, 2018) T-L-shaped (Zhou et al., 2020).

2.3   Metamaterials

An artificially structured material engineered to produce specific properties that do not exist in nature is known as a metamaterial. This technique gives unlimited freedom to engineer different designs of materials with unique features. Typically, metamaterials are periodic arrays. Planar metamaterials (metasurfaces) are defined as two-dimensional surfaces with almost zero thickness. The thickness is sufficiently small to guarantee that the material pattern presented to the light is essentially two-dimensional. Planar metamaterials can display birefringence and dichroism when they do not have any mirror symmetry plane, i.e., chiral shape. Due to their unique properties, metamaterials have attracted the interest of researchers from a variety of disciplines, particularly engineering and material science (Ma *et al.*, 2017; Plum, 2010; Wang *et al.*, 2016).

2.4 Mathematical Quantitative Measurement of Chirality

In terms of the quantitative measurement of chirality, two essential methodologies have emerged, with selection depending on the object used as a reference (Potts *et al.*, 2003).

The first method involves comparing the chiral object to its closest achiral form. In principle, when employing this method, the most challenging step is determining how to generate the closest achiral form.

The second method involves comparing the chiral object with its mirror image in order to determine their similarities. The general requirement is achieved via spatial reflection through a hyperplane, with enantiomeric transformation for an n-dimensional object performed using an (n-1)-dimensional hyperplane. Generation of the mirror image form for a two-dimensional object simply requires a reflection transformation operation through any line in the plane (Potts *et al.*, 2003).

Quantification of chirality is then based on two different parameters though these are related to each other, namely, the chirality index and the degree of chirality. The chirality index is a parameter that defines the quantity of chirality and its handedness in the interval [-1, 1]. Its value is pseudoscalar, meaning that it takes values with different signs for the object and its enantiomer; thus, if the chirality index of an object is c, then the chirality index of its mirror image must be –c (Boruhovich, 2006; Petitjean, 2003; Potts *et al.*, 2003).

Meanwhile, the degree of chirality is then defined as the absolute value of the relevant chirality index. Fundamentally, this identifies the quantity of existent chirality, which increases as the symmetry decreases. Hence, both the object and its enantiomer have the same degree of chirality measured within the interval [0, 1] (Fowler, 2005).

Both the chirality index and the degree of chirality must satisfy the following conditions (Boruhovich, 2006; Potts *et al.*, 2003):

1- Lack of dependence on which specific form (right- or left-version) is selected to generate the corresponding mirror image.

2- Lack of susceptibility to any translation or rotation operation of the object.

3- A value of zero only if the object is achiral (non-chiral).

4- Non-linear secularity such that, when a structure is divided into N sub-objects, the chirality of the initial structure is not necessarily simply the summation of the chirality of those N sub-objects, as an extra chirality may be, and generally is, caused by the arrangement of each N sub-objects within the final structure.

To develop an understanding of the last condition, consider the chiral shape shown in Figure 2-3, which consists of two achiral objects in a rectangular form. The value of the chirality index of the chiral shape is different from zero, even though the value of the chirality index of each of the rectangular shapes must be zero, as these are themselves achiral shapes.

Figure 2-3: A chiral structure consisting of two achiral objects in a rectangular shape.

3   Algebraic Description of Polarised Light

As known, light is electromagnetic waves that composed of coupled oscillating electric and magnetic fields. These fields oscillate perpendicular to each other and perpendicular to the propagation direction. When the electric field oscillates in a specific direction, the light is known as polarised light. The electric field could oscillate in a single direction drawing a line, which known as linear polarised light; rotate at constant rate drawing circle; or ellipse, which results in circular, or elliptical polarised light, see Figure 3-1 (Peatross, and Ware, 2011).
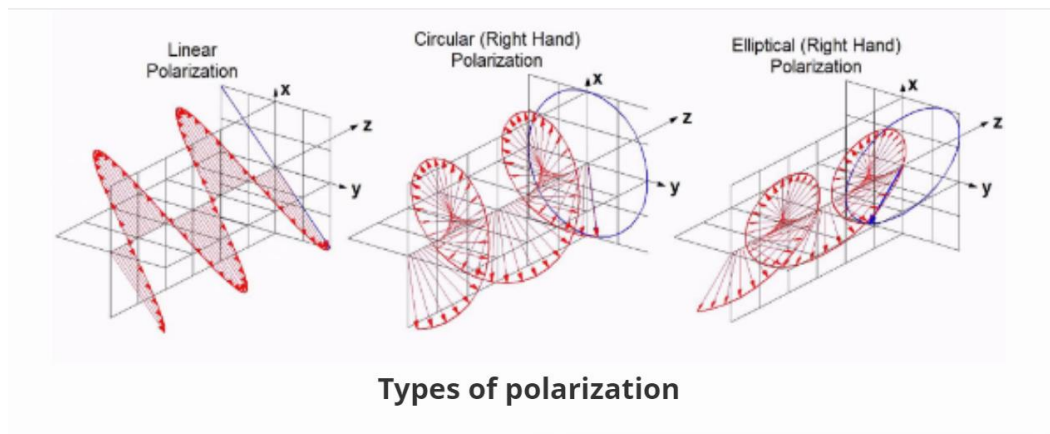
Figure 3-1: polarization types: linear, circular, and elliptical polarised light (emedicalprep.com).

3.1   The Plane Wave

For simplicity, we assume that an electromagnetic wave is travelling as a plane wave where the electric field **E** propagates in **z**-direction while oscillating in **x-y** directions. Accordingly, we could write the electric field of the plane wave equation as (Trippe, 2014):

$$\boldsymbol{E}(z,t) = \widehat{\boldsymbol{x}}\, E_x(z,t) + \widehat{\boldsymbol{y}} E_y(z,t) \tag{3-1}$$

The fields $E_x(z, t)$ and $E_y(z, t)$ are given by the real part of a complex field as:

$$E_x(z,t) = Re\{E_{x0}\, e^{i(\omega t - kz + \delta_x)}\} \tag{3-2}$$

$$E_y(z,t) = Re\{E_{y0}\, e^{i(\omega t - kz + \delta_y)}\} \tag{3-3}$$

where ω is the angular frequency, k is the wavenumber, and factors δx and δy indicate phase shift in **x**- and **y**-direction, respectively.

The electric field direction defines the direction of polarisation. The phase difference between E_x and E_y and the values of the amplitudes E_{x0} and E_{y0} determine the polarisation state of the wave, namely, linear, elliptical, or circular polarisation (see section 4.1 for more details).

3.2   **Jones Calculus**

Developed by R. Clark Jones in 1941, the Jones calculus is a two-dimensional matrix algebra that is applicable only to fully polarised light, with the light being represented by a vector, while optical elements are represented by 2D matrices. For plane wave travelling in the **z**-direction, the Jones vector is written as (Sharma, 2006):

$$\boldsymbol{E} = \begin{bmatrix} E_x \\ E_y \end{bmatrix} = \begin{bmatrix} E_{xo}e^{i\delta_x} \\ E_{yo}e^{i\delta_y} \end{bmatrix} \tag{3-4}$$

For the sake of simplicity, Jones matrices could be normalised to 1 at the initial calculation. Therefore, special cases of polarised light are given by (Sharma, 2006):

$$\boldsymbol{e_H} = \begin{bmatrix} 1 \\ 0 \end{bmatrix}; \quad \boldsymbol{e_V} = \begin{bmatrix} 0 \\ 1 \end{bmatrix}; \quad \boldsymbol{e_{+45°}} = \frac{1}{\sqrt{2}} \begin{bmatrix} 1 \\ 1 \end{bmatrix}; \quad \boldsymbol{e_L} = \frac{1}{\sqrt{2}} \begin{bmatrix} 1 \\ i \end{bmatrix}; \quad \boldsymbol{e_R} = \frac{1}{\sqrt{2}} \begin{bmatrix} 1 \\ -i \end{bmatrix} \tag{3-5}$$

where $\boldsymbol{e_H}$ and $\boldsymbol{e_V}$ denote linear polarised light in **x** and **y** direction, respectively; $\boldsymbol{e_{+45°}}$ denotes linear polarised light at 45° to **x**-direction; while $\boldsymbol{e_L}$ and $\boldsymbol{e_R}$ denote left-hand and right-hand circular polarised light, respectively. It can be noticed that these vectors contain essential information about the polarisation state. They characterise the amplitude and the phase of the two components of the electric field in both directions **x** and **y**. Hence, the intensity of the light will be the sum of the squares of the absolute values of the electric field components.

The effects of the optical elements on the light can be represented as a 2D matrix. The following are simple examples of normalised Jones matrices of special cases of linear polariser (Sharma, 2006):

$$\boldsymbol{J_H} = \begin{bmatrix} 1 & 0 \\ 0 & 0 \end{bmatrix}; \quad \boldsymbol{J_V} = \begin{bmatrix} 0 & 0 \\ 0 & 1 \end{bmatrix}; \quad \boldsymbol{J_{+45°}} = \frac{1}{2} \begin{bmatrix} 1 & 1 \\ 1 & 1 \end{bmatrix} \tag{3-6}$$

where **J_H**, **J_V**, and **J_{+45}°** describe a linear polariser with the transmission axis along the **x**-axis, **y**-axis, and at 45° to the **x**-axis, respectively. Table 3-1 summarises Jones Matrices of a polariser and wave plates at arbitrary angles θ (Peatross, and Ware 2011).

Table 3-1: Jones Matrices for the polariser and wave plates, where ξ is a parameter that signifies a general retarder's expression.

The retarder	ξ value	Jones Matrix
General retarder	ξ	$\begin{bmatrix} \cos^2\theta + \xi\sin^2\theta & \sin\theta\cos\theta - \xi\sin\theta\cos\theta \\ \sin\theta\cos\theta - \xi\sin\theta\cos\theta & \sin^2\theta + \xi\cos^2\theta \end{bmatrix}$
No component	1	$\begin{bmatrix} 1 & 0 \\ 0 & 1 \end{bmatrix}$
Polariser	0	$\begin{bmatrix} \cos^2\theta & \sin\theta\cos\theta \\ \sin\theta\cos\theta & \sin^2\theta \end{bmatrix}$
Quarter-wave plate	i	$\begin{bmatrix} \cos^2\theta + i\sin^2\theta & \sin\theta\cos\theta - i\sin\theta\cos\theta \\ \sin\theta\cos\theta - i\sin\theta\cos\theta & \sin^2\theta + i\cos^2\theta \end{bmatrix}$
Have- wave plate	-1	$\begin{bmatrix} \cos2\theta & \sin2\theta \\ \sin2\theta & -\cos2\theta \end{bmatrix}$

Indeed, Jones calculus has the power to explain how light behaves when it interacts with different components by calculating the product of Jones matrix of the light by Jones matrices of the components in the system to obtain the Jones matrix representing the total effects of the compound system.

3.3 Stokes Parameters

In 1852, George Gabriel Stokes introduced a unique set of four real values, namely, I, Q, U, and V, which have become known as Stokes parameters and depend on the light wavelength, position, and direction. They can represent any given polarisation state mathematically as (Born and Wolf, 1999):

$$S = \begin{bmatrix} I \\ Q \\ U \\ V \end{bmatrix} = \begin{bmatrix} \langle E_x E_x^* \rangle + \langle E_y E_y^* \rangle \\ \langle E_x E_x^* \rangle - \langle E_y E_y^* \rangle \\ \langle E_x E_y^* \rangle + \langle E_y E_x^* \rangle \\ -i[\langle E_x E_y^* \rangle - \langle E_y E_x^* \rangle] \end{bmatrix} \tag{3-7}$$

Where **S** is a stokes vector compound of the four parameters: I corresponds to the total intensity of the whole wave; Q is a parameter of the difference between the

intensities of the linear polarised light in the **x** and **y**-axis (horizontal and vertical polarised light); U is a parameter of the difference between the two diagonal components at angles of ±45° to the positive **x**-axis; V is a parameter that corresponds to the difference between the intensity of the right and the left circular polarised light. Thus, Q and U provide information about linear polarisation, while V is related to circular polarisation states. The sign <...> denotes the time average of the enclosed parameters (in this case, the electric field of the **x**-axis and the **y**-axis), and (*) indicates the complex conjugate of the quantity.

For experimental purposes, the Stokes parameters can be expressed with the light intensity in the following way:

$$\begin{bmatrix} I \\ Q \\ U \\ V \end{bmatrix} = \begin{bmatrix} I_{0°} + I_{90°} = I_{+45°} + I_{-45°} = I_R + I_L \\ I_{0°} - I_{90°} \\ I_{+45°} - I_{-45°} \\ I_R - I_L \end{bmatrix} \tag{3-8}$$

where I_θ is the light intensity when the linear polariser at θ° (where θ°= 0°, 90°, ±45°), while I_R and I_L are the intensities of right and left circularly polarised components, respectively (Guan, Cook, Jones, and Shen, 2010; Hecht, 2002; Liu, 2005).

It is also possible to define the Stokes parameters in terms of the intensity of polarised light performing with an ideal polariser as following:

$$\begin{bmatrix} I \\ Q \\ U \\ V \end{bmatrix} = \begin{bmatrix} P_H + P_V \\ P_H - P_V \\ P_{45°} - P_{-45°} \\ P_R - P_L \end{bmatrix} \tag{3-9}$$

P_H, P_V, and $P_{±45°}$ are the light intensities resulting from the passing of the light through a horizontal, vertical, and diagonal linear polariser with the axis at 0°, 90°, and ±45°, respectively. P_R and P_L denote the light intensities resulting from the passing of the light through a right and left circular polariser, respectively (Bass, 1995). Table 3-2 summarises the category of polarisation states based on Stokes parameters.

Table 3-2: Categorisation of Stokes parameters values in some particular situation of polarisation state.

polarisation state	Stokes parameters values			
general polarisation state	I	Q	U	V
Linear polarised light	$(Q^2+U^2)^{1/2}$	$\neq 0$	$\neq 0$	0
Circular polarised light	V	0	0	$\neq 0$
Fully polarised light	$(Q^2+U^2+V^2)^{1/2}$	Q	U	V
Partially polarised light	$> (Q^2+U^2+V^2)$	Q	U	V
Unpolarised light	I	0	0	0

Therefore, Q/I, U/I, and V/I take values in the range [-1,1], and once any of them takes the extreme value, the other parameters become zero. The extremes for Q/I occur when the light is linearly polarised either horizontally or vertically; for U/I when the light is linearly polarised at ±45°; while for V/I when the light is right and left circularly polarised.

Based on the Stokes parameters, the polarisation properties of light can be defined as follows:

The intensity of the polarised component:

$$I_p = \sqrt{Q^2 + U^2 + V^2} \tag{3-10}$$

The intensity of the depolarised component:

$$I_{dp} = \sqrt{I^2 - I_p^2} \tag{3-11}$$

The degree of polarisation:

$$\text{DOP} = \frac{I_p}{\sqrt{I_p^2 + I_{dp}^2}} = \sqrt{(Q^2 + U^2 + V^2)/I^2} \qquad 0 \le DOP \le 1 \qquad \text{(3-}$$

The degree of linear polarisation:

$$\text{DOLP} = \sqrt{(Q^2 + U^2)/I^2} \qquad 0 \le DOLP \le 1 \qquad \text{(3-13)}$$

The degree of circular polarisation:

$$\text{DOCP} = \frac{V}{I} \qquad 0 \le DOCP \le 1 \qquad \text{(3-14)}$$

It must be noted that DOP = 1 corresponds to completely polarised light, DOP = 0 corresponds to completely unpolarised light, and any other value in between corresponds to partially polarised light (Liu, 2005; Schmidt, Schubert, and Schubert, 2013).

The formula for the polarisation orientation (azimuth angle) ψ is:

$$\Psi = \frac{1}{2} tan^{-1} \left(\frac{U}{Q} \right) \qquad \text{(3-15)}$$

The ellipticity:

$$e = \frac{V}{I + \sqrt{Q^2 + U^2}} \qquad \text{(3-16)}$$

Eccentricity:

$$\epsilon = \sqrt{1 - e^2} \qquad \text{(3-17)}$$

The ellipticity angle:

$$\chi = \frac{1}{2} sin^{-1} \left(\frac{V}{I_p} \right) \qquad \text{(3-18)}$$

In principle, the general state of polarisation when polarised light was elliptical, or in other words, when the electric field rotated in an ellipse path. The orientation of

the ellipse major axis measured counter-clockwise from the **x**-axis is known as the azimuth angle, while the ellipticity is the ratio of the minor to the major axis of the ellipse path. The ellipticity differs from 0 for linearly polarised light and can reach up to 1 for circularly polarised light. The eccentricity describes the deviation of the ellipse from circularity, having a value of zero for circularly polarised light, increasing as the ellipse narrows, and reaching a value of one for linearly polarised light (Bass, 1995).

3.4   **Mueller Matrices**

Any optical system consists of several optical components (e.g. a mirror, a lens, or a polarisation element) that interact with light in various ways: reflection, refraction, diffraction, or scattering. When the light is described by the Stokes vector **S**, the interaction between the light and each optical element is determined by using the Mueller matrix **M**, which is a 4x4 matrix with 16 real-valued elements invented by Hans Mueller in 1943. The matrix elements depend on the properties of the optical component.

Besides Jones matrices, the concept of Mueller matrices is considered as an alternative description of the polarisation state and has the ability to handle the depolarisation situation. In general, the Mueller calculus is more suitable for describing polarisation measurements for polarimeters, radiometers, and spectrometers (Bass, 1995; Garcia-Caurel, De Martino, Gaston, and Yan, 2013; Hecht, 2002; Schmidt *et al.*, 2013; Trippe, 2014).

If a light beam with Stokes vector **S$_{in}$** is altered by a material with Mueller matrix M, then the resultant Stokes vector **S$_{out}$** is calculated as:

$$S_{out} = M \, S_{in} \tag{3-19}$$

$$\begin{bmatrix} I` \\ Q` \\ U` \\ V` \end{bmatrix} = \begin{bmatrix} m_{00} & m_{01} & m_{02} & m_{03} \\ m_{10} & m_{11} & m_{12} & m_{13} \\ m_{20} & m_{21} & m_{22} & m_{23} \\ m_{30} & m_{31} & m_{32} & m_{33} \end{bmatrix} \begin{bmatrix} I \\ Q \\ U \\ V \end{bmatrix} \tag{3-20}$$

The following are two examples of Mueller matrices that correspond to a reflection matrix *M$_{ref}$* and rotation matrix *M$_{rot}$* of the coordinate system by an angle β (Trippe, 2014):

$$M_{ref} = \begin{bmatrix} 1 & 0 & 0 & 0 \\ 0 & 1 & 0 & 0 \\ 0 & 0 & -1 & 0 \\ 0 & 0 & 0 & -1 \end{bmatrix}; \quad M_{rot}(\beta) = \begin{bmatrix} 1 & 0 & 0 & 0 \\ 0 & cos2\beta & sin2\beta & 0 \\ 0 & -sin2\beta & cos2\beta & 0 \\ 0 & 0 & 0 & 1 \end{bmatrix} \qquad (3\text{-}21)$$

The formula for determining the Mueller matrix of a rotating optical element by an angle β is:

$$M(\beta) = M_{rot}(-\beta)\, M(0)\, M_{rot}(\beta) \qquad (3\text{-}22)$$

The total Mueller matrix M_{total} that describes a cascade of N components is given by:

$$M_{total} = M_N\, M_{N-1} \ldots\ldots M_2 M_1 = \prod_{n=N,-1}^{n=1} M_n \qquad (3\text{-}23)$$

where the numerals 1, 2, … indicate the first, second, … device that interacts with the light (Bass, 1995).

3.5 The Correlation Between Mueller and Jones Matrices

For a non-depolarising system, the following formula gives the relationship between a Jones and a Mueller matrix (Bass, 2010):

$$M = U(J \otimes J^*)U^{-1} \qquad (3\text{-}24)$$

Where $\otimes$ denotes the tensor product, * denotes the complex conjugate of the matrix, and **U** is the transform matrix:

$$U = \frac{1}{\sqrt{2}} \begin{bmatrix} 1 & 0 & 0 & 1 \\ 1 & 0 & 0 & -1 \\ 0 & 1 & 1 & 0 \\ 0 & i & -i & 0 \end{bmatrix} = (U^{-1})^\dagger \qquad (3\text{-}25)$$

Here, † denotes the Hermitian adjoint.

So, if the Jones matrix is expressed as:

$$J = \begin{bmatrix} j_{xx} & j_{xy} \\ j_{yx} & j_{yy} \end{bmatrix} \qquad (3\text{-}26)$$

Then, the Mueller matrix is given by (Schmidt *et al.*, 2013):

$$M =$$

$$\begin{bmatrix}
\frac{1}{2}\left(|j_{xx}|^2 + |j_{yy}|^2 + |j_{yx}|^2 + |j_{xy}|^2\right) & \frac{1}{2}\left(|j_{xx}|^2 - |j_{yy}|^2 - |j_{yx}|^2 + |j_{xy}|^2\right) & Re\left(j_{xx}j_{yx}^* + j_{yy}^* j_{xy}\right) & Im\left(j_{xx}j_{yx}^* + j_{yy}^* j_{xy}\right) \\
\frac{1}{2}\left(|j_{xx}|^2 - |j_{yy}|^2 + |j_{yx}|^2 - |j_{xy}|^2\right) & \frac{1}{2}\left(|j_{xx}|^2 + |j_{yy}|^2 - |j_{yx}|^2 - |j_{xy}|^2\right) & Re\left(j_{xx}j_{yx}^* - j_{yy}^* j_{xy}\right) & Im\left(j_{xx}j_{yx}^* - j_{yy}^* j_{xy}\right) \\
Re\left(j_{xx}j_{xy}^* + j_{yy}^* j_{yx}\right) & Re\left(j_{xx}j_{xy}^* - j_{yy}^* j_{yx}\right) & Re\left(j_{xx}j_{yy}^* + j_{xy}^* j_{yx}\right) & Im\left(j_{xx}j_{yy}^* - j_{xy}^* j_{yx}\right) \\
-Im\left(j_{xx}j_{xy}^* + j_{yy}^* j_{yx}\right) & -Im\left(j_{xx}j_{xy}^* - j_{yy}^* j_{yx}\right) & -Im\left(j_{xx}j_{yy}^* + j_{xy}^* j_{yx}\right) & Re\left(j_{xx}j_{yy}^* - j_{xy}^* j_{yx}\right)
\end{bmatrix}$$

$$(3\text{-}27)$$

where j* denotes the complex conjugate of j.

On the other hand, the Jones matrix can be represented in terms of the elements of the Mueller matrix, as follows (Bass, 2010):

$$J = \begin{bmatrix}
\frac{1}{\sqrt{2}}\sqrt{m_{00} + m_{01} + m_{10} + m_{11}}\,e^{i\varphi_{xx}} & \frac{1}{\sqrt{2}}\sqrt{m_{00} - m_{01} + m_{10} - m_{11}}\,e^{i\varphi_{xy}} \\
\frac{1}{\sqrt{2}}\sqrt{m_{00} + m_{01} - m_{10} - m_{11}}\,e^{i\varphi_{yx}} & \frac{1}{\sqrt{2}}\sqrt{m_{00} - m_{01} - m_{10} + m_{11}}\,e^{i\varphi_{yy}}
\end{bmatrix} \quad (3\text{-}28)$$

In which the relative phases are:

$$\varphi_{yy} - \varphi_{xx} = arctan\left(\frac{m_{32} - m_{23}}{m_{22} - m_{33}}\right); \qquad\qquad (3\text{-}29)$$

$$\varphi_{yx} - \varphi_{xx} = arctan\left(\frac{m_{30} - m_{31}}{m_{20} - m_{21}}\right); \qquad\qquad (3\text{-}30)$$

$$\varphi_{xx} - \varphi_{xy} = arctan\left(\frac{m_{03} - m_{13}}{m_{22} - m_{23}}\right) \qquad\qquad (3\text{-}31)$$

The phase φ_{xx} represents the reference phase.

3.6   Poincare Sphere

The Poincare sphere is a unity sphere representing polarisation states. It is depicted in Figure 3-2, where *Q, U*, and *V* are the three orthogonal vectors (instead of **x**, **y**, and **z** in the Cartesian coordinate system). *Q/I, U/I*, and *V/I* are the respective polarisation components along with the vectors *Q, U*, and *V, respectively*. The fully polarised states lie on the sphere surface, whereas the partially polarised states lie inside the sphere at a distance I_p from the origin. Any point in the *Q-U* plane represents a linear polarised state. The vector *V* represents the circular polarisation states where the positive values correspond to the right-handed circular polarisation state, and the negative values correspond to the left-handed circular polarisation state. The other

points on the sphere represent elliptically polarisation states Ip. Ψ and χ are the polarisation angle and the ellipticity angle, respectively (Zhang, 2006).
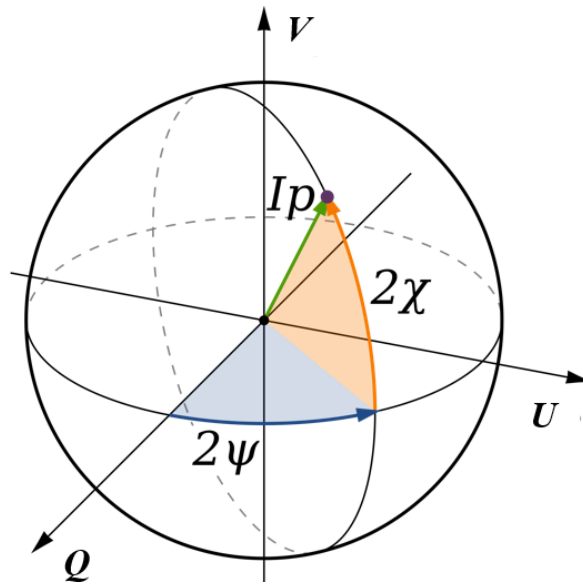
Figure 3-2: The Poincare sphere, where Q, U, and V are the three orthogonal vectors. (Commons. Wikimedia)

4   The Optical Properties of Chiral Metamaterials

Typically, chiral substances tend to display disparity when they absorb the right circular polarisation in comparison to the left. This phenomenon is referred to as circular dichroism. In addition, chiral substances demonstrate optical activity, as they can adapt the orientation of the polarisation of the transmitted linear polarisation light. However, for a non-chiral array (also known as achiral materials), alteration of the polarisation direction is not foreseen (Ma *et al.*, 2017).

In 1845, Faraday discovered the rotational behaviour of the polarisation state of linearly polarised light when a magnetic field was applied. This phenomenon has been known as the Faraday Effect and is attributed to the interaction between the applied magnetic field and the magnetic field of the light wave (Bass, 1995). In 1848, Pasteur recorded opposing but identical levels of polarisation rotation through different crystals of sodium ammonium tartrate. The difference between magnetic rotation and natural optical activity was finally clarified by Lord Kelvin in 1884, when he introduced the notion of chirality to describe this phenomenon (Ye *et al.*, 2017).

4.1   The Polarisation of Light

Polarisation is one of the fundamental results of the interaction between a light beam and matter. Light is electromagnetic waves comprising electric and magnetic field components that oscillate synchronously perpendicular to each other and perpendicular to their propagation direction. In the most common source of light (e.g., sunlight), the waves oscillate in random directions; such light is termed unpolarised light. By contrast, polarised light can be produced by passing the light through a polariser that allows passage only of the light that oscillates in a specific direction, as shown in Figure 4-1. Typically, the light has a combination of polarised and unpolarised waves, termed partially polarised light (Hauge, Mueller, and Smith,1980; Peatross, and Ware, 2011).
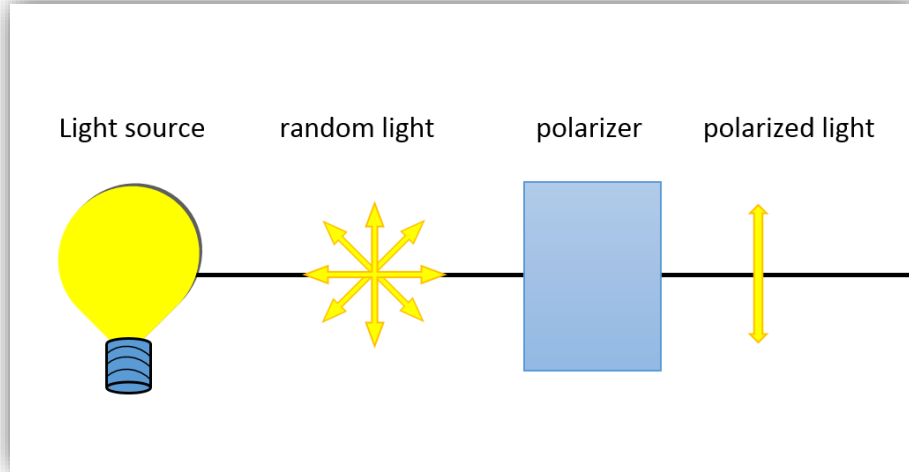
Figure 4-1: The polariser passes only light that oscillated in a specific direction.

The polarisation direction is determined by the direction of the electric field oscillation. For the purpose of simplification, we assume that an electromagnetic wave is travelling as the electric field **E** in the **z**-direction, which is known as a plane wave and could be expressed as the following (Trippe, 2014):

$$\boldsymbol{E}(z,t) = E_0 \, cos(\omega t - kz + \emptyset) \qquad (4\text{-}1)$$

The direction of propagation is specified by the wavenumber k, while Ø is defined as the electric field phase. E(z,t) can be decomposed into its **x** and **y** components, so that

$$E_x(z,t) = E_{x0} \, cos(\omega t - kz + \emptyset_x) \qquad (4\text{-}2)$$

$$E_y(z,t) = E_{y0} \, cos\big(\omega t - kz + \emptyset_y\big) \qquad (4\text{-}3)$$

Here, $\emptyset_x$ and $\emptyset_y$ denote the phase components in the x- and y-axis, respectively. Then the phase retardation between x and y components is $\delta = \emptyset_y$ - $\emptyset_x$. The three independent parameters E_{x0}, E_{y0}, and δ could be used to define the polarisation state of a plane wave (Trippe, 2014).

The polarisation status can be classified as elliptical, circular, or linear. In general, equation 4-1 describes an elliptically polarised wave, where the electric field rotates in the ellipse path. In terms of the direction of travelling, this rotation employs either right or left polarisation. When $\delta > 0$, it means polarisation is right-handed, and the electric field vector rotates clockwise when viewed by an observer looking towards

the light source. Meanwhile, when δ < 0, the wave is described as left-handed polarisation, and the electric field vector rotates anticlockwise, as shown in Figure 4-2 (Trippe, 2014).
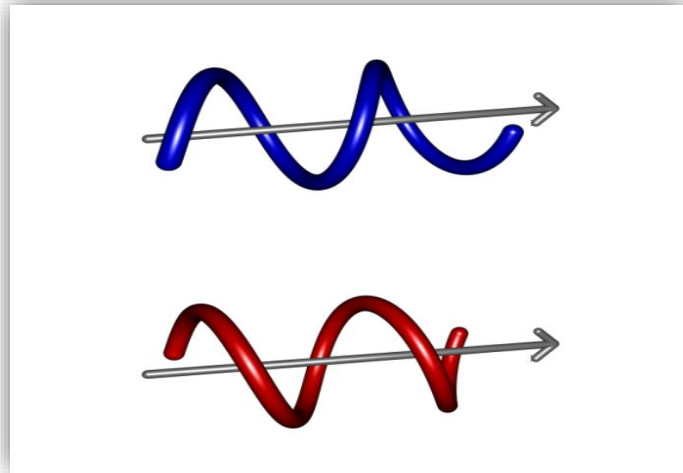
Figure 4-2: Right-handed (blue) and left-handed (red) elliptical polarisation light, with clockwise and anticlockwise rotation of the electric field vector, respectively (Tutor Vista)

Similarly, circular polarisation can be considered as a particular case of elliptical polarisation; however, in the circular polarisation case, the electric field rotates in a circular path with a constant rate, where $E_{x0} = E_{y0} = E_0$. In the case of δ = mπ/2, m=1, 2, 3, …, we have

$$E_x(z,t) = E_0 \cos(\omega t - kz) \tag{4-4}$$

$$E_y(z,t) = \pm E_0 \sin(\omega t - kz) \tag{4-5}$$

The sign ± determines the sense of the motion handedness of E. A positive sign is equivalent to anticlockwise motion and is identified as left-handed circular polarisation. In contrast, a negative sign is equivalent to clockwise motion and is identified as right-handed circular polarisation (Trippe, 2014).

In a linear polarisation case, the light oscillates in a single direction in the **x-y** plane. That can be described as a superposition of the right and left polarised wave with identical amplitude. In this case, $\emptyset_x = \emptyset_y = 2n\pi$, n = 0,1,2,3,… , we can write (Trippe, 2014):

$$E_x(z,t) = E_{x0}\ cos(\omega t - kz) \tag{4-6}$$

$$E_y(z,t) = E_{y0}\ cos(\omega t - kz) \tag{4-7}$$

In the case of $E_{y0} = 0$ (or $E_{x0} = 0$), the electric field of the light oscillates along the **x**-axis (or y-axis), which is known as a horizontally (or vertically) polarised light.

4.2   **Electromagnetic Response of Chiral Materials**

The following relationship gives the chiral material response to electromagnetic wave:

$$\begin{bmatrix} \boldsymbol{D} \\ \boldsymbol{B} \end{bmatrix} = \begin{bmatrix} \varepsilon_0\varepsilon_r & -i\kappa/c \\ i\kappa/c & \mu_0\mu_r \end{bmatrix} \begin{bmatrix} \boldsymbol{E} \\ \boldsymbol{H} \end{bmatrix} \tag{4-8}$$

where **E** is the electric field, **H** is the magnetic field, **D** is the electric displacement, and **H** is the magnetic induction. ε_0 (ε_r) and μ_0 (μ_r) are the permittivity and permeability of vacuum (chiral medium), respectively. c is the speed of light in vacuum, and κ is a parameter that measures the effect of cross-coupling between electric (**E**) and magnetic (**H**) fields (Ma *et al.*, 2017; Li, Mutlu, and Ozbay, 2013; Wang *et al.*, 2009). The refractive index for the right (+) and left (-) circularly polarised light waves can subsequently be defined as:

$$n_\pm = \sqrt{\varepsilon_r\mu_r} \pm \kappa = n_0 \pm \kappa \tag{4-9}$$

The following relationships indicate how these parameters relate to each other (Li *et al.*, 2013):

$$n_0 = (n_+ + n_-)/2, \quad \kappa = (n_+ - n_-)/2, \tag{4-10}$$

4.3 Polarisation Effects of Reflection and Transmission

In general, the Jones matrix provides a mathematical description for a sample that reflects or transmits polarised light by a matrix that contains four complex-valued elements according to the following formula:

$$\begin{bmatrix} E_r^x \\ E_r^y \end{bmatrix} = \begin{bmatrix} r_{xx} & r_{xy} \\ r_{yx} & r_{yy} \end{bmatrix} \begin{bmatrix} E_i^x \\ E_i^y \end{bmatrix} = R \begin{bmatrix} E_i^x \\ E_i^y \end{bmatrix} \tag{4-11}$$

$$\begin{bmatrix} E_t^x \\ E_t^y \end{bmatrix} = \begin{bmatrix} t_{xx} & t_{xy} \\ t_{yx} & t_{yy} \end{bmatrix} \begin{bmatrix} E_i^x \\ E_i^y \end{bmatrix} = T \begin{bmatrix} E_i^x \\ E_i^y \end{bmatrix} \tag{4-12}$$

Here R and T are the reflection and transmission matrices for a linear polariser, respectively. E_i, E_r, and E_t are the incident, reflected and transmitted polarised electric fields, respectively, in **x** or **y** directions. If a metamaterial has mirror symmetry, then $r_{xy} = r_{yx} = t_{xy} = t_{yx} = 0$, which eliminates the off-diagonal elements of R and T to be diagonal matrices (Wang *et al.*, 2016).

The exact mechanism applies for circular polarisation, where

$$R_{circ} = \begin{bmatrix} r_{++} & r_{\pm} \\ r_{\mp} & r_{--} \end{bmatrix}; \qquad T_{circ} = \begin{bmatrix} t_{++} & t_{\pm} \\ t_{\mp} & t_{--} \end{bmatrix} \tag{4-13}$$

The subscript + or − denotes clockwise or counterclockwise circularly polarised waves. For symmetrical structure ($r_{++} = r_{--}$, $r_{+-}=r_{-+}$, $t_{++}= t_{--}$, $t_{+-}= t_{-+}$) (Wang *et al.*, 2016).

In practical terms, the formula below is typically applied to calculate the circular transmission and reflection coefficients from the transmission and reflection coefficients of linearly polarised waves (Li *et al.*, 2013; Wang *et al.*, 2016):

$$\begin{bmatrix} t_{++} & t_{\pm} \\ t_{\mp} & t_{--} \end{bmatrix} = \frac{1}{2} \begin{bmatrix} t_{xx} + t_{yy} + i(t_{xy} - t_{yx}) & t_{xx} - t_{yy} - i(t_{xy} + t_{yx}) \\ t_{xx} - t_{yy} + i(t_{xy} + t_{yx}) & t_{xx} + t_{yy} - i(t_{xy} - t_{yx}) \end{bmatrix} \tag{4-14}$$

$$\begin{bmatrix} r_{++} & r_{\pm} \\ r_{\mp} & r_{--} \end{bmatrix} = \frac{1}{2} \begin{bmatrix} r_{xx} + r_{yy} + i(r_{xy} - r_{yx}) & r_{xx} - r_{yy} - i(r_{xy} + r_{yx}) \\ r_{xx} - r_{yy} + i(r_{xy} + r_{yx}) & r_{xx} + r_{yy} - i(r_{xy} - r_{yx}) \end{bmatrix} \tag{4-15}$$

4.4 Optical Activity

The crystal can rotate the polarisation plane of a linearly polarised light ray and this constitutes optical activity, as illustrated in Figure 4-3. Some materials exhibit natural optical activity, that is, without any external influences (e.g. quartz). However, electric fields can also induce optical activity under particular conditions (Potts *et al.*, 2002; Zhang, 2006).

Fundamentally, due to their low-symmetry structure, chiral materials are naturally optically active. Fresnel attributed optical rotation to a difference in the velocity of propagation of the left and right circularly polarised components of the linearly polarised beam in the medium. It was observed that the enantiomers rotate a given polarisation plane by the same magnitude but in the opposite direction (Arteaga, 2010; Emile *et al.*, 2013).
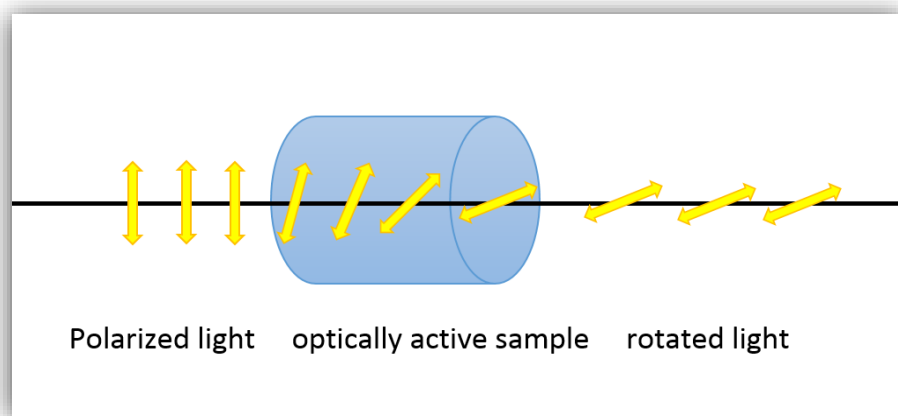
Figure 4-3: Optical activity phenomenon.

4.5 Dichroism

Chiral materials exhibit disparity in that the right circularly polarised light is absorbed to a greater or lesser extent than the left circularly polarised light. Such an optical phenomenon is known as Circular Dichroism. Similarly, linear dichroism occurs as a result of differential absorption between two orthogonal components of linearly polarised light with certain non-isotropic crystals (Arteaga, 2010; Kwon, Werner, and Werner, 2008).

4.6 Birefringence

When light passes through a substance, it changes the velocity depending on the refractive index of that substance. However, some materials have two refractive indices known as birefringent materials, as depicted in Figure 4-4. The phenomenon of birefringence arises due to anisotropy within some crystals or fluids, causing the optical properties to differ according to direction. However, some materials exhibit birefringence at specific wavelengths of light. Birefringent materials are employed in several optical elements that are used to modify the polarisation state of light, such as polarisers and waveplates.

The two orthogonal components of linearly polarised beam travel through the birefringent materials at different velocities so that they exit with a phase difference known as the retardance. As a result of passing through a birefringent crystal, the linear polarisation light can be either circular or elliptical (Lin and Lee, 2012; McCall, Hodgkinson, and Wu, 2014; Plum, 2010).

Figure 4-4: A birefringent crystal. (Wiersma, 2013)

5   Experimental Methods

This chapter emphasises the dual photoelastic modulator setup with the lock-in amplifier technique used in this project to measure the polarisation states, which is fully illustrated later through this chapter. Subsequently, these polarisation states are then analysed mathematically based on their Stokes parameters and Mueller matrices.

5.1   Polarimeter

A polarimeter is an optical instrument with polarisation elements used to measure the polarisation properties of light beams, including the direction of the wave oscillation and the degree of polarisation in a given case, as a means of studying the optical characteristics of a sample. The polarimeters are used in several different fields, including astronomy, spectroscopy, and ellipsometry (when used for surfaces). Indeed, such instruments can facilitate the examination of a wide range of sample types, such as thin films, optical elements, geological surfaces, and biological structures.

To characterise the polarisation state of the light beam, a set of measurements is acquired by a series of optical elements based on multiple procedures, including measurements, calibrations, data reductions, and the comparison between the polarisation states of the incident and the exiting beams. The optical elements located between the light source and the sample are known collectively as the polarisation state generator (PSG). In contrast, those located between the sample and the detector are known as polarisation state analyser (PSA). To use Stokes representation, the PSG generates a polarised light with a Stokes vector that enters the sample, allowing the PSA to analyse the changes in the Stokes vector of that light after interfering with the sample (Bass, 1995).

The polarimeter can be one of two types: either a single wavelength polarimeter or a spectroscopic polarimeter. In the single wavelength polarimeter, a monochromatic light source is used to create a single set of resultant parameters. In contrast, with the spectroscopic polarimeter, a multi-wavelength light source is used to generate sample parameters as a function of wavelength (Shamiryan and Likhachev, 2012). However, in the current work, two types of LED with different wavelength were used as a monochromatic light source (see the details in chapter 7).

5.2 Polarimeter Elements

This section provides an overview of the elements used in the polarimetry that used in this project.

5.2.1 The Polariser

In 1928, Edwin H. Land discovered the polariser by immersing a stretched polymer sheet into iodine. Due to the stretching, the polymer chains aligned along a common direction known as the transmission axis. Therefore, the function of the polariser is to convey only the electric field components that oscillate parallel to its transmission axis (Bass, 1995).

Any polariser oriented at an angle θ can be represented by 2x2 as Jones matrix or 4x4 as Mueller matrix (Aas, 2009):

$$J_{polariser} = \begin{bmatrix} cos^2\theta & sin\theta cos\theta \\ sin\theta cos\theta & sin^2\theta \end{bmatrix}, \tag{5-1}$$

$$M_{polariser} = \frac{1}{2} \begin{bmatrix} 1 & cos(2\theta) & sin(2\theta) & 0 \\ cos(2\theta) & cos^2(2\theta) & cos(2\theta) sin(2\theta) & 0 \\ sin(2\theta) & cos(2\theta) sin(2\theta) & sin^2(2\theta) & 0 \\ 0 & 0 & 0 & 0 \end{bmatrix} \tag{5-2}$$

Typically, two polarisers are used in the polarimetry, one within the PSG to generate a linear polarised light before the sample and the other within the PSA after the sample.

5.2.2 The Wave Plate

A wave plate (WP) is an optical element made of a birefringent material with a birefringence Δn. The WP causes retardation of one component of the electric field (E_x or E_y) compared to the other, which results in a retardance ($\Delta\Phi$), where $\Delta\Phi=\pi$ for the half-wave plate (HWP) and $\Delta\Phi=\pi/2$ for the quarter-wave plate (QWP). The Mueller matrix of the WP is given by (Aas, 2009):

$$M_{WP} = \frac{1}{2} \begin{bmatrix} 1 & 0 & 0 & 0 \\ 0 & 1 & 0 & 0 \\ 0 & 0 & cos(\Delta\Phi) & -sin(\Delta\Phi) \\ 0 & 0 & sin(\Delta\Phi) & cos(\Delta\Phi) \end{bmatrix} \tag{5-3}$$

5.2.3 The Photoelastic Modulator

The phenomenon whereby some materials become birefringent under stress is known as the photoelastic effect. Based on this effect, J. Badoz developed the photoelastic modulator (PEM) in the 1960s. PEM is an optical component designed primarily to modify or analyse the polarisation state of the light. It commonly consists of fused silica and a piezoelectric transducer (which gives electricity under pressure) (Guan *et al.*,2010).

If, for example, a beam passes through a PEM, the electric component parallel to the PEM axis will travel faster than the perpendicular one. A new polarisation state is generated owing to the retardation phase between the two electric components. In this context, the PEM is a valuable element of any optical system where the assessment of a specific polarisation state is required.

The PEM can be described using the Mueller matrix as follows (Guan *et al.*, 2008):

$$\boldsymbol{M_{PEM}} =$$

$$\begin{pmatrix} 1 & 0 & 0 & 0 \\ 0 & cos(4\alpha)\,sin^2\left(\frac{\delta}{2}\right) + cos^2\left(\frac{\delta}{2}\right) & sin(4\alpha)sin^2\left(\frac{\delta}{2}\right) & -sin(2\alpha)\,sin\,(\delta) \\ 0 & sin(4\alpha)sin^2\left(\frac{\delta}{2}\right) & -cos(4\alpha)\,sin^2\left(\frac{\delta}{2}\right) + cos^2\left(\frac{\delta}{2}\right) & cos(2\alpha)\,sin\,(\delta) \\ 0 & sin(2\alpha)\,sin\,(\delta) & -cos(2\alpha)\,sin\,(\delta) & cos\,(\delta) \end{pmatrix}$$

$$(5\text{-}4)$$

Here, α is the angle between the fast axis of the PEM and the **x**-axis. $\delta = \delta_0 \sin\,(\Omega t)$ is the retardation phase produced by the PEM, where δ_0 is the retardation amplitude, and Ω is the modulating frequency of the PEM (Guan *et al.*, 2008; Liu, 2005).

The outcome signal can be represented by Bessel functions of the first kind and usually detected by the lock-in amplifier, where:

$$\sin(\delta) = \sin(\delta_0\,\sin\,(\Omega t)) = 2J_1(\delta_0)\,sin(\Omega t) + \cdots \qquad (5\text{-}5)$$

$$\cos(\delta) = \cos(\delta_0\,\sin\,(\Omega t)) = J_0(\delta_0)\,sin(\Omega t) + 2J_2(\delta_0)\,sin(2\Omega t) + \cdots \qquad (5\text{-}6)$$

In a polarimetric system, PEM modulates the relative phase retardation of the incident light sinusoidally and rapidly; it acts as an oscillating phase linear retarder.

5.2.4 The Lock-in Amplifier Technique

Measurement system sensitivity can be improved via the lock-in amplifier technique, whereby the photodiode converts light to a small current, and the current is in turn converted by the amplifier to voltage signals.

In this experiment, the DC signal is measured by an electrometer, and each of the other harmonic signals is measured by a different lock-in amplifier. All these signals are measured simultaneously by using a Keithley 6517 electrometer and three separate lock-in amplifiers, namely, Perkin-Elmer 7265, Stanford Research System SR810DSP, and EG&G 5209 (Liu, Jones, Peng, and Shen, 2006; Guan *et al.*, 2008; Guan *et al.*, 2010).

5.3 Determination of Stokes Parameters Using Dual PEM

The experimental setup is shown in Figure (5-1); the polarimetry comprises a light source, a polariser, two photoelastic modulators, an analyser, and a photodetector.

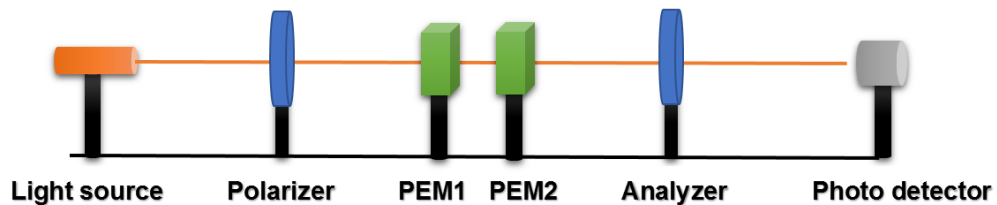*Figure 5-1: The setup of dual PEMs polarimetry.*

The modulators must operate at different frequencies to be able to distinguish their harmonics. Let us assume that the passing axis of PEM2 indicates the **x**-axis and the passing axis of PEM1 and the analyser (A) make an angle α and an angle β with the **x**-axis, respectively, as shown in Figure (5-2) (Guan *et al.*, 2008; Guan *et al.*, 2010).
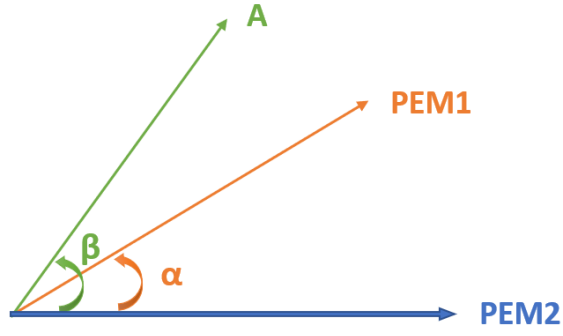
Figure 5-2: the orientation of the experimental components.

In this situation, the Mueller matrices for each of the PEM1, PEM2, and analyser are as follows:

$$M_{PEM1}$$
$$= \begin{bmatrix} 1 & 0 & 0 & 0 \\ 0 & cos(4\alpha) \, sin^2\left(\frac{\delta_1}{2}\right) + cos^2\left(\frac{\delta_1}{2}\right) & sin(4\alpha) sin^2\left(\frac{\delta_1}{2}\right) & -sin(2\alpha) \, sin(\delta_1) \\ 0 & sin(4\alpha) sin^2\left(\frac{\delta_1}{2}\right) & -cos(4\alpha) \, sin^2\left(\frac{\delta_1}{2}\right) + cos^2\left(\frac{\delta_1}{2}\right) & cos(2\alpha) \, sin(\delta_1) \\ 0 & sin(2\alpha) \, sin(\delta_1) & -cos(2\alpha) \, sin(\delta_1) & cos(\delta_1) \end{bmatrix}$$

(5-7)

$$M_{PEM2} = \begin{bmatrix} 1 & 0 & 0 & 0 \\ 0 & 1 & 0 & 0 \\ 0 & 0 & cos(\delta_2) & sin(\delta_2) \\ 0 & 0 & -sin(\delta_2) & cos(\delta_2) \end{bmatrix}$$

(5-8)

$$M_{analyser} = \frac{1}{2} \begin{bmatrix} 1 & cos(2\beta) & sin(2\beta) & 0 \\ cos(2\beta) & cos^2(2\beta) & cos(2\beta) \, sin(2\beta) & 0 \\ sin(2\beta) & cos(2\beta) \, sin(2\beta) & sin^2(2\beta) & 0 \\ 0 & 0 & 0 & 0 \end{bmatrix}$$

(5-9)

$\delta_i = \delta_{i0} \, sin(\Omega_i t)$, i=1,2, is the retardation phase produced by the PEMi, δ_{i0} is the retardation amplitude, and Ω_i is the modulating frequency of the PEMi (Guan *et al.*, 2008; Guan *et al.*, 2010).

Then

$$S_{out} = M_A(\beta)M_{PEM2}(0)M_{PEM1}(\alpha)S_{in} \tag{5-10}$$

where $S_{in} = [I\ Q\ U\ V]^T$ represents Stokes parameters of the polarised light emitted through the polariser, while $S_{out} = [\Gamma`\ Q`\ U`\ V`]^T$ represents the Stokes parameters for the beam after entering through PEM1, PEM2, and then the analyser, respectively, where $[\ldots]^T$ indicates the matrix transposed. After multiplying the three matrices, the quantity identified by the detector, $\Gamma`$, can be determined as follows (see Appendix B):

$$\Gamma` = I_{DC} + I_{QU1} + I_{QU2} + I_V \tag{5-11}$$

where:

$$I_{DC} = g_1 I + g_2 Q + g_3 U \tag{5-12}$$

$$I_{QU1} = g_4 Q + g_5 U \tag{5-13}$$

$$I_{QU2} = g_6 Q + g_7 U \tag{5-14}$$

$$I_V = g_8 V \tag{5-15}$$

The four sub-equations could be rewritten in matrix form as (Guan *et al.*, 2010):

$$\begin{pmatrix} I_{DC} \\ I_{QU1} \\ I_{QU2} \\ I_V \end{pmatrix} = \begin{pmatrix} g_1 & g_2 & g_3 & 0 \\ 0 & g_4 & g_5 & 0 \\ 0 & g_6 & g_7 & 0 \\ 0 & 0 & 0 & g_8 \end{pmatrix} \begin{pmatrix} I \\ Q \\ U \\ V \end{pmatrix} \tag{5-16}$$

Where I_{DC}, I_{QU1}, I_{QU2}, and I_V are four different signals that can be measured experimentally by using different lock-in amplifiers, while g_i (i=1, 2, ...8) are constants dependent on the retardation of the two photoelastic modulators, and also the angles between PEM2 and both PEM1 and the analyser (α and β) (Guan *et al.*, 2010). Then, the last equation could be rewritten as:

$$I_{out} = G\ S_{in}$$

The Stokes parameters of the entering polarised light can be obtained by calculating the matrix inversion, as follows:

$$G^{-1} = \frac{1}{|G|}\widetilde{G}$$

$$|G| = g_1\big(g_4(g_7g_8) - g_5(g_6\,g_8)\big) = g_1g_8(g_4g_7 - g_5g_6) = g_{det}$$

$$\widetilde{G}_{ij} = (-1)^{i+j}\big|M_{ji}\big|$$

Mji is a submatrix obtained by removing j-th row and i-th column from G

$$\begin{pmatrix} g_1 & g_2 & g_3 & 0 \\ 0 & g_4 & g_5 & 0 \\ 0 & g_6 & g_7 & 0 \\ 0 & 0 & 0 & g_8 \end{pmatrix}$$

$$\widetilde{G} = \begin{pmatrix} \begin{vmatrix} g_4 & g_5 & 0 \\ g_6 & g_7 & 0 \\ 0 & 0 & g_8 \end{vmatrix} & -\begin{vmatrix} g_2 & g_3 & 0 \\ g_6 & g_7 & 0 \\ 0 & 0 & g_8 \end{vmatrix} & \begin{vmatrix} g_2 & g_3 & 0 \\ g_4 & g_5 & 0 \\ 0 & 0 & g_8 \end{vmatrix} & -\begin{vmatrix} g_2 & g_3 & 0 \\ g_4 & g_5 & 0 \\ g_6 & g_7 & 0 \end{vmatrix} \\ -\begin{vmatrix} 0 & g_5 & 0 \\ 0 & g_7 & 0 \\ 0 & 0 & g_8 \end{vmatrix} & \begin{vmatrix} g_1 & g_3 & 0 \\ 0 & g_7 & 0 \\ 0 & 0 & g_8 \end{vmatrix} & -\begin{vmatrix} g_1 & g_3 & 0 \\ 0 & g_5 & 0 \\ 0 & 0 & g_8 \end{vmatrix} & \begin{vmatrix} g_1 & g_3 & 0 \\ 0 & g_5 & 0 \\ 0 & g_7 & 0 \end{vmatrix} \\ \begin{vmatrix} 0 & g_4 & 0 \\ 0 & g_6 & 0 \\ 0 & 0 & g_8 \end{vmatrix} & -\begin{vmatrix} g_1 & g_2 & 0 \\ 0 & g_6 & 0 \\ 0 & 0 & g_8 \end{vmatrix} & \begin{vmatrix} g_1 & g_2 & 0 \\ 0 & g_4 & 0 \\ 0 & 0 & g_8 \end{vmatrix} & -\begin{vmatrix} g_1 & g_2 & 0 \\ 0 & g_4 & 0 \\ 0 & g_6 & 0 \end{vmatrix} \\ -\begin{vmatrix} 0 & g_4 & g_5 \\ 0 & g_6 & 7 \\ 0 & 0 & 0 \end{vmatrix} & \begin{vmatrix} g_1 & g_2 & g_3 \\ 0 & g_6 & g_7 \\ 0 & 0 & 0 \end{vmatrix} & -\begin{vmatrix} g_1 & g_2 & g_3 \\ 0 & g_4 & g_5 \\ 0 & 0 & 0 \end{vmatrix} & \begin{vmatrix} g_1 & g_2 & g_3 \\ 0 & g_4 & g_5 \\ 0 & g_6 & g_7 \end{vmatrix} \end{pmatrix}$$

$$\widetilde{G}$$

$$= \begin{pmatrix} g_4g_7g_8 - g_5g_6g_8 & g_8(g_3g_6 - g_2g_7) & g_8(g_2g_5 - g_3g_4) & 0 \\ 0 & g_8g_1g_7 & -g_8g_1g_5 & 0 \\ 0 & -g_8g_1g_6 & g_8g_1g_4 & 0 \\ 0 & 0 & 0 & g_1(g_4g_7 - g_5g_6) \end{pmatrix}$$

$$K = G^{-1} = \begin{pmatrix} k_1 & k_2 & k_3 & 0 \\ 0 & k_4 & k_5 & 0 \\ 0 & k_6 & k_7 & 0 \\ 0 & 0 & 0 & k_8 \end{pmatrix}$$

33

$$\begin{pmatrix} I \\ Q \\ U \\ V \end{pmatrix} = \begin{pmatrix} k_1 & k_2 & k_3 & 0 \\ 0 & k_4 & k_5 & 0 \\ 0 & k_6 & k_7 & 0 \\ 0 & 0 & 0 & k_8 \end{pmatrix} \begin{pmatrix} I_{DC} \\ I_{QU1} \\ I_{QU2} \\ I_V \end{pmatrix} \tag{5-17}$$

where k_i (i=1, 2, …..8) are eight constants related to g_i, which could be determined experimentally through the calibration process, as illustrated in section 5.5. The **G** and **K** matrix should be an invertible matrix; thus, the determinant of both of them must not be zero.

A simplified version of this equation is:

$$\boldsymbol{S_{in} = K\, I_{out}} \tag{5-18}$$

By using the previous methodology, the sample properties can be studied without moving any elements of the PSA components.

5.4   Experimental Errors

Systematic errors can arise from various sources during the experimental processes are carried out in this work; these include misalignment of the optical elements and determination of the retardation amplitude of PEMs (Liu, 2005). In addition, several random errors may be generated by fluctuation in light intensity due to variations in the lab temperature or fluctuation in the amplitude of the PEM retardation (Liu, 2005).

To diminish the potential variation in light intensity, the fluctuations in room temperature were minimised to ±1ºC during the measurement process by using air conditioner. Also, to reduce the systematic errors, the PSA part of the dual PEM polarimetry was calibrated to determine the eight constants in equation (5-17) before any samples were added. Possible errors in the determination of the retardation values and the angle of the analyser and the PEM1 are thus involved within these eight constants. Moreover, the dual PEM polarimetry allowed to perform the measurement without further moving of any component in the PSA part of the system after calibration, preventing additional misalignment issues (Liu, 2005; Guan *et al.*, 2010).

5.5 Calibration Steps for the Dual PEM Polarimetry

In order to avoid any possible errors in the experimental arrangement, the optical system was calibrated to determine the K matrix prior to adding any sample. To calibrate the dual PEM polarimetry, the following steps were taken (Liu, 2005; Guan *et al.*, 2010):

1. The polariser axis was set at 0º and placed in the light path.

2. The analyser was placed in the light path and rotated to the extinction position.

3. One of the photoelastic modulators, PEM2, was placed between the polariser and the analyser, then slowly rotated to the extinction position, meaning that the fast axis was placed parallel to the fast axis of the analyser, which denotes the **x**-axis of the experiments.

4. The other photoelastic modulator, PEM1, was placed between PEM2 and the polariser and rotated so that the angle between its fast axis and the **x**-axis was α=45°.

5. The retardation of both PEM1 and PEM2 was set at the first root of the Bessel function of the first kind; 2.4048 (see Appendix B).

6. The analyser was rotated until the angle between its passing axis and the **x**-axis was β=22.5°.

7. Linearly polarised light was then generated by passing the light through a rotatable linear polariser. The resulting polarised beam was then focused on the PSA system, which consists of the dual PEM and the analyser.

8. All the four experimental signals, namely, $I_{DC}, I_{QU1}, I_{QU2,}$ and I_V were measured using an electrometer and three different lock-in amplifiers.

9. The passing axis of the polariser was set at a series of angles $\psi = 0°, 5°, 10°, 15°, 20°, ..., 180°$ to generate a range of values of linear polarised light, and the four resulting signals corresponding to each value were measured.

10. A circularly polarised light was generated by inserting a quarter-wave plate into the PSG part after the polariser, and the values were changed by setting the polariser at a series of angles in 10° increments (0°, 10°, 20°, …).

11. All ki (i=1, 2, 3, …)=1 were considered as initial values to be able to calculate I, Q, U, and V from equation (5-17).

12. The validity of the work was verified by using equation (3-15) to calculate the azimuth angles of the linear polarised light ψ. Subsequently, the first error was calculated by determining the difference between the initial consideration of ψ and the value calculated by applying the equation.

13. By assuming 100% polarised light, the relationship between I, Q, U, and V is:

$$I^2 = Q^2 + U^2 + V^2 \qquad (5\text{-}19)$$

The second error can be calculated by finding the difference between the theoretical and experimental I^2.

14. The ki constants were obtained simultaneously by using Excel solver by minimising the total errors.

The calibration results are discussed in more detail in Chapter 7.

5.6   The Polarimetric Light Microscope

Insight into the material structure can be gained by using a light microscope. This instrument can be converted to a polarised light microscope by inserting a polariser before the sample stage to generate a polarised light and an analyser after the sample stage to analyse the changes in the polarised light after interacting with the sample. The polarised microscope has the ability to provide information about the optical properties of materials. The microscopic imaging can be characterised completely using the Stokes polarimetry technique, which provides an interesting tool to study biological tissue, crystal structure, and metamaterial surfaces.

This project uses a light microscope converted in the laboratory to a polarised microscope by adding a dual PEM configuration illustrated previously in section 5.3. Figure 5-3 shows a photograph of the Stokes polarimeter microscope in transmission geometry. The system consists of a polarisation state generator (PSG), sample stage, objective lens, and polarisation state analyser (PSA). The PSG integrates a rotatable linear polariser, and a quarter-wave plate can be inserted to generate different states of linear and circular polarised light. In contrast, the PSA consists of dual PEMs and an analyser for analysing polarisation changes.
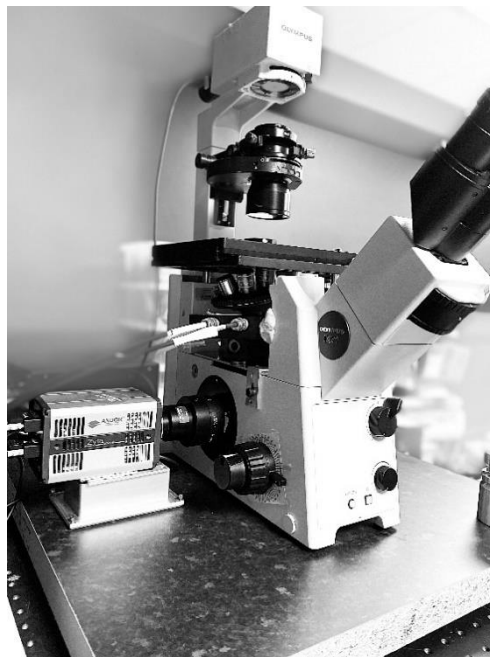

Figure 5-3: A photograph of the polarised microscope

During studying the mesoscopic structure, polarisation information regarding the two-dimensional structures is obtained at each individual pixel by using a digital camera to acquire microscopic images. The LabView 'virtual instrument' alongside Python is used to allow a fully quantitative measurement of Stokes parameters from the output signals.

Before doing samples measurements, a calibration technique is applied in the absence of the sample to estimate the ki constants. During the calibration procedure, rotation of the polariser or the quarter-wave plate allows the generation of different linear and circular polarisation states. The output signals are collected in each pixel of the resultant image. The eight constants ki are obtained following the same steps illustrated in the previous section 5.5.

In order to study a sample, the sample is placed on the sample stage, and the four Stokes parameters are obtained using equation 5-17. Determining the Stokes parameters of the sample can reveal additional information regarding the polarisation characteristics of the light, such as Ip, Idp, DOP, DOLP, DOCP, ψ, and χ, which are defined in section 3.3. By using the microscope, these polarisation characteristics can be determined in each pixel of the two-dimensional structure.

6   Simulation Work

Simulation is an integral component of theoretical and experimental studies in the field of applied science. There are many ways in which scientific studies are improved by employing simulation methodology, including the following:

- Visualisation: simulations provide supportive means to gain extensive visualisation of scientific cases.

- Replication of reality: when analytical or experimental solutions are problematic, simulations can help to mimic reality.

- Numerical calculation: a simulation is a powerful tool for solving complicated mathematical problems quickly and easily.

Even with regard to the amount of time needed to learn programming languages, simulation has effective applications in many scientific sectors, including mathematics, physics, biology, engineering, and chemistry. By using simulation, numerous models can be generated simply by changing the initial parameters or conditions (Cormen, Leiserson, Rivest, and Stein, 2009; Nava, and Kreinovich, 2016).

The usefulness of simulation is especially well illustrated by the field of nanotechnology, where the small size of the materials contributes to the complexity of measurements. A virtual nano-sample can be constructed with modelling, and its behaviour can be predicted under different circumstances without conducting an actual experiment. It is clear that simulation can be successfully used to reduce the time and the cost of scientific studies. In general, enhanced computing capability provides an open opportunity to support future developments in the era of nano-devices (MacLennan, 2008).

MATLAB programming facilitates the opportunity to model a realistic case by using high-level language prior to conducting an experimental study. This chapter attempts to understand Osipov and Potts models behaviour (which will be explained later in section 6.2) and calculate the chirality for a single triangle using MATLAB.

Subsequently, these MATLAB codes were used to study the chirality of gammadion patterns and how it depends on the triangle model.

6.1 Triangle Model

The simplest 2D object is defined by three points (triangle), which create an achiral object in two situations: an isosceles triangle or an equilateral triangle (regular triangle). Otherwise, the triangle (scalene triangle) is classified as a chiral object with three different sides, which could be labelled as Large (L), Medium (M), and Small (S). In accordance with this view, the triangle can be classified as either C_{LMS} or A_{LMS} based on the clockwise or anticlockwise ordering of Large, Medium, and Small sides(LMS), as depicted in Figure 6-1 (Fowler, 2005).
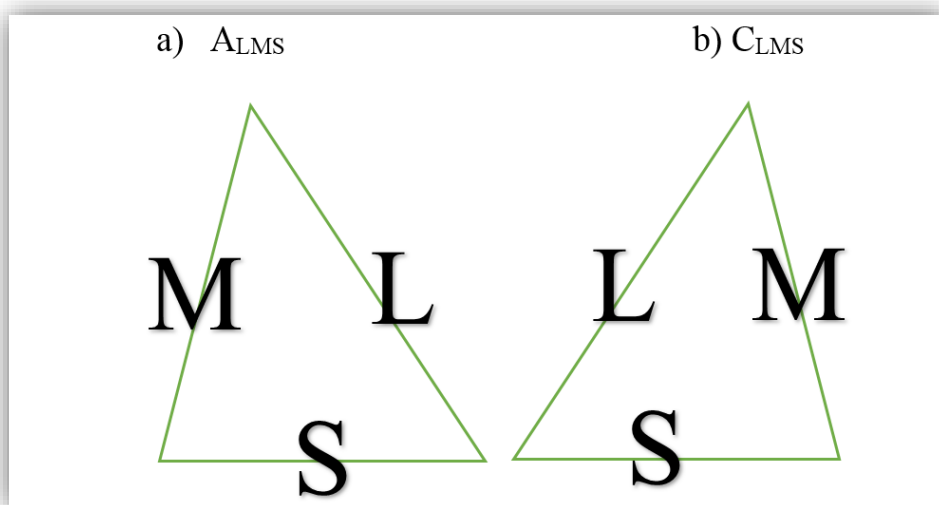

Figure 6-1: The handedness of two enantiomer triangles. a) A_{LMS} triangle where the ordering of the Large, Medium, and Small sides is anticlockwise. b) C_{LMS} triangle where the ordering of the Large, Medium, and Small sides is clockwise.

The triangle model effectively describes the chirality index (K) measurement in planar materials. Several attempts have been made to determine the chirality based on the asymmetry area of the triangle when placed over its mirror image, as further examples in Table 6-1.

As shown in the table below, there are many functions which can, to a certain degree, express the chirality as defined in section 2.4.

Table 6-1: Examples of the functions that calculate the chirality based on triangle model, where a_i, a_j, and a_k are the triangle sides, while θ_i, θ_j and θ_k are the triangle angles.

Chirality index (K) expression of a triangle	Reference
$$\frac{\Delta}{(a_i a_j a_k)^2}\left[\left(\frac{a_i^2}{a_k^2}-\frac{a_i^2}{a_j^2}\right)cos(\theta_i)+\left(\frac{a_j^2}{a_i^2}-\frac{a_j^2}{a_k^2}\right)cos(\theta_j)\right.$$ $$\left.+\left(\frac{a_k^2}{a_j^2}-\frac{a_k^2}{a_i^2}\right)cos(\theta_k)\right]$$	Potts et al. (2003)
$$\Delta\left[\frac{a_j^2-a_k^2}{a_i^2+\left|a_j^2-a_k^2\right|}+\frac{a_k^2-a_i^2}{a_j^2+\left|a_k^2-a_i^2\right|}+\frac{a_i^2-a_j^2}{a_k^2+\left|a_i^2-a_j^2\right|}\right]$$	Potts et al. (2003)
$$\Delta\left[\left(\frac{a_k}{a_j}-\frac{a_j}{a_k}\right)cos(\theta_i)+\left(\frac{a_i}{a_k}-\frac{a_k}{a_i}\right)cos(\theta_j)+\left(\frac{a_j}{a_i}-\frac{a_i}{a_j}\right)cos(\theta_k)\right]$$ $$\Delta\left[\left(\frac{a_j^2}{a_i^2}-\frac{a_i^2}{a_j^2}\right)+\left(\frac{a_k^2}{a_j^2}-\frac{a_j^2}{a_k^2}\right)+\left(\frac{a_i^2}{a_k^2}-\frac{a_k^2}{a_i^2}\right)\right]$$	Potts et al. (2003)
$$\Delta\left[\left(\frac{a_i-a_j}{a_i+a_j}\right)+\left(\frac{a_j-a_k}{a_j+a_k}\right)+\left(\frac{a_k-a_i}{a_k+a_i}\right)\right]$$	Potts et al. (2003)
$$cos\left(2(2\theta_i-\theta_j)\right)+cos\left(2(2\theta_j-\theta_k)\right)+cos(2(2\theta_k-\theta_i))$$ $$-cos\left(2(2\theta_j-\theta_i)\right)-cos\left(2(2\theta_k-\theta_j)\right)-cos(2(2\theta_i-\theta_k))$$	Rassat and Fowler (2003)
$$\frac{1}{\pi^6}\theta_i\theta_j\theta_k\left(\theta_i-\theta_j\right)\left(\theta_j-\theta_k\right)(\theta_k-\theta_i)$$	Rassat and Fowler (2003)
$$\left(sin\theta_i-sin\theta_j\right)\left(sin\theta_j-sin\theta_k\right)(sin\theta_k-sin\theta_i)$$	Rassat and Fowler (2003)

6.2 Osipov and Potts Models

For the purposes of this study, the focus is on the outcomes of the four models presented by Potts *et al.* (2003). These models are simple to apply to different 2D shapes and almost satisfy the requirements of the chirality measurement. These models take the following forms:

Osipov's model:

$$K(\text{Osipov}) = \frac{\Delta}{(a_i a_j a_k)^2} \left[\left(\frac{a_i^2}{a_k^2} - \frac{a_i^2}{a_j^2} \right) cos(\theta_i) + \left(\frac{a_j^2}{a_i^2} - \frac{a_j^2}{a_k^2} \right) cos(\theta_j) + \left(\frac{a_k^2}{a_j^2} - \frac{a_k^2}{a_i^2} \right) cos(\theta_k) \right]$$

(6-1)

Potts' 1ˢᵗ model:

$$K(\text{1st}) = \Delta \left[\frac{a_j^2 - a_k^2}{a_i^2 + |a_j^2 - a_k^2|} + \frac{a_k^2 - a_i^2}{a_j^2 + |a_k^2 - a_i^2|} + \frac{a_i^2 - a_j^2}{a_k^2 + |a_i^2 - a_j^2|} \right]$$

(6-2)

Potts' 2ⁿᵈ model:

$$K(\text{2nd}) = \Delta \left[\left(\frac{a_j^2}{a_i^2} - \frac{a_i^2}{a_j^2} \right) + \left(\frac{a_k^2}{a_j^2} - \frac{a_j^2}{a_k^2} \right) + \left(\frac{a_i^2}{a_k^2} - \frac{a_k^2}{a_i^2} \right) \right]$$

(6-3)

Potts' 3ʳᵈ model:

$$K(\text{3rd}) = \Delta \left[\left(\frac{a_i - a_j}{a_i + a_j} \right) + \left(\frac{a_j - a_k}{a_j + a_k} \right) + \left(\frac{a_k - a_i}{a_k + a_i} \right) \right]$$

(6-4)

Where: a_i, a_j and a_k represent the lengths of the triangle's sides opposite to angles θ_i, θ_j and θ_k, respectively, and Δ denotes the area of the triangle, as shown in Figure 6-2.
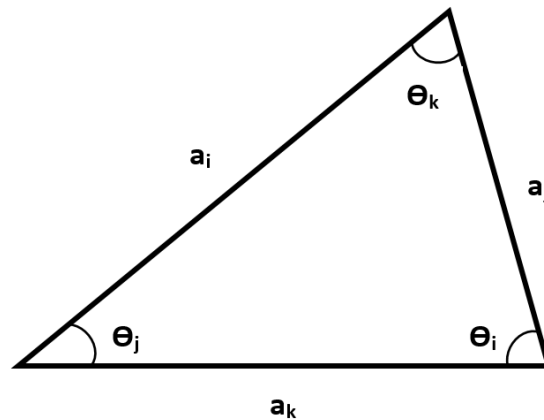
Figure 6-2: A triangle with the labelling of sides (a_i, a_j, and a_k), and angles(θ_i, θ_j, and θ_k).

6.2.1 Sensitivity to the Sense of Handedness

In order to gain an in-depth understanding of the sensitivity of the above-mentioned models to the sense of handedness, the chirality index K is obtained of different triangles as a function of one angle (θ_3) when $0°< \theta_3 <180°$ and the K of mirror images of these triangles, i.e. when $180°< \theta_3 <360°$. These triangles have sides a_1, a_2, and a_3 where $a_1=1$, $a_2= r\ a_1$, and a_3 changes as the opposite angle θ_3 changes from $0°$ to $360°$. As defined by the four previous formulas, the chirality index K is plotted as a function of θ_3. The outcomes for $r=0.5$ and $r=0.7$ are shown in Figures 6-3 and 6-4, as similar to the work done by Potts *et al.* (2003). As expected, the sign of chirality K changes when the handedness of the triangle changes, meaning that when $\theta_3 >180°$, K has the same value but with a different sign than K when $\theta_3 < 180°$. These results indicate that all the four models sensitive to the change of the handedness of the structure where they changed the sign when the handedness reversed.
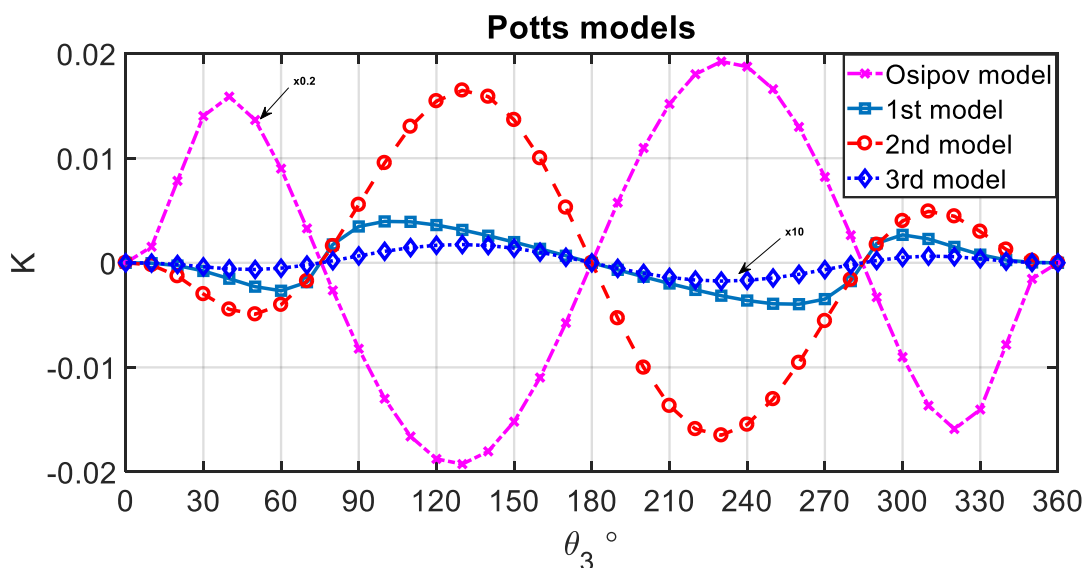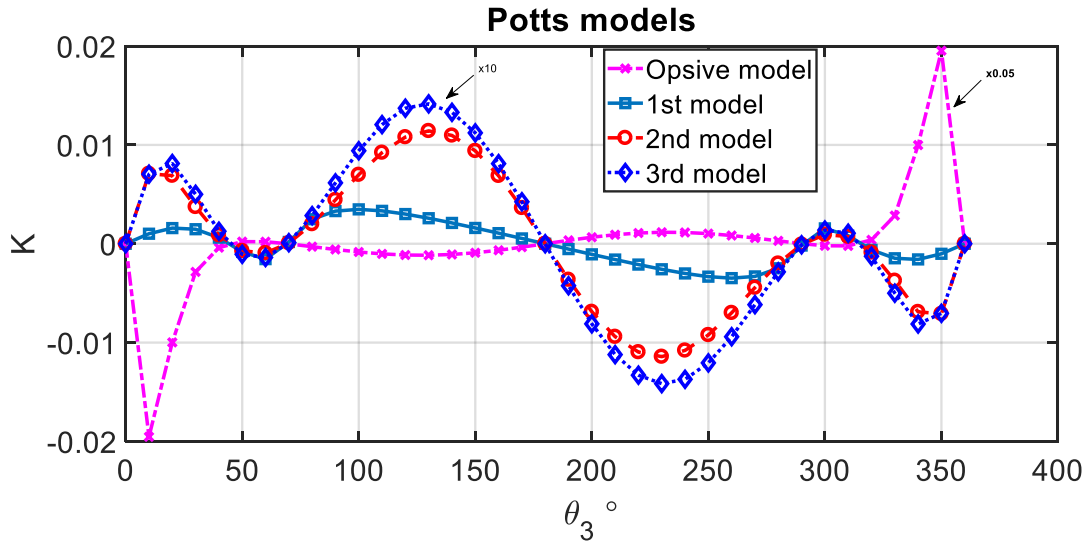

Figure 6-3: The chirality of triangles with sides $a_1=1$, $a_2=.5a_1$, a3 changes depending on the changing of the opposite angle θ_3 from $0°$ to $360°$. The chirality index K, defined by the four different formulas, is plotted as a function of θ_3. (the code is in Appendix A-2)

Figure 6-4: The chirality of triangles with sides $a_1=1$, $a_2=.7a_1$, a_3 changes depending on the changing of the opposite angle θ_3 from 0° to 360°. The chirality index K, defined by the four different formulas, is plotted as a function of θ_3. (the code is in Appendix A-3)

6.2.2   Sensitivity to Chirality

To investigate the behaviour of the four models when a shape has trivial changes, consider the five different shapes in Figure 6-5. The shape in (6-5a) is an achiral pattern in a square shape, and the four other shapes are constructed by modifying the square slightly, which result in one achiral pattern in envelope shape in Figure (6-5b) and three chiral shapes in Figures (6-5c), (6-5d), and (6-5e). After pixelating these shapes, the chirality K was calculated by using the four different models. In general, all of the models seem sensitive when the shape change from achiral to chiral. Chirality tends to be zero if the shape has symmetry, such as the square in Figure (6-5a) and the envelope shape in Figure (6-5b). However, chirality acquires a considerable value as a result of chiral shapes, such as those in Figures (6-5 c), (6-5 d), and (6-5 e). It should be noted that the chirality K of the shapes in Figures (6-5 c) and (6-5 d) has the same value as the shapes are the same under the rotation operation.
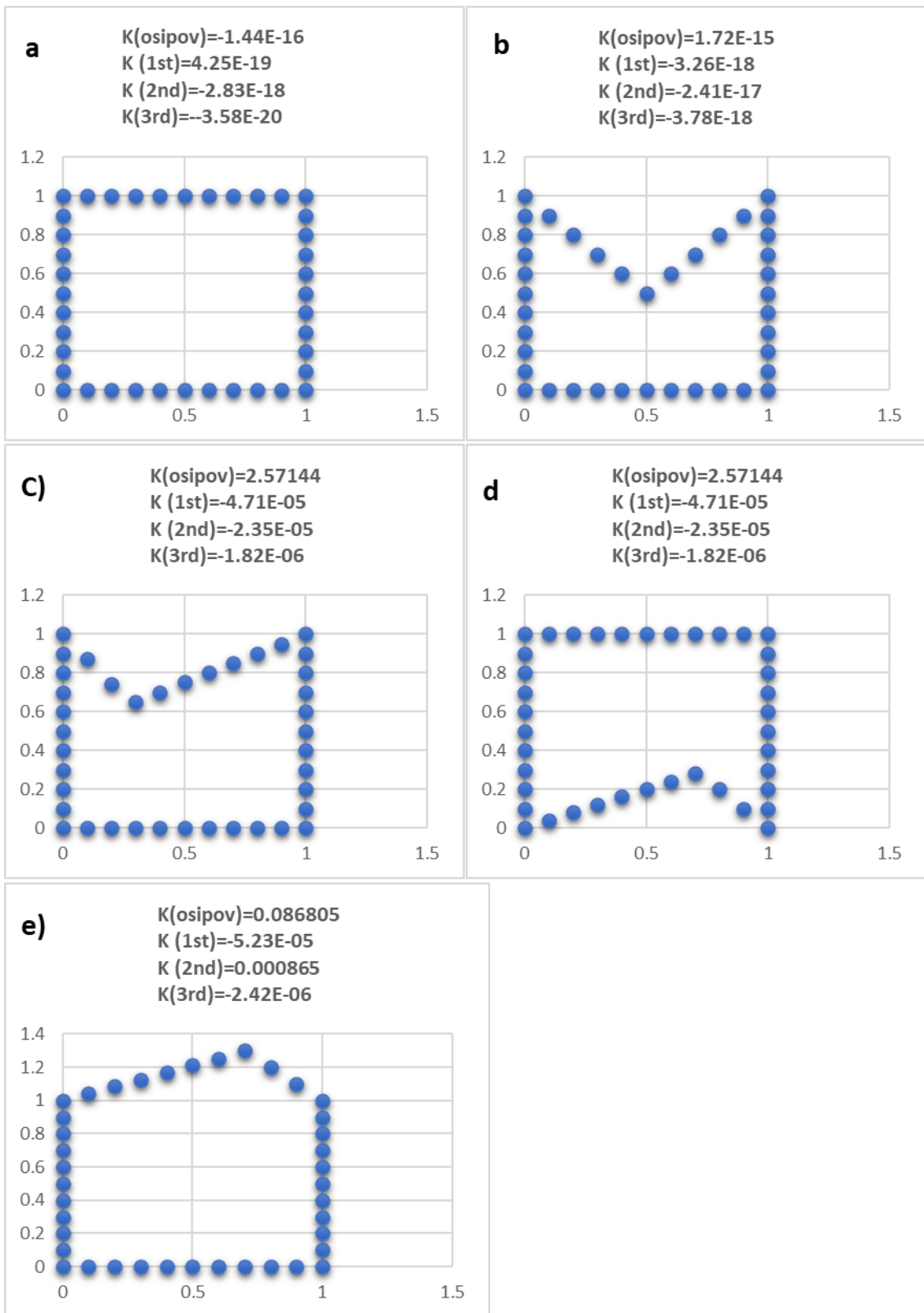
Figure 6-5: Chirality values K obtained based on the four models for different shapes. K tends to be zero for a) square and b) envelope as achiral shapes; however, the value of K becomes considerable for any small change that results in a chiral shape, like figures c), d), and e), l

45

6.2.3   Limitations

These models are not without limitations. One major limitation is that they are all reliant on the area, not just the shape, which make the comparison between different structure with different area not accurate.
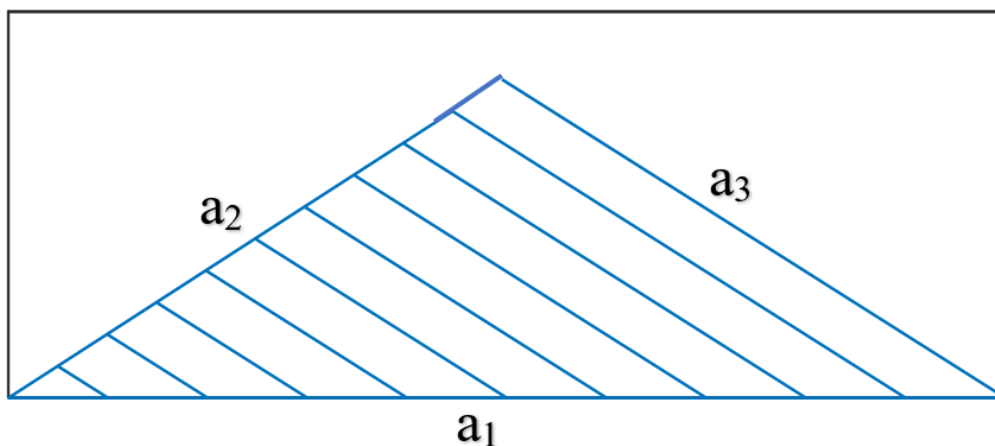
Figure 6-6: Triangles with the same angles but different area.

Let us consider the following situation (see Figure 6-6): similar triangles with fixed angles but different sides where the first side a_1 changes from 1 to 10 units, and the second side $a_2 = 0.7a_1$, while the third side a_3 changes but the opposite angle is kept fixed as $\theta_3 = 45°$. The chirality K is calculated using the three models proposed by Potts *et al.* (2003) and plotted as a function of the area in Figure (6-7). As shown in the figure, when the area of the triangle increases, the chirality, as defined by the Potts' models, decreases linearly, although the shape does not change. Note that the chirality index decreases with negative values, which means that the degree of chirality increases as the area increases.
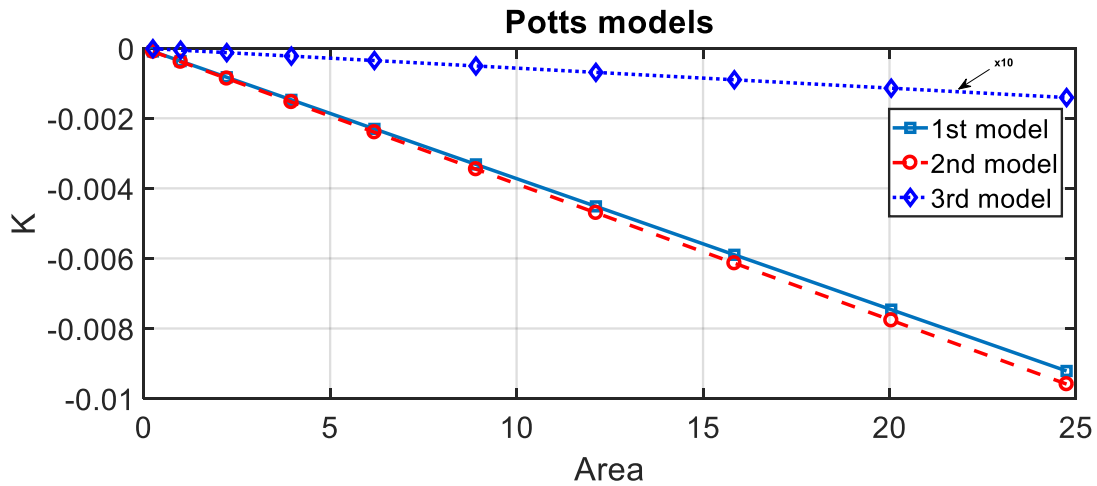
Figure 6-7: The relationship between the chirality and the area of similar triangles. (the code is in Appendix A-4)

6.2.4 The Most Chiral Triangle

Attempting to identify the most chiral triangle is a complex task (Rassat and Fowler, 2003). To compare the chirality of triangles with a fixed area, consider the area of triangles is settled to be equal to a unit by choosing triangles with points (0,0), (0,1), and $(x_3,2)$ where x_3 takes different values over the interval [-10, 10]. This is exemplified by the triangle in Figure (6-8).
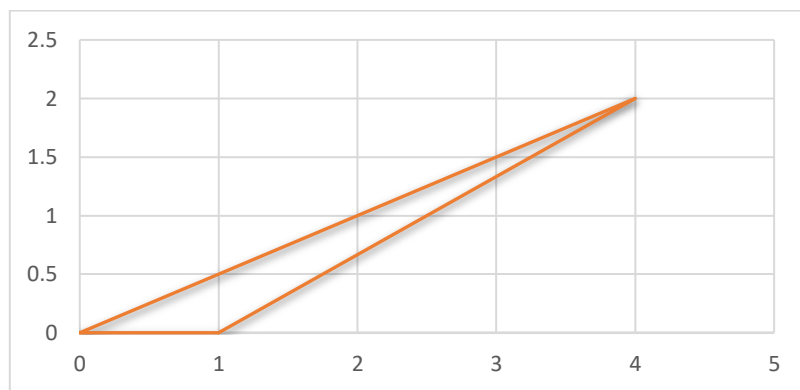

Figure 6-8: The area of triangles is fixed to be equal to a unit by choosing triangles with points (0,0), (0,1), and $(x_3,2)$, where $x_3=4$ here as an example. (the code is in Appendix A-5)

The four different models (Potts *et al.*, 2003) facilitate the calculation of chirality, which can then be plotted as a function of x_3 values. As seen in Figure 6-9, the Osipov model and Potts 3rd model show different extremum values around at $x_3=\pm1.3$, ±5, respectively, which indicate the most chiral triangle. However, Potts' 1st and 2nd models do not indicate the maximum value.
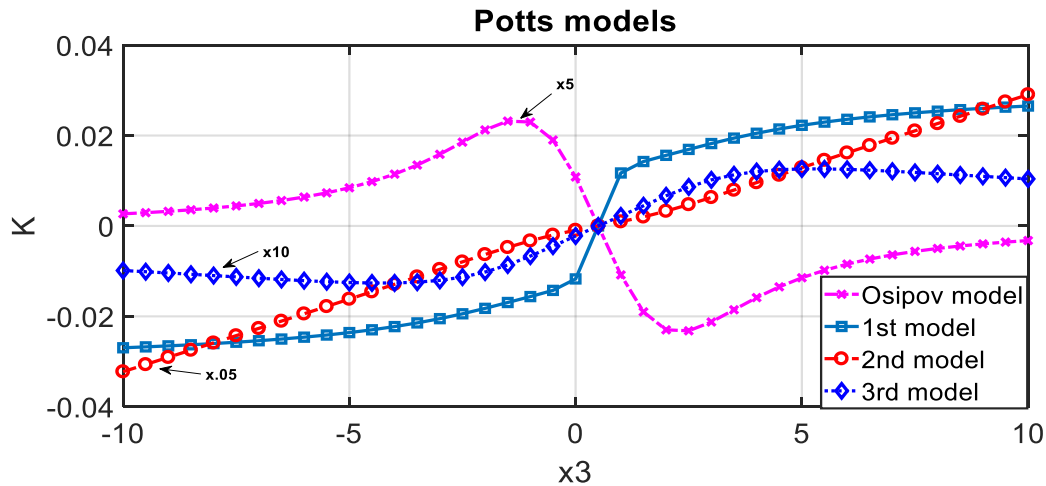
Figure 6-9: The chirality of triangles with fixed area calculated using the four different models and plotted as a function of x_3 (as explained in Figure 6-8). The Osipov model and Potts 3rd model show different extremum value, while Potts' 1st and 2nd models do not indicate the maximal value.

6.3 Chirality Index of Gammadion Patterns

By using Osipov and Potts models (Potts *et al.*, 2003), the chirality index K was calculated for gammadion patterns as a function of the bending angle (β) of the gammadion arm (the gammadion shape illustrated in Figure (6-10).
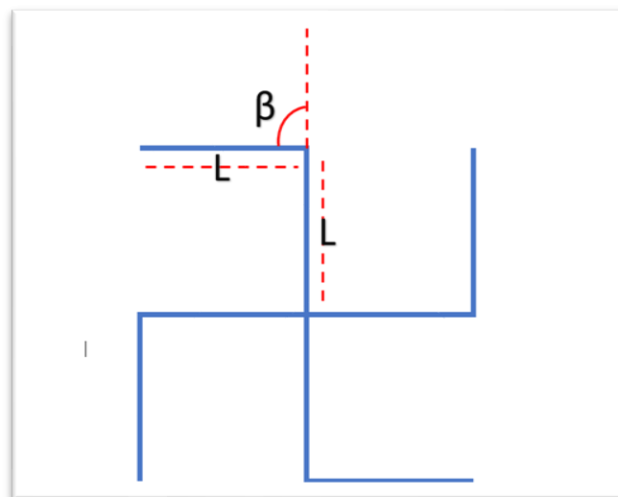

Figure 6-10: Gammadion shape, β is the bending angle of the arm and L is arm length.

Similar to the work done by Potts *et al.* (2003), the chirality index K is calculated by using different pixelating of the shape: 0.1L, 0.05L, and 0.025L, where L=1 is the length of the gammadion arm. Then, K values were calculated by summing over the chirality of all possible triangles performed with three points in the clockwise

direction. The following figures show the chirality K of gammadion patterns using the four different models: Figure (6-11) Osipov model, Figure (6-12) Potts 1st model, Figure (6-13) Potts 2nd model, and Figure (6-14) Potts 3rd model. The figures show that the result of the case of the Osipov model changes significantly when the pixelating of the shape change, while the Potts 1st, 2nd, and 3rd models appear almost no change (Potts *et al.*, 2003).
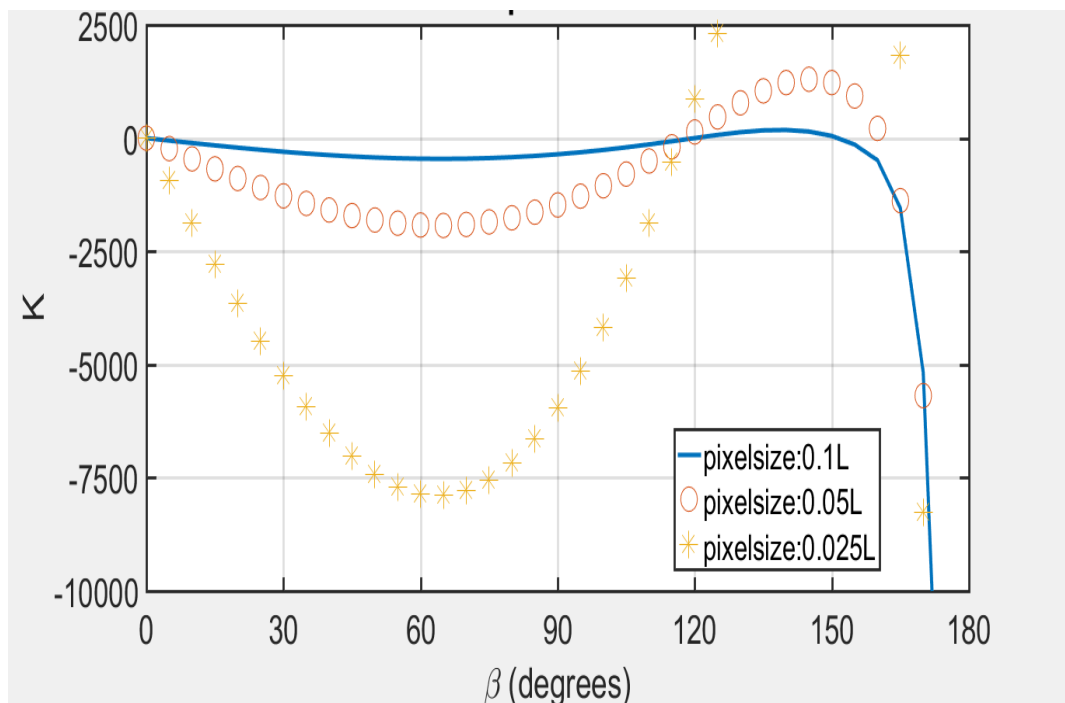

Figure 6-11: Chirality index K by using Osipov model for gammadion patterns as a function of the bending angle of the arm (β), with three different pixelating of the pattern: 0.1L, 0.05L, and 0.025L, where L is the arm length
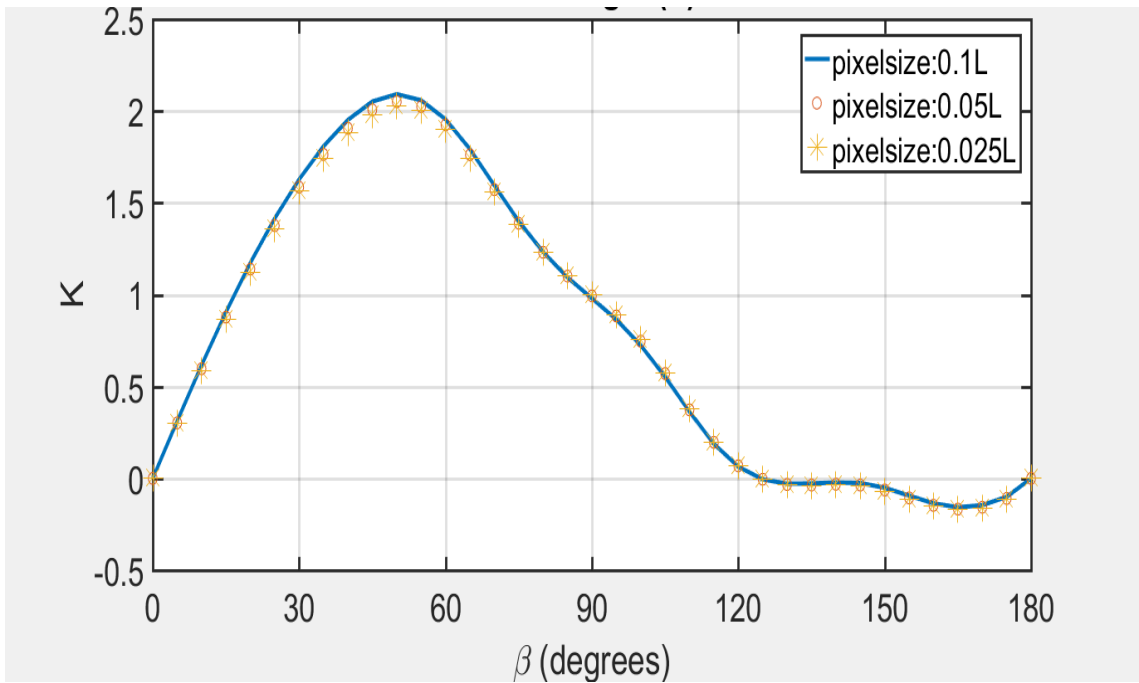
Figure 6-12:Chirality index K by using Potts 1st model for gammadion patterns as a function of the bending angle of the arm (β), with three different pixelating of the pattern: 0.1L, 0.05L, and 0.025L, where L is the arm length

Figure 6-13:Chirality index K by using Potts 2nd model for gammadion patterns as a function of the bending angle of the arm (β), with three different pixelating of the pattern: 0.1L, 0.05L, and 0.025L, where L is the arm length

Figure 6-14:Chirality index K by using Potts 3rd model for gammadion patterns as a function of the bending angle of the arm (β), with three different pixelating of the pattern: 0.1L, 0.05L, and 0.025L, where L is the arm length
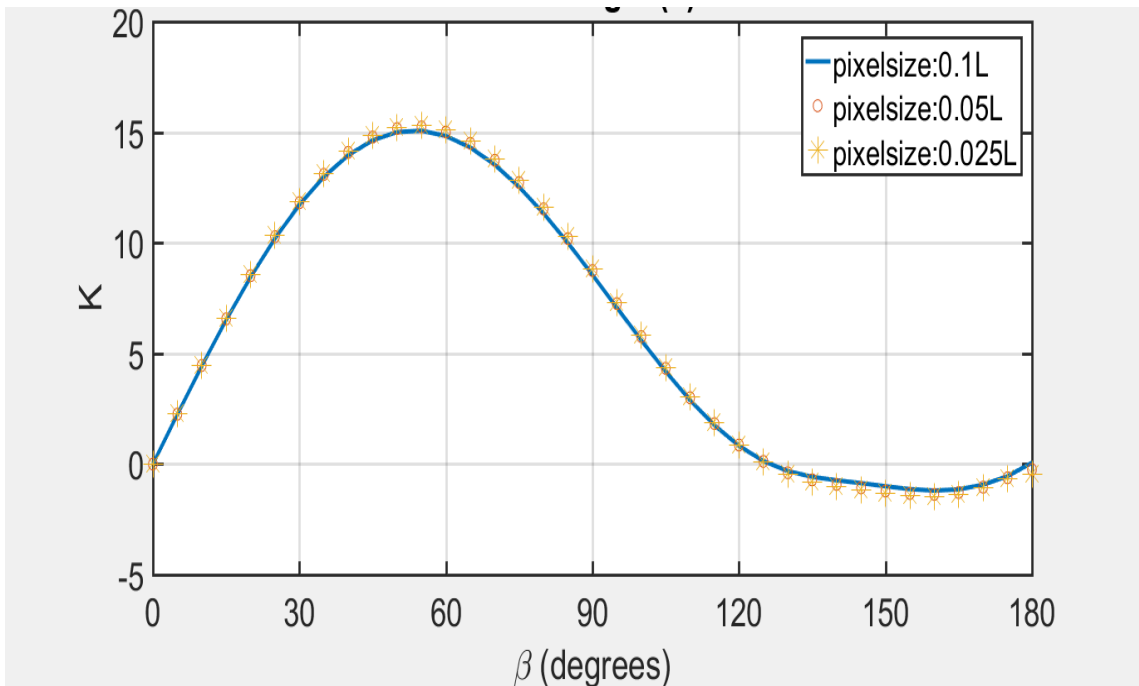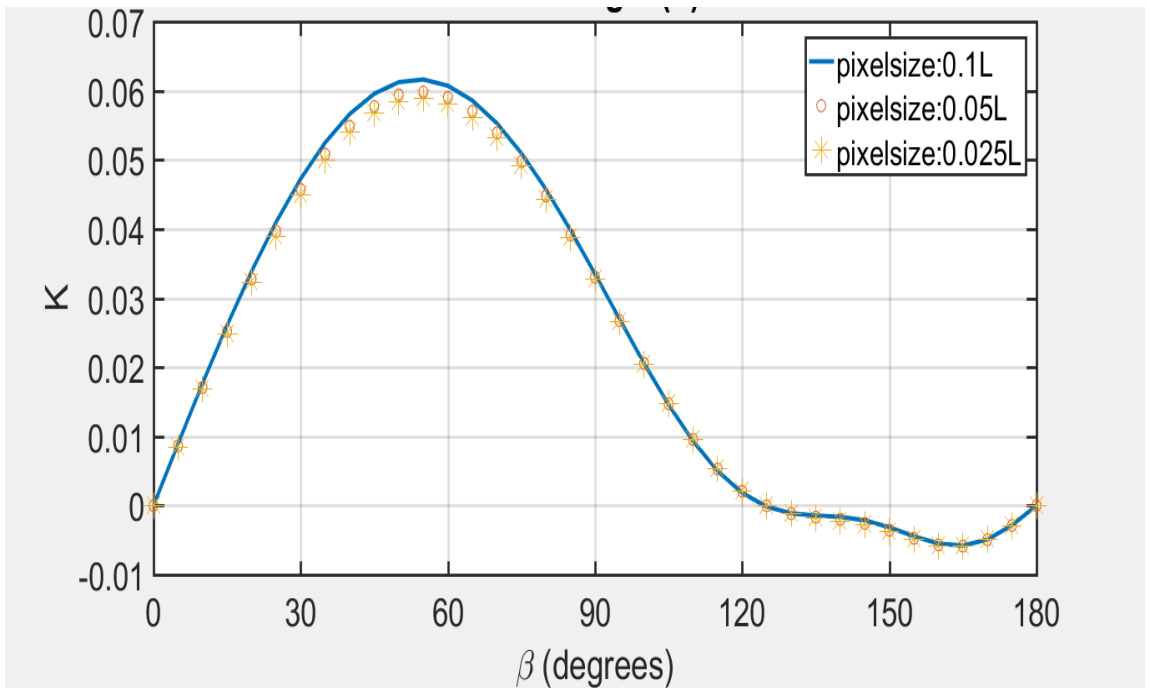
7   Experimental Results

The experimental measurements presented in this chapter were collected using a dual-PEM polarimeter (illustrated in section 5.3) and the polarimetric imaging microscope (described in section 5.6). In this work, the polarimetric microscope was operated in transmission mode, with the light passing through the PSG and the sample before reaching the PSA. The PSG consisted of a light source, a rotatable polariser to generate various linear polarised light. In some experiments, a rotatable quarter waveplate was used to generate various circular polarised light. The PSA part consisted of two photoelastic modulators and an analyser. The data acquired by using a digital camera. The polarimetric microscope was computerised using LabView, and appropriate Python codes were used to analyse the collected data.

In general, this chapter presents the calibration data of the system using three different light resources. Also, the experimental results of measuring Stokes parameters by using multiple samples are offered. Hence these parameters can be used in turn to determine other optical properties such as the angle of ellipticity, the azimuth angle, the degree of polarisation and the degree of depolarisation.

7.1 Sample Description

In order to study the optical responses of chiral materials, several multiple samples in gammadion shapes with different bending angles (β) were patterned. One pattern of these samples is achiral structures, while others are chiral structures. There are also spiral-shaped patterns and five-folded shapes. All these samples were created in an external production facility in China. Figure 7-1 and 7-2 show and label the dimensions of gammadion and spiral pattern, while Table 7-1 lists the value of the dimensions in each pattern.
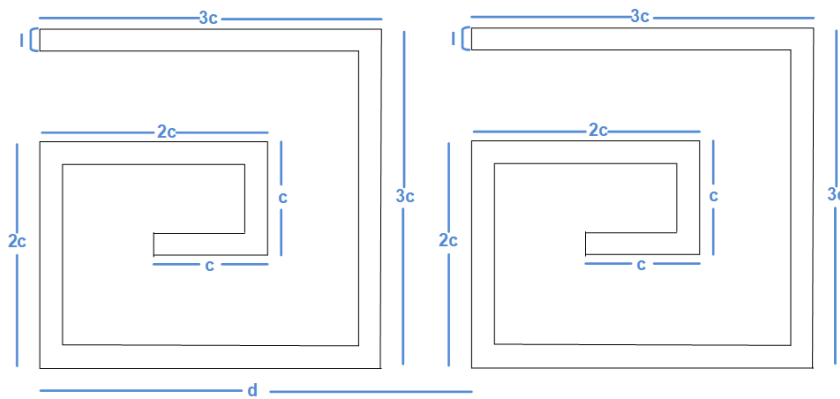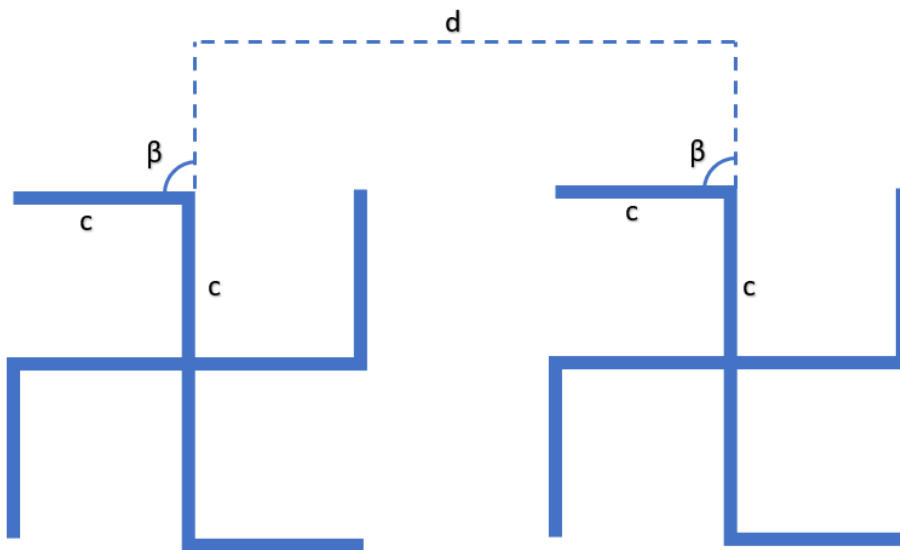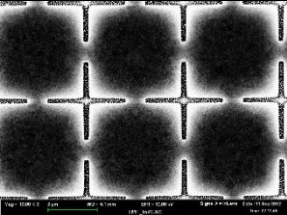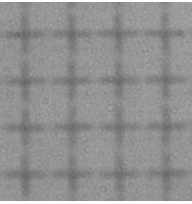

Figure 7-1: Spiral-shaped patterns.
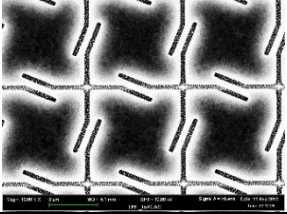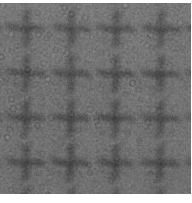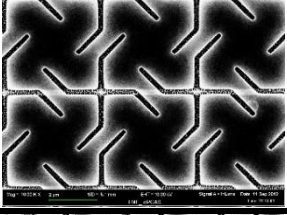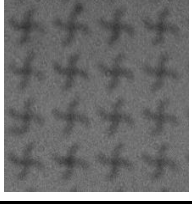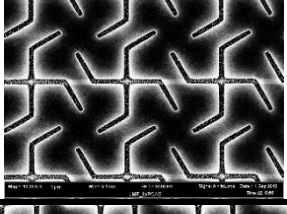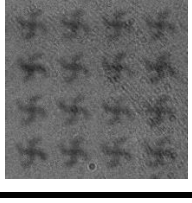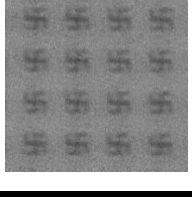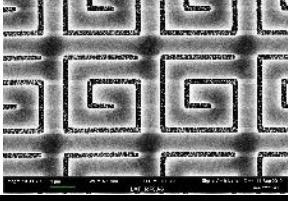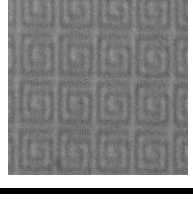
Figure 7-2: Gammadion-shaped patterns.

Table 7-1: The value of the dimensions in each pattern of the experimental samples. The symbols (β, d, and c) are defined in Figures 7-1 and 7-2; microscope images captured using 100x objective lens with 1.6x immersion oil.

Shape	β (°)	d (μm)	c (μm)	Manufacturer SEM images	Polarised Microscope image
Gammadion G0	0	4	1.40		
Gammadion G22.5	22.5	4	1.40		
Gammadion G45	45	4	1.40		
Gammadion G60	60	4	1.40		
Gammadion G90	90	4	1.40		
Spiral	-	4	1		

The pattern G0 is an achiral shape, while the other patterns are chiral shapes, and it might be right- or left-handed.

The samples were arranged in 25 different arrays with spaces between them of around 2mm. Each array consisted of a periodic arrangement of identical patterns in two dimensions. The pattern was etched on a silicon nitride layer of 320 nm thickness placed upon a fused silica substrate layer of 1 mm thickness. The width of the etched line was thus about 200 nm, as shown in the schematic diagram in Figure 7-3.
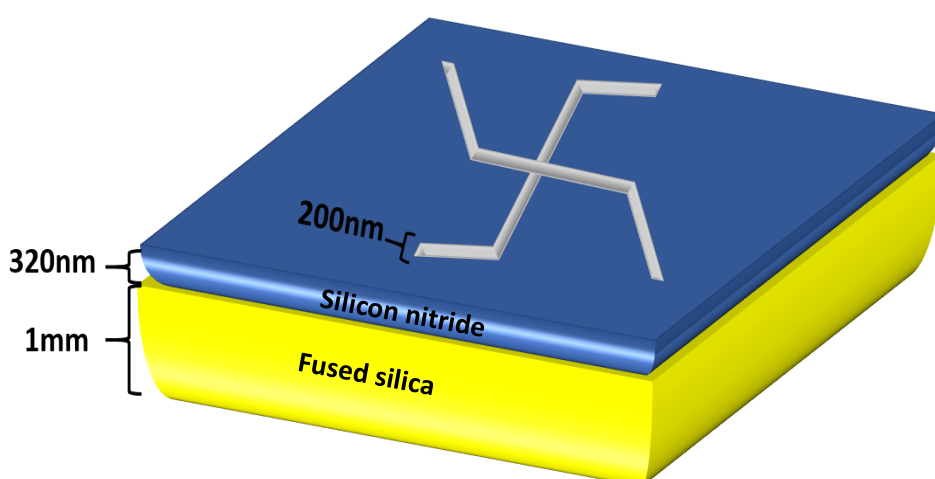
Figure 7-3: Schematic representation of a gammadion sample.

7.2   Calibration

The calibration procedure characterises the PSA, and thus should be performed periodically to achieve higher accuracy in measurement. In order to determine k_i elements where i=1, 2, 3, ….,8 prior to adding any sample, the dual PEM polarimetry was calibrated following the steps illustrated in detail in section 5.5. During the calibration procedure, linear and circular polarised light passed through the PSA using polariser and QWP. Then, the four experimental signals, I_{DC}, I_{QU1}, I_{QU2}, and I_V, were measured and, based on equation (5-17), Stokes parameters were calculated. The total error was calculated as follows:

$$\varepsilon_{total} = \Delta I + \Delta \psi$$

where ΔI is the difference between the experimental and theoretical value of Stokes parameter I, while Δψ is the difference between the experimental and theoretical value of azimuth angle. By using an Excel solver, the ki constants were obtained simultaneously by minimising the total errors.

7.2.1 Calibration of the Dual PEM System (using a 670-nm laser)

Following the steps in section 5.5, a system of two PEMs (Hinds Instruments) with different frequencies Ω_1=42 kHz and Ω_2=50 kHz; and Glan-Thompson(Karl Lambrecht) analyser was calibrated by using a laser light of wavelength 670 nm, acting as a light source, and a photodiode detector (Melles Griot). The calibration constants, ki, are listed in Table 7-2, along with the value of total error ε_{total}. The normalised Stokes parameters q=Q/I, u=U/I, and v= V/I are plotted in Figure 7-4 as a function of the angle of the polariser by using circular and linear polarised light. Note that in Figure 7-4a, q remains positive, although that not fully understood.
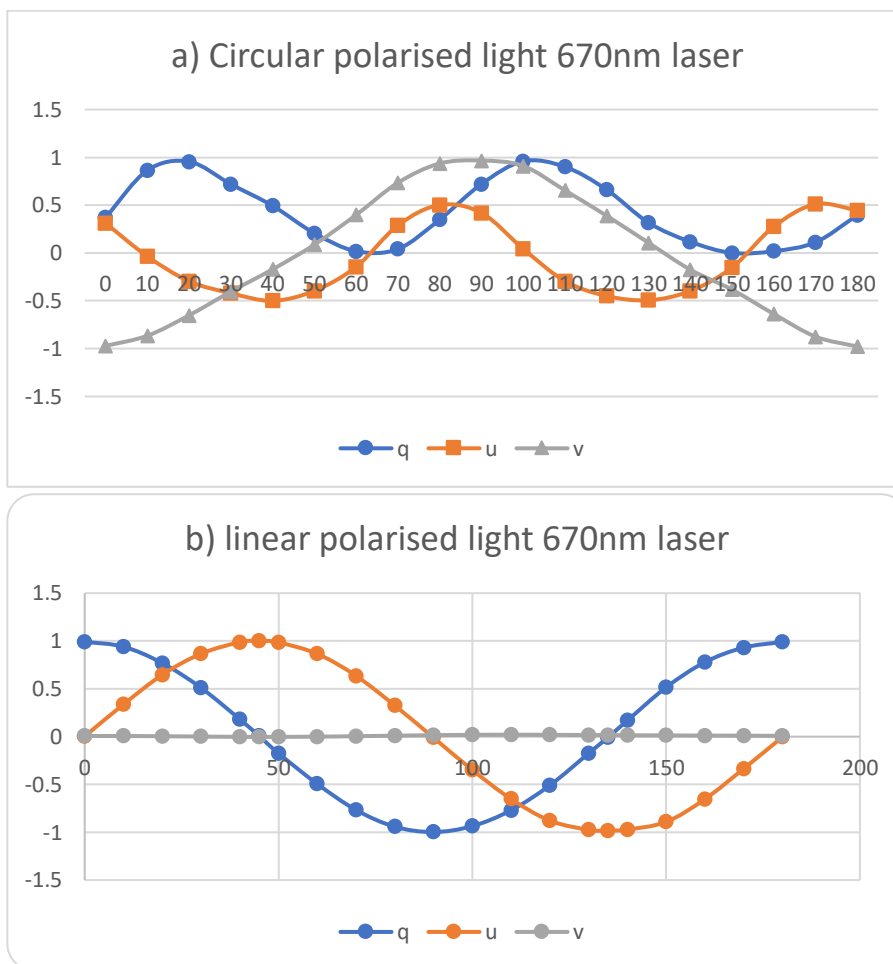
Table 7-2: calibration constants ki with the total error ε_{total} for dual PEMs configuration with 670-nm laser light.

With 670nm laser	
k1	1
k2	0.350381062
k3	0.362692492
k4	2.313098818
k5	-0.036551535
k6	0.069754952
k7	2.215441109
k8	3.46277614
ε_{total}	3.22E-02

Figure 7-4: The normalised Stokes parameters q, u and v for the dual PEMs polarimetry with 670-nm laser as a polarised light: a) circular and b) linear. Lines drawn between data points are intended to be a guide to the eye.

7.2.2 Calibration of the Polarimetric Microscope (using 445- nm LED)

As explained in Section 5.5, the calibration process was used to identify the eight constants of the polarimetric microscope (k_i, i=1,2, …,8). The microscope was then calibrated by using a LED with a wavelength of 445 nm as a light source. The frequencies of PEM1 and PEM2 were Ω_1=42 kHz and Ω_2=47 kHz, respectively. A quarter-wave plate (QWP) was used to generate the required circular polarisation states. The calibration constants k_i are listed in Table 7-3 with total error ε_{totoal}, while Figure 7-5 shows the normalised Stokes parameters q, u, and v.
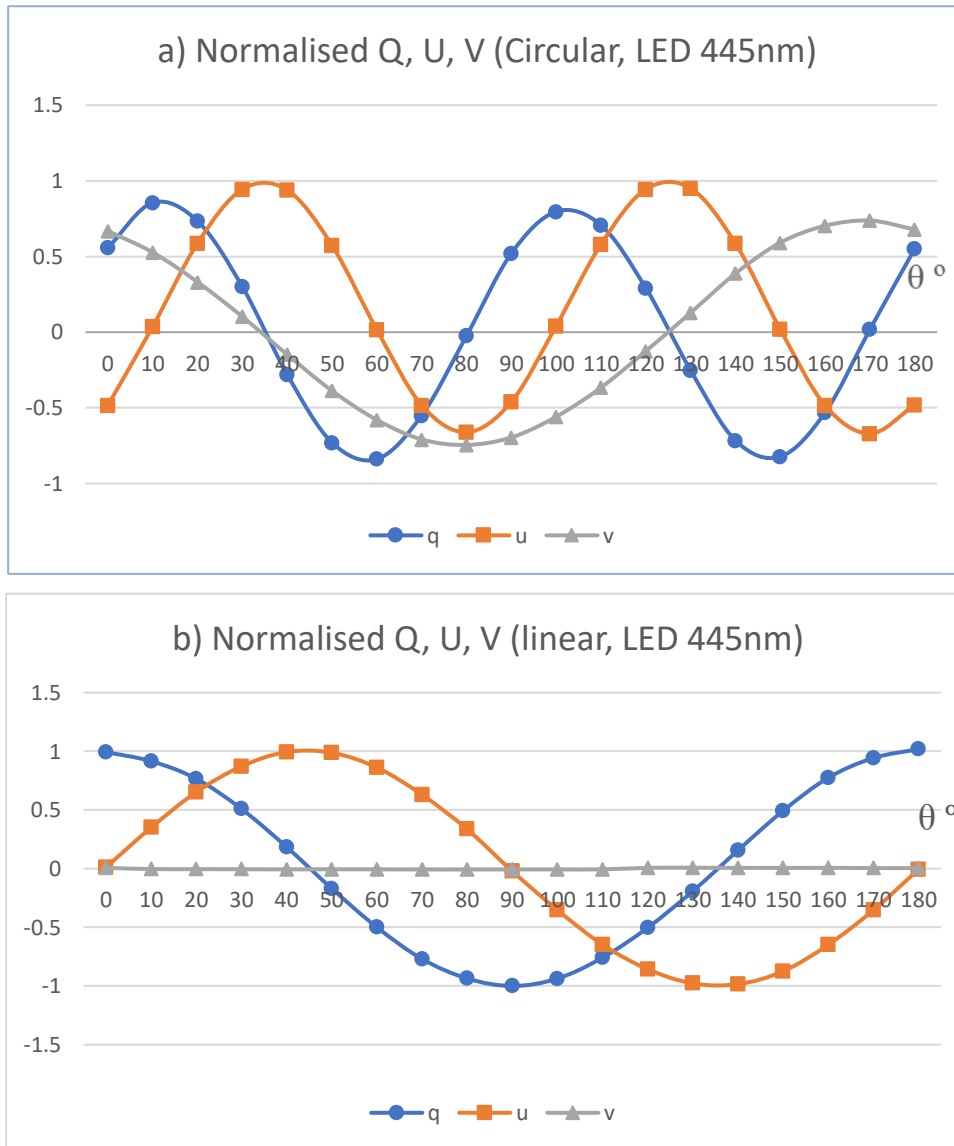
Table 7-3: calibration constants ki (i=1, 2, ….8) with the total error ε_{total} for polarimetric microscope using 445-nm LED.

With LED 445nm	
k1	1
k2	0.214435081
k3	2.030462941
k4	0.726620156
k5	-5.769474153
k6	-5.056997556
k7	-1.141747266
k8	4.349517707
ε_{total}	0.034613285

Figure 7-5: The normalised Stokes parameters q, u, and v for the polarimetric microscope with 445- nm LED as a light source for a) circularly polarised light and b) linear polarised light. Lines drawn between data points are intended to be a guide to the eye

7.2.3   Calibration of the Polarimetric Microscope (using 660- nm LED)

Aside from the fact that the light source was LED of 660-nm wavelength, the process was the same as in the previous section. The calibration result of the polarimetric microscope is shown in Figure 7-6, where Figure 7-6a shows normalised Stokes parameters of circularly polarised light, while Figure 7-6b shows normalised Stokes parameters of linear polarised light. Table 7-4 summarises the calibration constants (k_i, i=1,2, …,8) and the total error ε_{totoal}. Note that in Figure 7-6a u is nearly negative but that not the case in Figure 7-5a; although that the difference between the two experiments is just the light wavelength, this features is not fully understood

a)Normalised Q, U, V (Circular, LED 660nm)

With LED 660nm	
k1	1
k2	0.02911742
k3	4.644286161
k4	2.142209116
k5	-9.103065789
k6	3.514125234
k7	4.144227242
k8	2.819710344
ε$_{total}$	0.032891858

b)Normalised Q, U, V (linear, LED 660nm)

Figure 7-6: The normalised Stokes parameters q, u, and v for the polarimetric microscope with 660-nm LED as a light source for a) circularly polarised light and b) linear polarised light. Lines drawn between data points are intended to be a guide to the eye

7.3 Calculation of Stokes Parameters

A gammadion shape was measured in transmission mode by using a polarimetric microscope. Normalised Stokes parameters and normalised depolarisation were calculated. The light source was a 445nm LED, and the polarimetric microscope equipped with a 40x objective lens with 1.6x immersion oil. The results are shown in Figure 7-7.
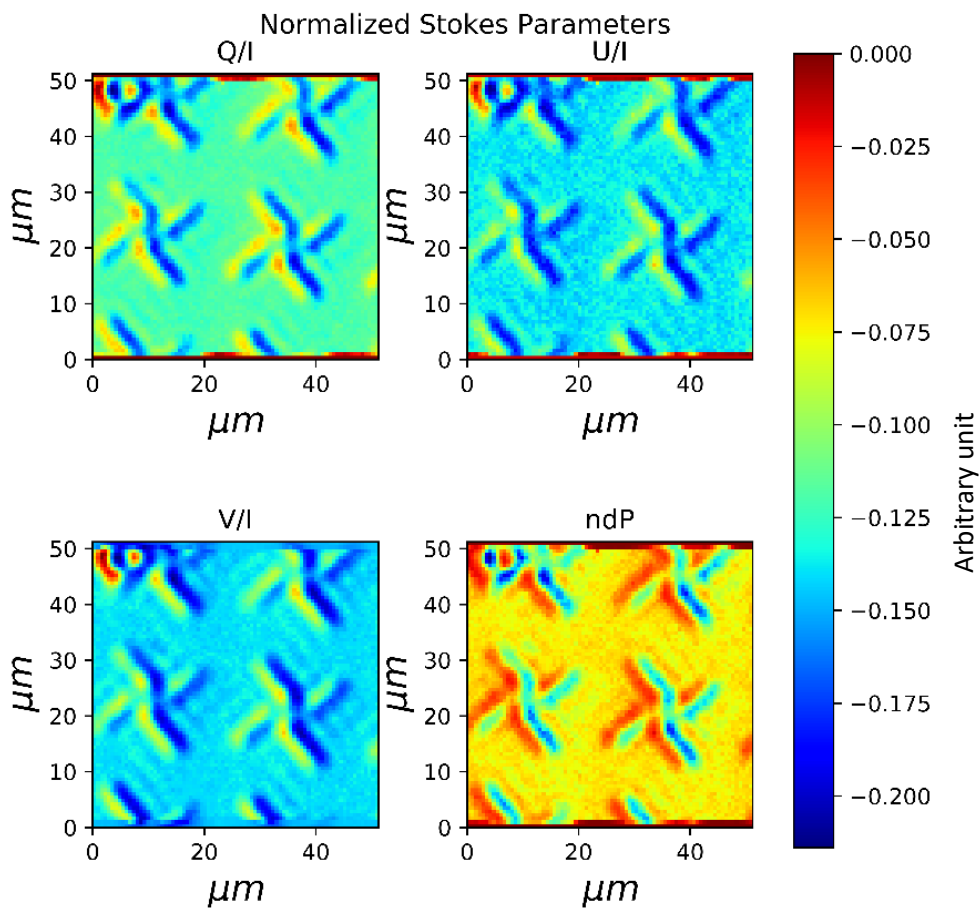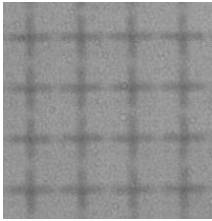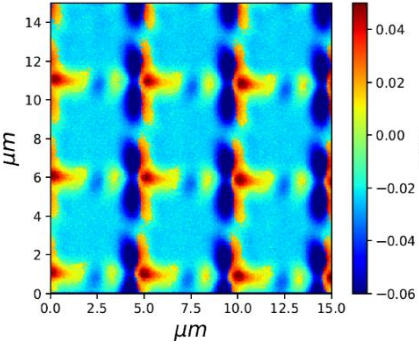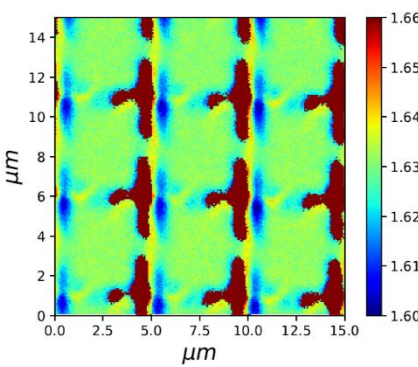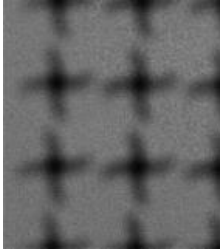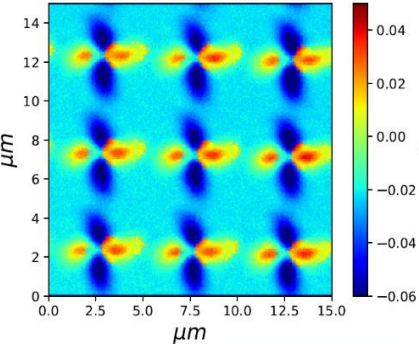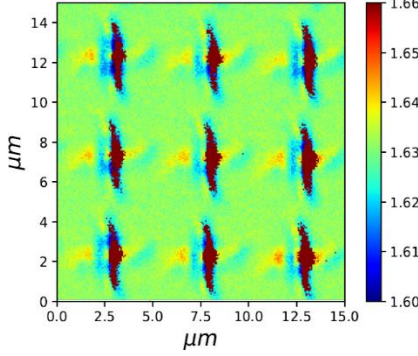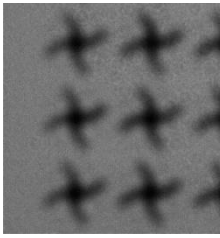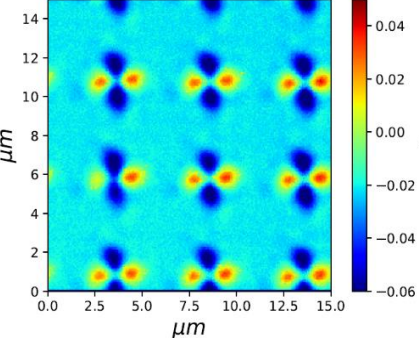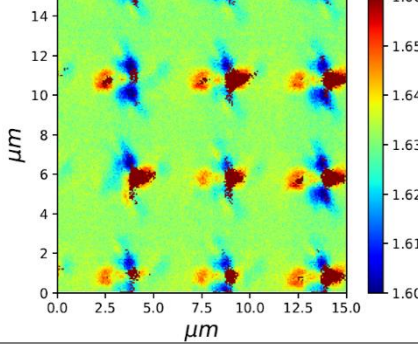
Figure 7-7:Normalised Stokes parameters (Q/I, U/I, V/I) and normalised depolarisation (ndP) of a pattern in gammadion shape (G45 as illustrated in Table 7-1) by using (455-nm LED and 40x objective lens with 1.6x immersion oil).

7.4   Calculation of Ellipticity and Azimuth Angles

Both the ellipticity and azimuth angles were calculated using the data of Stokes parameters measured for different patterns of gammadion shapes by using the polarimetric microscope. All the measurements were obtained under the same conditions using a 445 nm LED as a light source and a 100x objective lens with 1.6x immersion oil.

Table 7-5: Ellipticity (χ) and azimuth (ψ) angles of different patterns (as illustrated in table 7-1) by using LED 455 nm and 100x objective lens with 1.6x immersion oil.

Pattern name	Photo of the pattern	Ellipticity angle (χ) (rad)	Azimuth angle (ψ) (rad)
G0			
G22.5			
G45			

Pattern name	Photo of the pattern	Ellipticity angle (χ)	Azimuth angle (ψ)
G60			
G90			
5-folded shape			

Pattern name	Photo of the pattern	Ellipticity angle (χ)	Azimuth angle (ψ)
6-folded shape			
Z-shape			
RH Spiral			
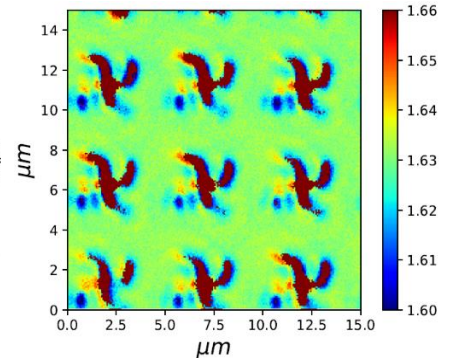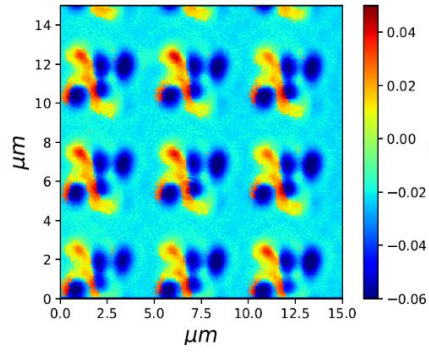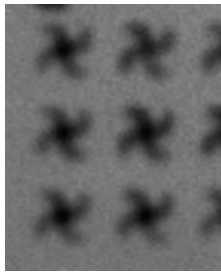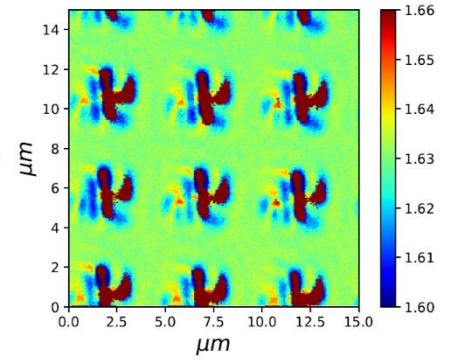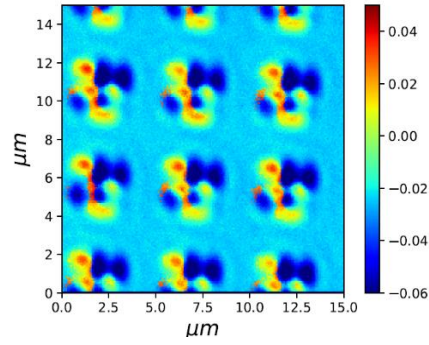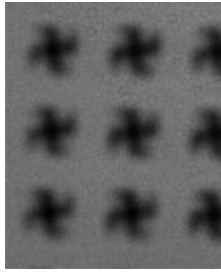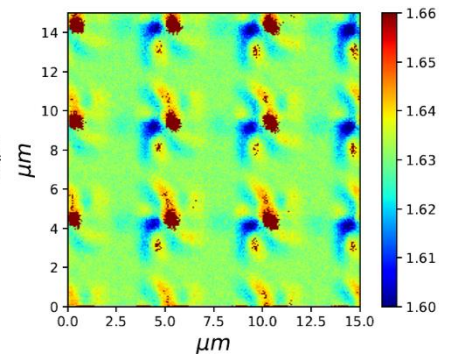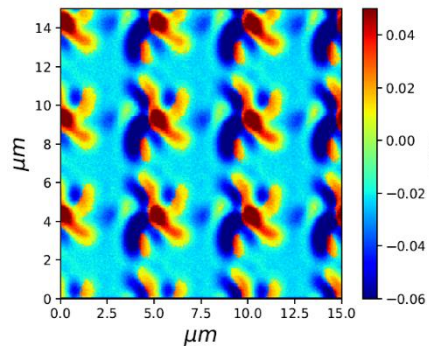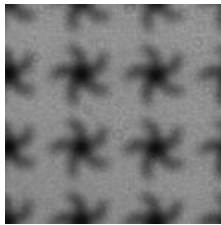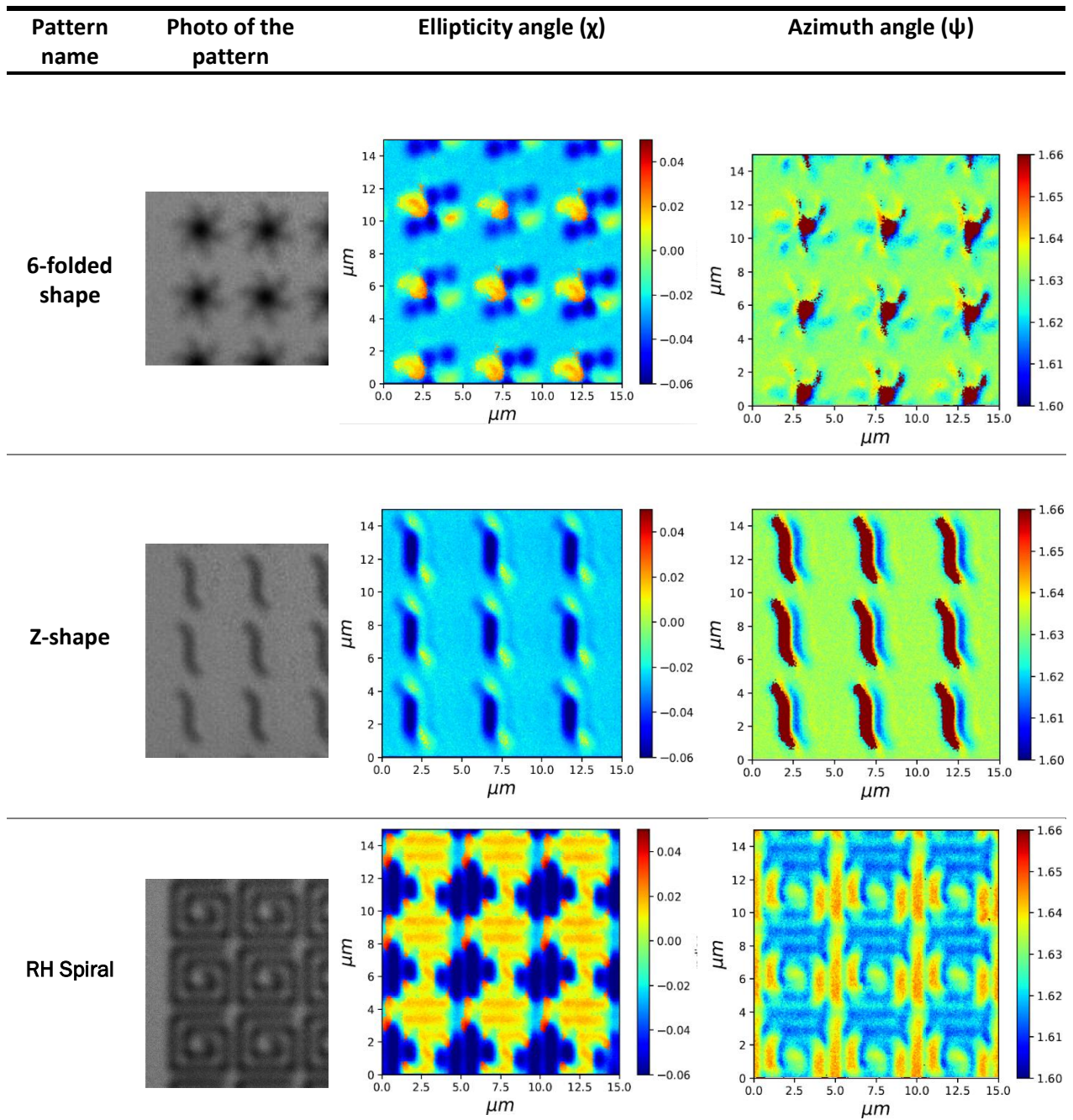
As illustrated by the Figures in Table 7-5, the experimental results show that the ellipticity angle and the azimuth angle depend on the shape of the planar samples.

Also, this study took advantage of the availability of a rotatable polariser to obtain measurements of the samples with different polariser angles. In practice, the same light source was used throughout to allow the 2D values of the ellipticity angle and azimuth angle to be determined along with the rotation of the polariser angles from 0 º to 110º. The results are shown in Figures 7-8(a-l) and 7-9(a-l).
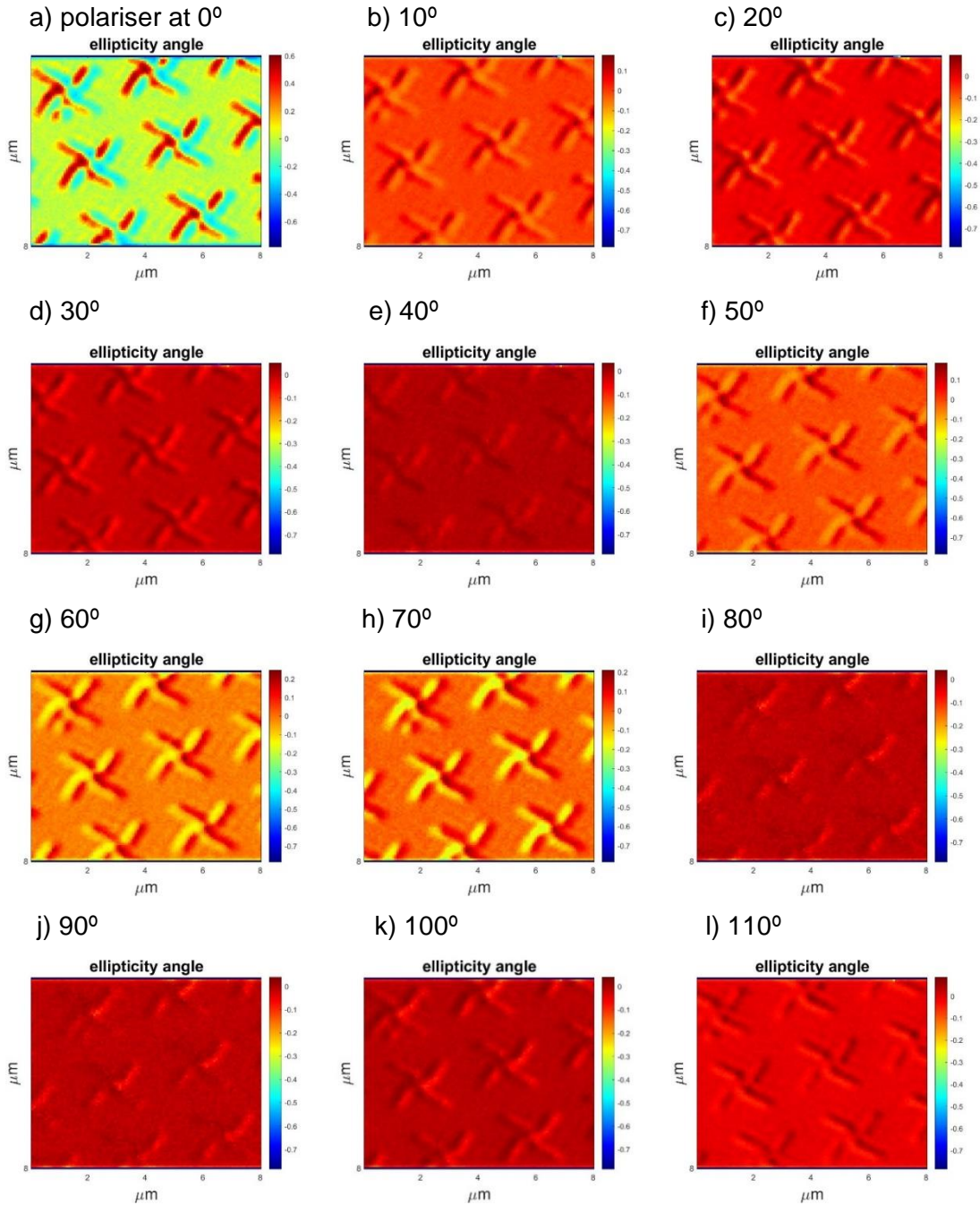
Figure 7-8: Ellipticity angle (χ) in radian of a pattern in gammadion shape (G45 as illustrated in Table 7-1) with changing the polariser angle using 455-nm LED and 40x objective lens with 1.6x immersion oil.
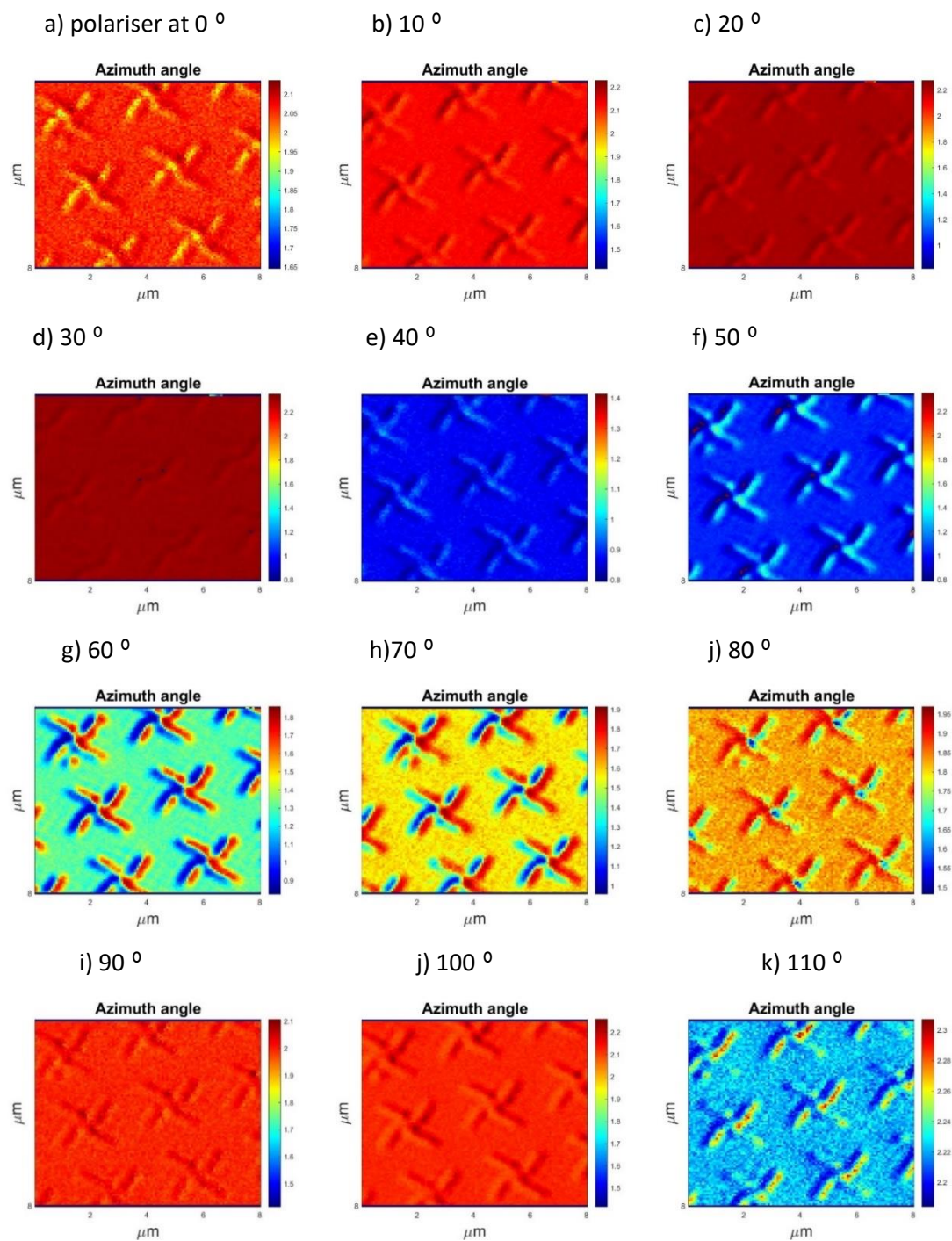
Figure 7-9: Azimuth (ψ) angles in radian of a pattern in gammadion shape (G45, as illustrated in table 7-1) with changing the polariser angle using LED 455nm, 40x objective lens with 1.6x immersion oil.

The following results thus present experimental data that contains additional information about the sample, where the sample was rotated while it was being measured at each 10º. The ellipticity angle and azimuth angle of one pattern in a gammadion shape were calculated based on the data collected during rotation of the sample from (0º -60º) as shown in Figure 7-10 and 7-11.

a) sample at 0⁰ b) 10⁰ c) 20⁰

d) 30⁰ e) 40⁰ f) 45⁰

g) 50⁰ h) 55⁰ i) 60⁰
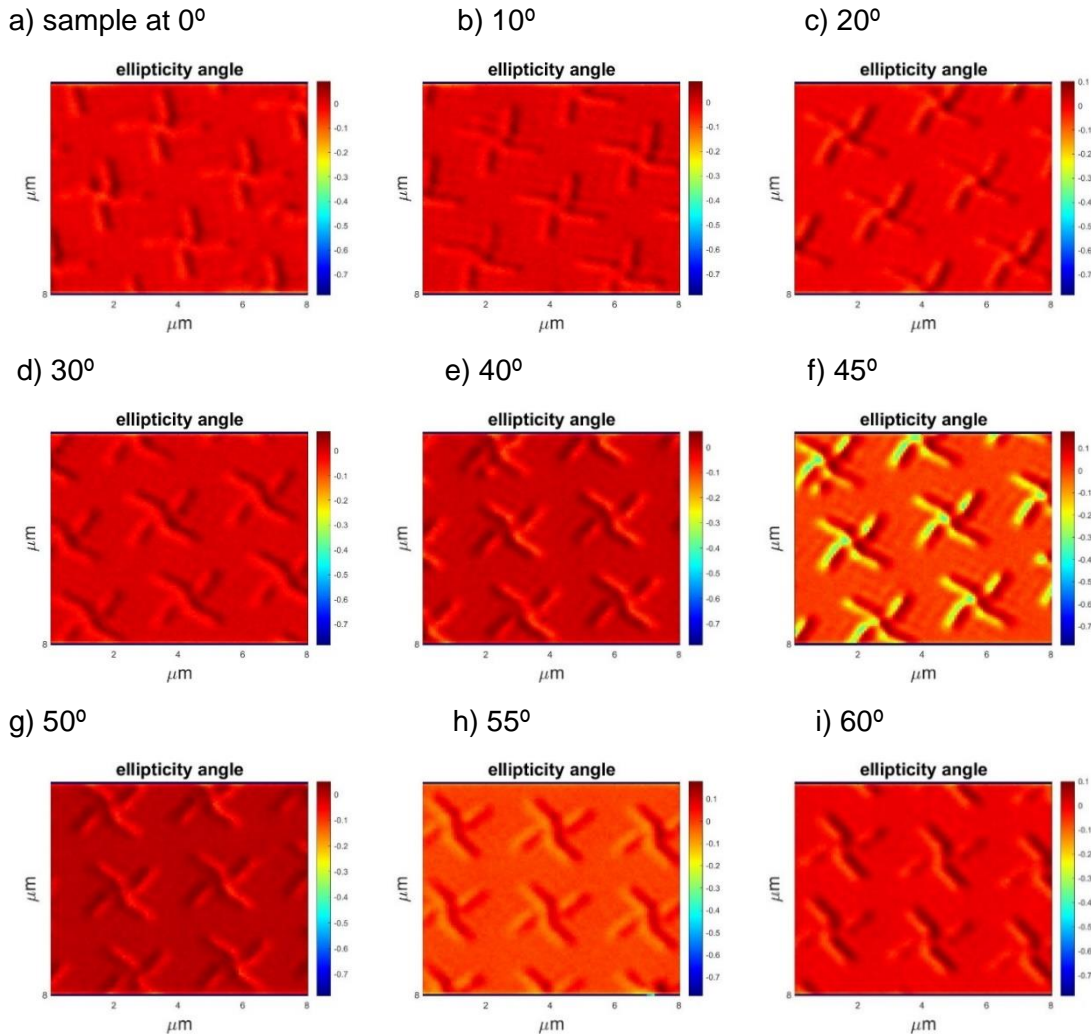
Figure 7-10: Ellipticity (χ) angle in radian of a pattern in gammadion shape (G45, as illustrated in Table 7-1) with rotation of the sample by using 455-nm LED 40x objective lens with 1.6x immersion oil.

a) sample at 0⁰

b) 10⁰

c) 20⁰

d) 30⁰

e) 40⁰

f) 45⁰

g) 50⁰

h) 55⁰

i) 60⁰
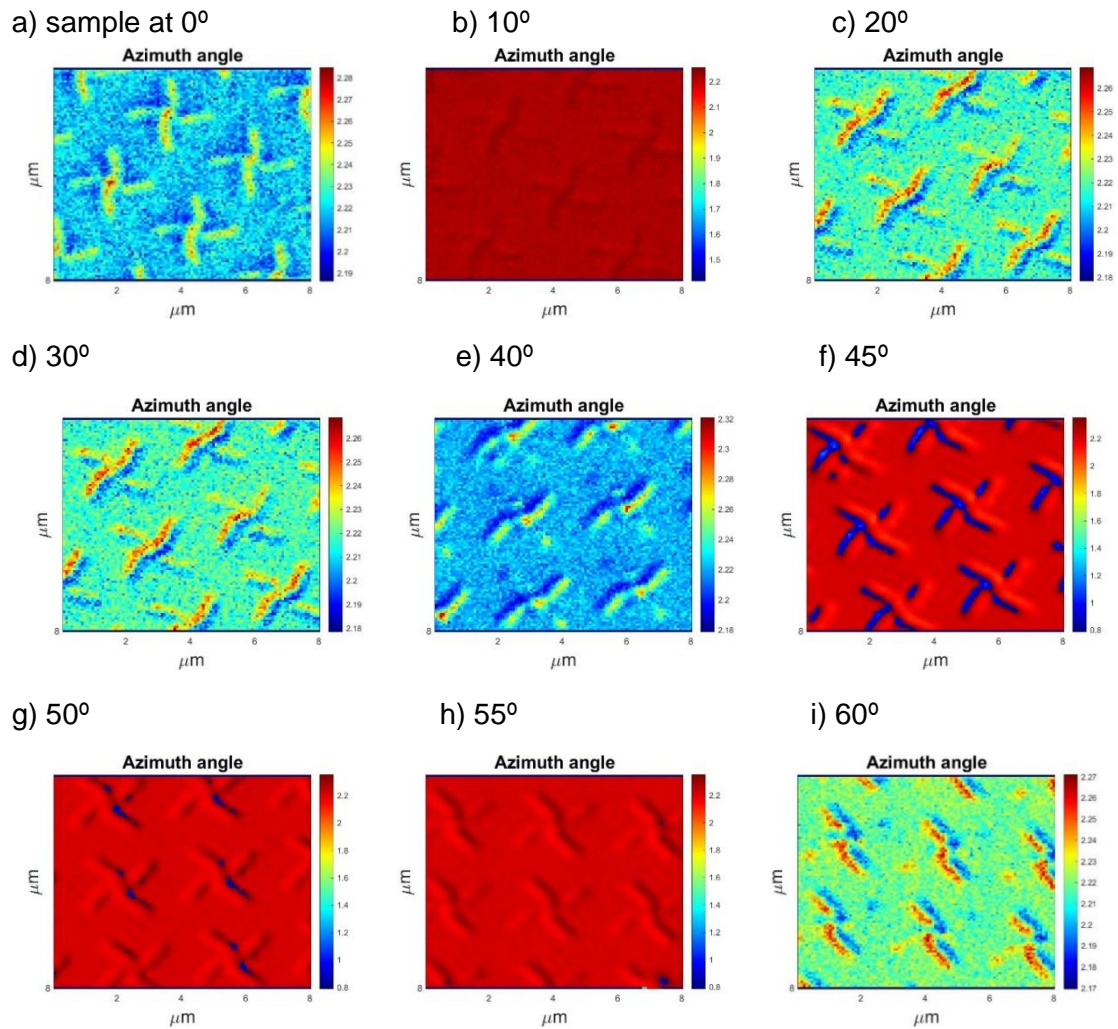
Figure 7-11: Azimuth (ψ) angles in radian of a pattern in gammadion shape (G45, as illustrated in Table 7-1) with rotation of the sample by using 455-nm LED and 40x objective lens with 1.6x immersion oil.

As clearly seen by the Figures in this section, the polarimetric microscope has the ability to determine the ellipticity and azimuth angles for different sitting for the sample or the polariser.

7.5   Calculation of the Mueller Matrix of a Gammadion Pattern:

One of the most promising uses of the polarimetric microscope is to calculate the Mueller matrix of a given sample. The imaging technique offers excellent opportunities to discerning the Mueller matrix in each pixel of the sample. One of the main reasons behind the experiment presented in this section is to showcase the polarimetric microscope's ability to define the elements of the Mueller matrix as 2D images.

By using the polarimetric microscope, I believe that the complete Mueller matrix of a sample can be determined. However, there are not sufficient measurements taken to provide the full set of Mueller matrix elements in the current experiment, where only linear polarised light was generated during the measurements. The polariser was oriented at five different angles (θ=0°, 20°, 40°, 60°, 80°), and at each angle, the linear polarised light passing through the air was measured. After that, the sample was inserted, and the linear polarised light was measured for the same five angles of polarisation. Although the determination of a Mueller matrix requires measurements of four different polarised states as a minimum, here, five different measurements were taken to offer overdetermination thus increasing the accuracy of the results. Then the Mueller matrix of the sample was extracted by inversion calculation.

$$\begin{bmatrix} I \\ Q \\ U \\ V \end{bmatrix}_\theta = M \begin{bmatrix} I_{air} \\ Q_{air} \\ U_{air} \\ V_{air} \end{bmatrix}_\theta \tag{7-1}$$

$$I_\theta = m_{00}\, I_{air(\theta)} + m_{01}\, Q_{air(\theta)} + m_{02}\, U_{air(\theta)} + m_{03}\, V_{air(\theta)} \tag{7-2}$$

$$Q_\theta = m_{10}\, I_{air(\theta)} + m_{11}\, Q_{air(\theta)} + m_{22}\, U_{air(\theta)} + m_{33}\, V_{air(\theta)} \tag{7-3}$$

$$U_\theta = m_{20}\, I_{air(\theta)} + m_{21}\, Q_{air(\theta)} + m_{22}\, U_{air(\theta)} + m_{23}\, V_{air(\theta)} \tag{7-4}$$

$$V_\theta = m_{30}\, I_{air(\theta)} + m_{31}\, Q_{air(\theta)} + m_{32}\, U_{air(\theta)} + m_{33}\, V_{air(\theta)} \tag{7-5}$$

where $[I\ Q\ U\ V]^T$ is the Stokes vector of the light entering through the sample, while $[I_{air}\ Q_{air}\ U_{air}\ V_{air}]^T$ is the Stokes vector of light travelling through the air, and θ=0°, 20°, 40°, 60°, 80° are the polariser angles. Each equation has four unknown

Mueller elements and could be separated into five different equations for the five different polarisation states measurements. The resulting equations could be organised in matrix formula as the following:

$$
\begin{pmatrix}
I_0 & I_{20} & I_{40} & I_{60} & I_{80} \\
Q_0 & Q_{20} & Q_{40} & Q_{60} & Q_{80} \\
U_0 & U_{20} & U_{40} & U_{60} & U_{80} \\
V_0 & V_{20} & V_{40} & V_{60} & V_{80}
\end{pmatrix} =
$$

$$
\begin{pmatrix}
m_{00} & m_{01} & m_{02} & m_{03} \\
m_{10} & m_{11} & m_{12} & m_{13} \\
m_{20} & m_{21} & m_{22} & m_{23} \\
m_{30} & m_{31} & m_{32} & m_{33}
\end{pmatrix}
\begin{pmatrix}
I_{air0} & I_{air20} & I_{air40} & I_{air60} & I_{air80} \\
Q_{air0} & Q_{air20} & Q_{air40} & Q_{air60} & Q_{air80} \\
U_{air0} & U_{air20} & U_{air40} & U_{air60} & U_{air80} \\
V_{air0} & V_{air20} & V_{air40} & V_{air60} & V_{air80}
\end{pmatrix}
\tag{7-6}
$$

Figure 7-12 shows nine elements of the Mueller matrix measured experimentally.
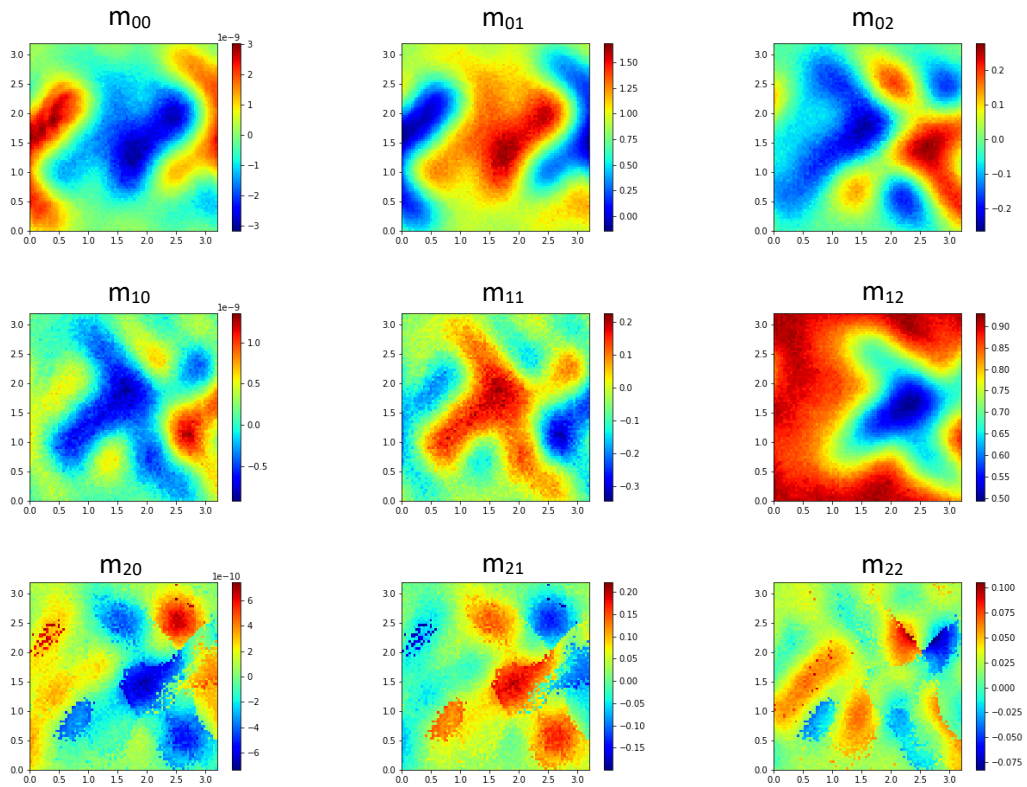
Figure 7-12: Imaging nine elements of Mueller matrix in 2D for chiral gammadion shape, the dimension of the measurement is 3μm x 3μm. (the code is in Appendix A-6).

The experimental data collected in this section was thus insufficient to gather beyond nine elements because circularly polarised light was not used. To achieve measurement of the complete elements of the Mueller matrix (16 elements), the

experiment could be extended to add measurements using the QWP to generate circularly polarised.

7.6   Comparing Two Sides of a Sample

As Zhang et al. (2005, 2006) demonstrated when illuminating both sides of a planar pattern, the handedness of the polarisation rotation was opposite to that for the other side. In this section, the results of the measurements of both sides of a single gammadion sample are presented. Table 7-6 shows the experimental measurements of transmission light for linearly polarised beams incident on both sides of metamaterial structure in gammadion shape. The measurements were acquired by using 660 nm LED light and a 40x objective lens with 1.6x immersion oil.

Thus, chiral materials should demonstrate different signs for handedness for both sides of a sample, based on the result shown in previous research (Zhang *et al.*,2006). However, the current experimental results do not show any clear difference between the opposite sides, perhaps because the accuracy required to demonstrate such measurements is beyond the current technical capabilities of the polarimetric microscope. In fact, the obtained results should not be considered automatically in contradiction with previous research outcomes due to this; they should instead open the door to further work in this area.

Table 7-6: The measurement of both sides of a chiral sample: a) normalised Stokes parameters (**Q/I, U/I, V/I**) and normalised depolarisation (ndP); b) Ellipticity angle; c) Azimuth angle.

	Side 1	Side 2
a) Q/I, U/I, V/I and ndP		
b) ellipticity angle		
c) Azimuth angle		
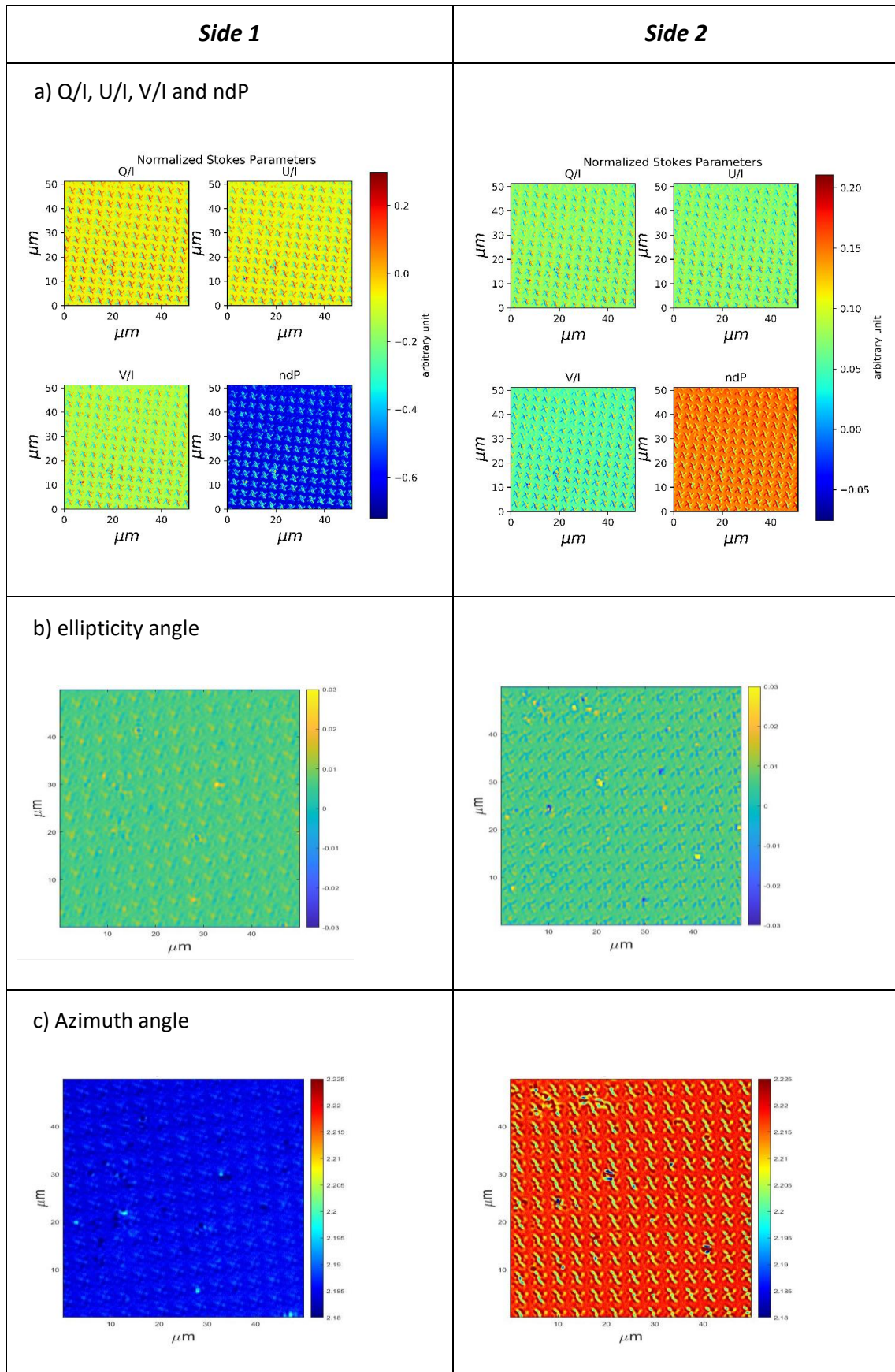
7.7 Fourier transformation

The Fourier transform (FT) is an important image processing tool based on applying a mathematical formula to transfer the image from its natural space (the space domain in this case) into the Fourier space (the frequency domain). FT decomposes an image into its sinusoidal components, with each point representing a specific frequency. Thus, a particular frequency of an image could be observed. FT has several applications in imaging processing, such as image analysis, image filtering, image reconstruction, and image compression. The mathematical expression for FT is generally written as the following (Solomon and Breckon, 2011):

$$F(k,l) = \sum_{i=0}^{N-1} \sum_{j=0}^{N-1} f(i,j) e^{-i2\pi\left(\frac{ki}{N}+\frac{lj}{N}\right)} \tag{7-7}$$

where the image size is NxN; f(i,j) is the input image in the spatial space; and F(k,l) is the image in the Fourier space. Each point of the function F(k,l) is a result of double summation over the multiplication of each pixel in the function f(i,j) by the corresponding exponential function. As is clear from the mathematical expression, FT output thus involves complex numbers, and the DC component appears at the centre of the FT representation for F(0,0) (McAndrew, 2004).

The response of Stokes parameters images to FT was examined in order to develop a further understanding of the nature of the periodic patterns. By using MATLAB, FT was thus applied to one of the current experimental results, the outcome of FT shown in Figure 7-13.
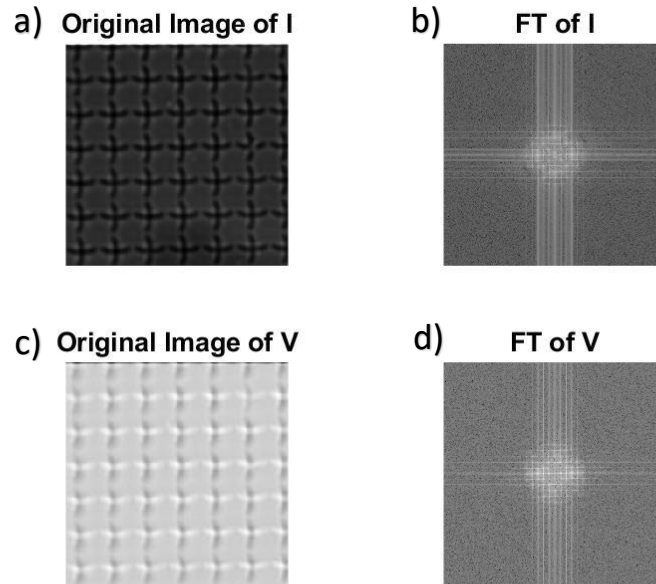
*Figure 7-13: FT of Stokes parameters **I** and **V**. a) I component; b) FT of **I**; c) **V** component; and d) FT of **V**.*

The Fourier transformation of the **I** and **V** images showed two dominating directions, the vertical and horizontal, passing through the centre. These dominating because of the regularity of the patterns in the original images.

7.8   Investigation of nanoparticles

To understand the nature of nanoparticle responses, several experiments were undertaken to measure the normalised Stokes parameters for gold nanoparticles (GNP), gold nanostars (GNS), and copper nanoparticles (CuNP). Two different sizes of GNP, 50 nm and 15nm, were thus investigated. Furthermore, the copper nanoparticles were synthesised in solution with two different pH values, PH=10 and 10.5. The resultant samples were prepared by either putting the particles on a glass slide and sealing this immediately with a top slide or allowing the particles to dry on the glass before adding the top slide, where the later versions were labelled as' 'Dried'. These samples were provided by Dr Zeljka Krpetic (University of Salford).

The normalised Stokes parameters (**Q/I, U/I,** and **V/I**) and the normalised depolarisation were measured for various nanoparticles using a polarimetric microscope with 455nm LED and the result is shown in the following figures: Figure 7-14 shows Gold nanoparticles, Figure 7-15 shown Gold nanostars, and Figure 7-16 shown Copper nanoparticles.
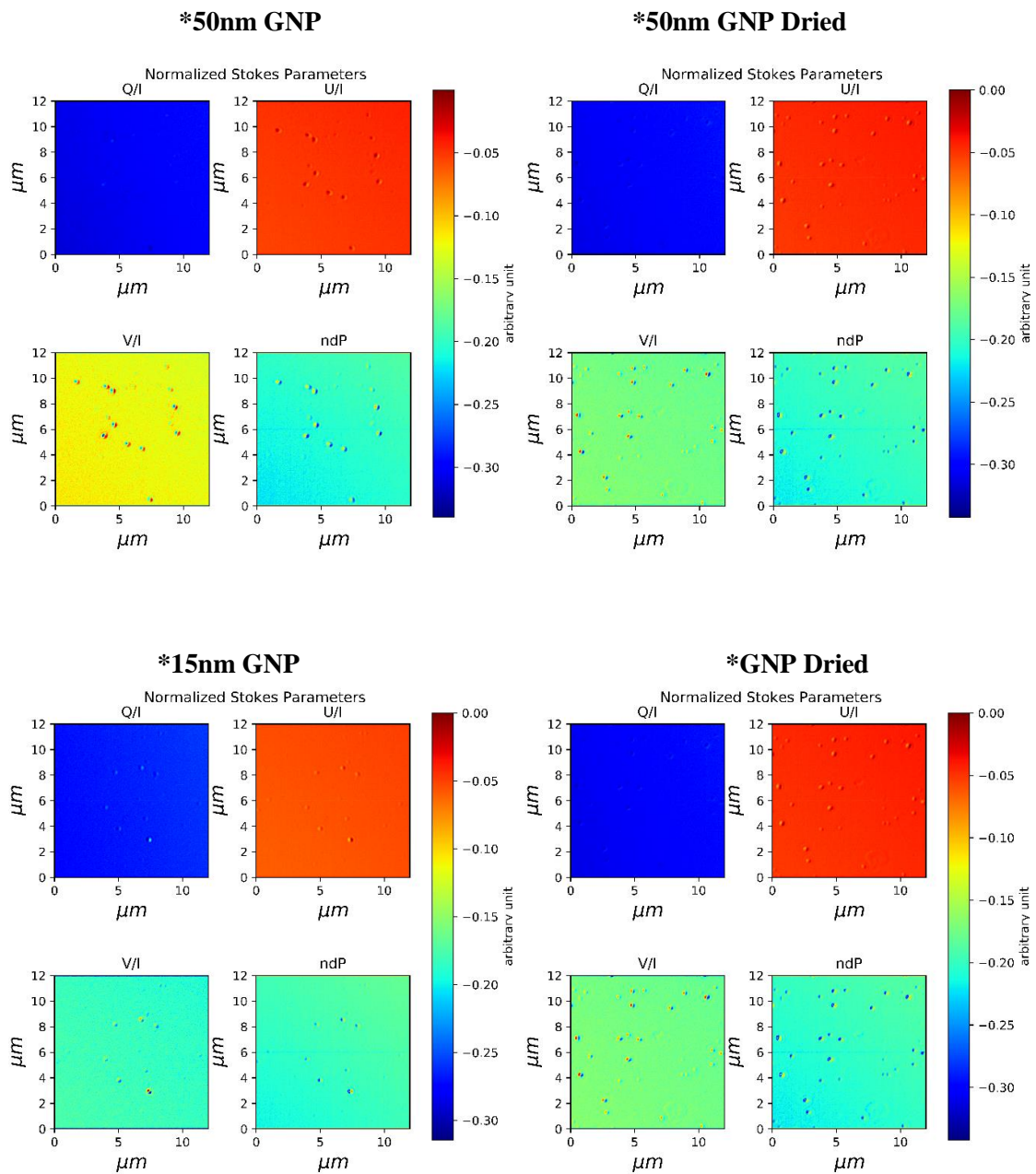
*Figure 7-14: normalised Stokes parameters (**Q/I, U/I, V/I**) and normalised depolarisation (ndP) of gold nanoparticles by using LED 455nm, 100x objective lens with 1.6x immersion oil, 320x320 pixels*
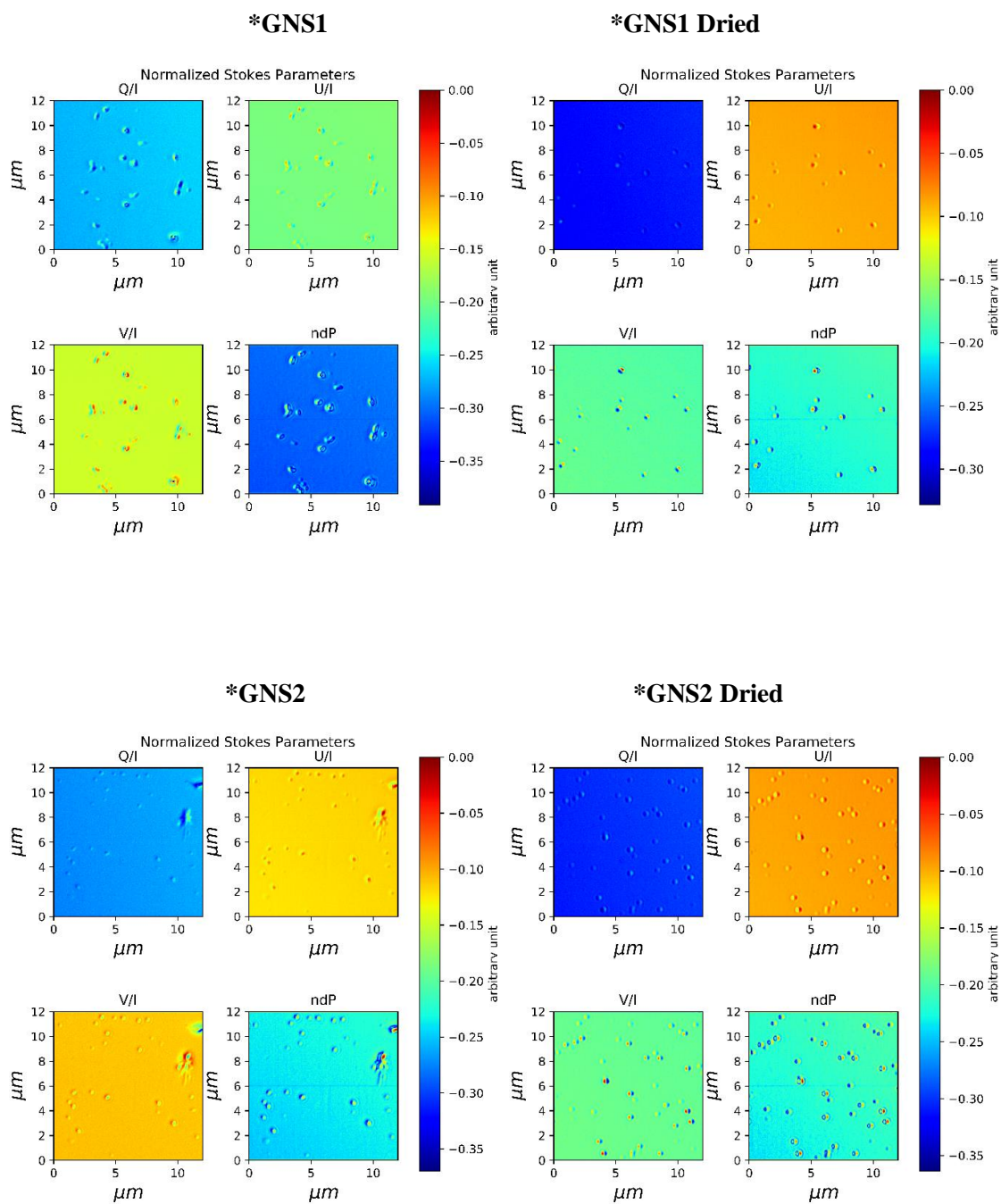
*Figure 7-15: normalised Stokes parameters (**Q/I, U/I, V/I**) and normalised depolarisation (ndP); of gold nanostars by using LED 455nm, 100x objective lens with 1.6x immersion oil, 320x320 pixels*

*CuNP PH10 Dried   ***CuNP PH10.5 Dried**

*CuNP PH10   *** CuNP PH10.5**
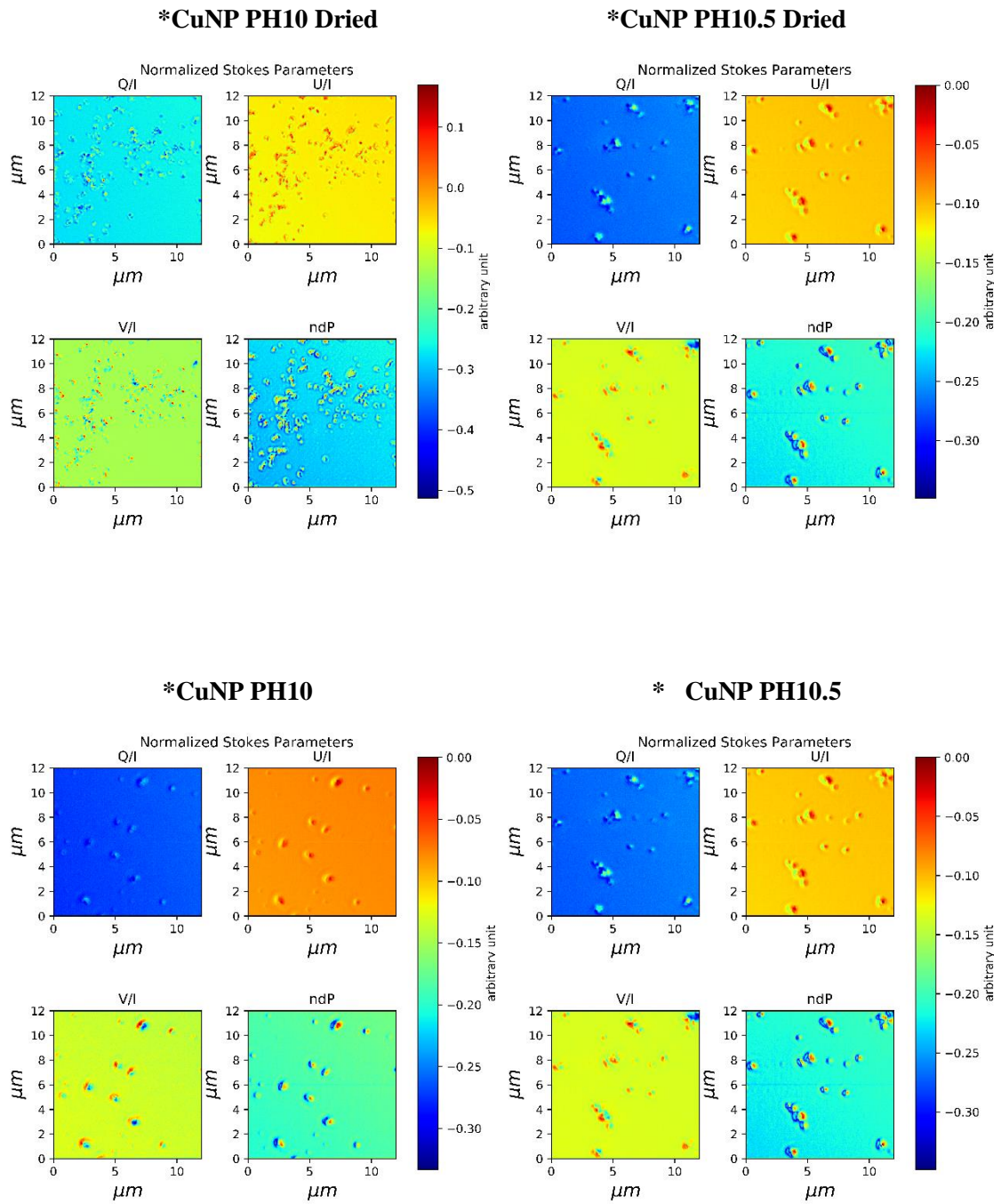
*Figure 7-16: normalised Stokes parameters (**Q/I, U/I, V/I**) and normalised depolarisation (ndP); of copper nanoparticles by using LED 455nm, 100x objective lens with 1.6x immersion oil, 320x320 pixels*

Conclusion

In this thesis, the optical properties of planar chiral materials were studied both theoretically and experimentally. General theoretical concepts supporting this work, including chirality and polarised light, were thus initially discussed. Furthermore, the background of the experimental work was briefly reviewed.

Simulations were performed to investigate four different models, as described in chapter 6. Despite the acknowledged presence of certain limitations, these models offer significant potential for the development of an application for analysing chiral structures. However, there is no doubt that these models require improvement to make them more convenient for the measurement of the chirality properties of any shape. In fact, currently, they cannot be used in making comparisons of different chiral patterns due to their area dependence.

The dual photoelastic modulators polarimetry system was described as used in this work, that is, were operating in transmission mode. The polarimetry system was then used to modify an optical microscope to offer additional information about the optical properties of a mesoscopic structure, as described in section 5.6. Thus, the microscope was equipped with two polarisers and two photoelastic modulators, with a digital camera used as a detector. The two photoelastic modulators were operated at different frequencies, offering the potential to simultaneously obtain the four elements required for the Stokes parameters. The combined use of the microscope and the dual photoelastic modulators polarimetry provided valuable insights into planar chiral metamaterial structures, allowing certain structural insights down to the molecular level.

We point out that the minimisation of the errors was ensured by calibrating the system prior to doing measurements of the samples. The calibration routine was performed as described to determine the characteristics of the polarimetry system based on generating eight constants related to the set of angles associated with optical elements. A detailed inspection of these revealed that the calibration process is essential to avoid random and systematic errors that might otherwise result from imperfections in the optical components and misalignments in the experimental setup.

The dual photoelastic configuration should be implementable in a polarimetric microscope, which is important based on the latter's use as an extremely sensitive tool for understanding the properties of metamaterial structures. This work shows that a great deal of valuable information may be extracted from these images, with the system being used to detect metamaterial samples in gammadion shapes, as well as some nanoparticles, as shown in chapter 7. Several examples are offered to illustrate the polarimetric microscope's adequacy for multiple practical applications, such as the measurements of the Stokes parameters, ellipticity angles, azimuth angles, and Mueller Matrices.

The results support the idea that the proposed polarimetric microscope permits effective measurement of the Stokes vectors. The results also confirm that the polarimetric microscope is suitable for studying the effects of chiral structures on linear and circular polarised light. By analysing the Stokes images obtained from the signal, we are able to quantify the polarisation state of arbitrary polarised light, namely, the Ip, Idp, DOP, DOLP, and DOCP, as defined in section 2.3.

From a more general perspective, this characterisation study has demonstrated that the polarimetric microscope can measure the full Mueller matrix of a sample. Although the experimental results offered in this work have shown the result of nine elements of the Mueller matrix of a planar metamaterial in transmission mode, as a QWP was not used in this case to generate a circular signal; however, all the 16 elements could be gained using the same approach by adding some circularly polarised light.

Interestingly, imaging in reciprocal space may constitute an attractive alternative to more conventional approaches, leading to a better understanding of composition and offering a new way to detect anomalies in specimens. This may be relevant in cases such as diseases in biological samples that have not been previously well understood. The resulting detailed mapping of the Stokes parameters may also offer a new way to analyse the polarisation characteristics of the diffraction based on the application of Fourier optics, which is an area worthy of further study in future.

To evaluate the measurement performance of the proposed polarimetry system, evidence of its validity is first required. The system should be used to obtain suitable

measurements of materials with known Mueller matrices in order to provide evidence of its reliability in terms of making valid Mueller matrix measurements.

Finally, this work has demonstrated that the microscope is a versatile instrument that can be used for a wide range of applications, wherever imaging the optical properties of a sample is essential. The method still has room for improvement; however, both reduce experimental errors and improve the interpretation of results. Work is in progress to further increase the amount of information derived from dual photoelastic modulators. The polarimetric microscope could thus be optimised to involve different vision apart from the investigated transmission mode, where transmission measurements depend on the thickness of the sample, which is not the case in reflection measurements. Another interesting perspective for future work would be to extend the experiments to include light sources providing a wider range of wavelength.

Future work

Obviously, the use of the polarimetric microscope is a valuable technique for a wide range of fields. However, the method still has opportunities for further enhancements where new approaches can be induced. For example, the polarimetric microscope could thus be extended to work in reflection mode in addition to transmission mode. Nevertheless, the light source would be optimised to employ a broad band light source to get optical properties of samples as a function of the light wavelength. In addition, designing and running experiments to study the sample's behaviour under applying magnetic field could investigate addition phenomena such as Faraday rotation.

Unfortunately, the experimental images were obtained by using a camera with a fan, and that introduced a vibration which produced noise in the outcome images. Future work could be carried out using a water-cooled camera to avoid vibrational interference.

Using LabView, the microscope could be automated to directly calculate some optical properties such as the Stokes parameters, ellipticity angles, azimuth angles, and Mueller Matrices without the need for additional python programming. This step will effectively save more time. Moreover, the graphs could be improved with more attributes and details.

The way used to calculate Mueller matrix elements could also be changed. In addition to using linear polarised light, circular polarised light could be generated to calculate all the 16 elements of the Mueller matrix. Moreover, evaluation of Mueller matrix measurements' validity could be done by obtaining measurements of materials with known Mueller matrices.

Concerning the calibration results provided in section 7.2, the results of different light wavelength have not been compared. Such comparison could be made for different further calibrations, which could improve the calibration reliability in future work.

Due to the unexpected curtailment of the research phase of this work by national lockdowns caused by the ongoing Covid-19 pandemic, the work in the Fourier transformation area is highly preliminary at this stage of writing the thesis. However,

the initial results suggest that this is a highly promising area, as it may lead to the establishment of convenient and valuable means of evaluating the polarisation characteristics in the Fraunhofer diffraction of light. This relates favourably to prior studies in the literature where the focus has been on the direct measurements of polarisation characteristics of the diffracted light beams. So, further research in this direction may also offer a new way to analyse the polarisation characteristics of the diffraction based on the application of Fourier optics, which is an area worthy of further study in future.

Regarding the quantification of chirality, there are also many ideas that could be investigated to try to obtain a quantitative expression for chirality. It could be interesting to consider the seek on how to get a mathematical expression that just depends on chirality using triangle angles instead of sides to be area independent.

In general, the preliminary results of these experiments do not seem to be satisfactory, and further study is still required in order to understand the behaviour of chiral samples and improve the polarimetric microscope.

References

Aas, L. M. S. (2009). 'Mueller matrix ellipsometric imaging. *Dept. Phys., NTNU, Oslo, Norway*.

Arteaga, O. (2010). *Mueller matrix polarimetry of anisotropic chiral media* (Doctoral dissertation, Universitat de Barcelona).

Bass, M. (2010). *Handbook of Optics: Volume I-Geometrical and Physical Optics, Polarized Light, Components and Instruments*. McGraw-Hill Education.

Bass, M. (1995). Handbook of Optics: Devices, Measurements, and Properties, Vol. 2.

Born, M., and Wolf, E. (1999). *Principle of the Optics Electromagnetic Theory of propagation interference and diffraction of light.* 7th Edition, Cambridge University Press.

Boruhovich, S. P. (2006). Chirality Measure for 2D and 3D Meta-Materials. *International Conference on Mathematical Methods in Electromagnetic Theory* on (pp. 418-420). IEEE

Brandt, J. R., Salerno, F., and Fuchter, M. J. (2017). The added value of small-molecule chirality in technological applications. *Nature Reviews Chemistry*, *1*(6), 0045.

Brooks, W. H., Guida, W. C., and Daniel, K. G. (2011). The significance of chirality in drug design and development. *Current topics in medicinal chemistry*, *11*(7), 760-770.

Common wikimedea Retrieved from:
https://commons.wikimedia.org/wiki/File:Poincar%C3%A9_sphere.svg#file

Cormen, T. H., Leiserson, C. E., Rivest, R. L., and Stein, C. (2009). *Introduction to algorithms*. MIT press.

emedicalprep.com Retrieved from:

https://www.emedicalprep.com/study-material/physics/wave-optics/polarization/

Emile, J., Emile, O., Ghoufi, A., Moréac, A., Casanova, F., Ding, M., and Houizot, P. (2013*).* Giant optical activity of sugar in thin soap films. *Elsevier Inc.*

Fedotov, V. A., Mladyonov, P. L., Prosvirnin, S. L., Rogacheva, A. V., Chen, Y., and Zheludev, N. I. (2006). Asymmetric Propagation of Electromagnetic Waves through a Planar Chiral Structure. *Physical review letters, 97*(16), 167401.

Fowler, P. W. (2005). "Quantification of chirality: Attempting the impossible. "Symmetry: *Culture and Science* 16.4, 321-334.

Fowler, P. W., and Rassat, A. (2006). A classification scheme for chiral tetrahedra. *Comptes Rendus Chimie*, *9*(9), 1203-1208.

Garcia-Caurel, E., De Martino, A., Gaston, J. P., and Yan, L. (2013). Application of spectroscopic ellipsometry and Mueller ellipsometry to optical characterization. *Applied spectroscopy*,*67*(1), 1-21.

Goodman, J. W. (2005). *Introduction to Fourier optics*. Roberts and Company Publishers.

Guan, W., Cook, P. J., Jones, G. A., and Shen, T. H. (2010).Experimental determination of the Stokes parameters using a dual photoelastic modulator system. *Applied Optics*, *49*(14), 2644-2652

Guan, W., Jones, G. A., Liu, Y., and Shen, T. H. (2008). The measurement of the Stokes parameters: a generalized methodology using a dual photoelastic modulator system. *Journal of Applied Physics, 103*(4), 043104.

Hauge, P. S., Muller, R. H., and Smith, C. G. (1980). Conventions and formulas for using the Mueller-Stokes calculus in ellipsometry. *Surface science*, *96*(1-3), 81-107.

Hecht, E. (2002). *Optics.* 4th Edition, Pearson Education Limited.

Huang, Y., Yao, Z., Hu, F., Liu, C., Yu, L., Jin, Y., and Xu, X. (2017). Tunable circular polarization conversion and asymmetric transmission of planar chiral graphene-metamaterial in terahertz region. *Carbon, 119*, 305-313.

Kim, T. T., Oh, S. S., Park, H. S., Zhao, R., Kim, S. H., Choi, W., Min, B. and Hess, O. (2014). Optical activity enhanced by strong inter-molecular coupling in planar chiral metamaterials. *Scientific reports, 4*, 5864.

Kwon, D. H., Werner, P. L., and Werner, D. H. (2008). Optical planar chiral metamaterial designs for strong circular dichroism and polarization rotation. *Optics express*, *16*(16), 11802-11807.

Li, Z., Zhao, R., Koschny, T., Kafesaki, M., Alici, K. B., Colak, E., Caglayan,H.,Ozbay E., and Soukoulis, C. M. (2010). Chiral metamaterials with negative refractive index based on four "U" split ring resonators. *Applied Physics Letters*, *97*(8), 081901.

Li, Z., Alici, K. B., Colak, E., and Ozbay, E. (2011). Complementary chiral metamaterials with giant optical activity and negative refractive index. *Applied Physics Letters*, *98*(16), 161907.

Li, Z., Mutlu, M., and Ozbay, E. (2013). Chiral metamaterials: from optical activity and negative refractive index to asymmetric transmission. *Journal of Optics*, *15*(2), 023001.

Lin, J. F., and Lee, M. Z. (2012). Concurrent measurement of linear birefringence and dichroism in ferrofluids using rotating-wave-plate Stokes polarimeter. *Optics Communications*, *285*(7), 1669-1674.

Liu, Y. (2005). *A study of magnetic ultrathin films on GaAs and optically excited spin injection* (Doctoral dissertation, University of Salford).

Liu, Y., Jones, G. A., Peng, Y., and Shen, T. H. (2006). Generalized theory and application of Stokes parameter measurements made with a single photoelastic modulator.*Journal of applied physics*, *100*(6), 063537.

Ma, X., Pu, M., Li, X., Guo, Y., Gao, P., and Luo, X. (2017). Meta-chirality: Fundamentals, construction and applications.*Nanomaterials*, *7*(5), 116.

MacLennan, B. J. (2008). Computation and nanotechnology.

McAndrew, A. (2004). An introduction to digital image processing with matlab notes for scm2511 image processing. *School of Computer Science and Mathematics, Victoria University of Technology*, *264*(1), 1-264.

McCall, M. W., Hodgkinson, I. J., and Wu, Q. (2014). *Birefringent thin films and polarizing elements*. World Scientific.

McConathy, J., and Owens, M. J. (2003). Stereochemistry in drug action. *Primary care companion to the Journal of clinical psychiatry*, *5*(2), 70.

Nava, J., and Kreinovich, V. (2016). *Algorithmic Aspects of Analysis, Prediction, and Control in Science and Engineering*. Springer-Verlag Berlin An.

Osipov, M. A., Pickup, B. T., Fehervari, M., and Dunmur, D. A. (1998). Chirality measure and chiral order parameter for a two-dimensional system.*Molecular Physics*, *94*(2), 283-287.

Papakostas, A., Potts, A., Bagnall, D. M., Prosvirnin, S. L., Coles, H. J., and Zheludev, N. I. (2003). Optical manifestations of planar chirality. *Physical Review Letters*, *90*(10), 107404.

Peatross, J., and Ware, M. (2011). *Physics of light and optics* (pp. 101-119). Brigham Young University, Department of Physics.

Petitjean, M. (2003). Chirality and symmetry measures: A transdisciplinary review. Entropy, 5(3), 271-312.

Plum, E. (2010). *Chirality and metamaterials* (Doctoral dissertation, University of Southampton).

Potts, A., Papakostas, A., Zheludev, N. I., Coles, H. J., Greef, R., and Bagnall, D. M. (2002). Optical properties of planar chiral meta-materials. In *MRS Proceedings* (Vol. 722, pp. K10-3). Cambridge University Press

Potts, A., Bagnall, D. M., and Zheludev, N. I. (2003). A new model of geometric chirality for two-dimensional continuous media and planar meta-materials. *Journal of Optics A: Pure and Applied Optics*, *6*(2), 193.

Rassat, A., and Fowler, P. W. (2003). Any scalene triangle is the most chiral triangle. *Helvetica chimica acta*, *86*(5), 1728-1740.

Schmidt, D., Schubert, E., and Schubert, M. (2013). Generalized ellipsometry characterization of sculptured thin films made by glancing angle deposition. In *ellipsometry at the Nanoscale* (pp. 341-410). Springer, Berlin, Heidelberg.

Schwanecke, A. S. (2009). *Novel phenomena in planar and layered, photonic and microwave metamaterials* (Doctoral dissertation, University of Southampton).

Shamiryan, D., and Likhachev, D. V. (2012). Spectroscopic ellipsometry of ion-implantation-induced damage. *Ion Implantation*, 89-104.

Sharma, K. K. (2006). *Optics: principles and applications*. Elsevier.

Solomon, C., and Breckon, T. (2011). *Fundamentals of Digital Image Processing: A practical approach with examples in Matlab*. John Wiley and Sons.

Testa, B. (2013). Organic Stereochemistry. Part 3. *Helvetica Chimica Acta*, *96*(3), 351-374.

Trippe, S. (2014). Polarization and polarimetry: A review. *arXiv preprint arXiv:1401.1911*.

Tutor Vista. Retrieved from: http://www.tutorvista.com/content/physics/physics-iv/optics/polarization.php

Valev, V. K., Zheng, X., Biris, C. G., Silhanek, A. V., Volskiy, V., De Clercq, B., ... and Moshchalkov, V. V. (2011). The origin of second harmonic generation hotspots in chiral optical metamaterials. *Optical Materials Express, 1*(1), 36-45.

Wang, B., Zhou, J., Koschny, T., Kafesaki, M., and Soukoulis, C. M. (2009). Chiral metamaterials: simulations and experiments. *Journal of Optics A: Pure and Applied Optics*,*11*(11), 114003.

Wang, Z., Cheng, F., Winsor, T., and Liu, Y. (2016). Optical chiral metamaterials: a review of the fundamentals, fabrication methods and applications. *Nanotechnology*, *27*(41), 412001.

Wen, D., Yue, F., Kumar, S., Ma, Y., Chen, M., Ren, X., and Chen, X. (2015). Metasurface for characterization of the polarization state of light. *Optics express*, *23*(8), 10272-10281.

Wiersma, D.(2013) Retrieved from: https://fineartamerica.com/featured/birefringence-in-a-calcite-crystal-dirk-wiersma.html

Ye, W., Yuan, X., Guo, C., Zhang, J., Yang, B., and Zhang, S. (2017). Large chiroptical effects in planar chiral metamaterials. Physical *Review Applied, 7*(5), 054003.

Zhang, W., Potts, A., Papakostas, A., and Bagnall, D. M. (2005). Intensity modulation and polarization rotation of visible light by dielectric planar chiral metamaterials. *Applied Physics Letters*, *86*(23), 231905.

Zhang, W., Potts, A., and Bagnall, D. M. (2006). Giant optical activity in dielectric planar metamaterials with two-dimensional chirality. *Journal of Optics A: Pure and Applied Optics*, *8*(10), 878.

Zhang, W. (2006). OPTICAL ACTIVITY AND APPLICATIONS OF PLANAR CHIRAL METAMATERIALS. University of Southampton, Faculty of Engineering, Science and Mathematics, PhD Thesis.

Zhao, J., & Cheng, Y. (2018). Ultrathin dual-band polarization angle independent 90° polarization rotator with giant optical activity based on planar chiral metamaterial. *Applied Physics B*, *124*(9), 1-7.

Zhou, L., Wang, Y., Zhou, J., Ding, J., Lu, M., & Sang, T. (2020). Tunable asymmetric transmission across stretchable chiral metamaterial. *Applied Optics*, *59*(23), 6868-6872.

Appendix A

Matlab Codes

A-1) Matlab Code to plot spiral (Figure 2.2).

```matlab
%%% program to plot spiral patterns %%%
%%% by Huda Alzahrani 29/3/2018 %%%
=============================================

 t = linspace(0,10*pi,2000);

x1=(t.^2).*sin(t);
 y1=-(t.^2).*cos(t);
z = zeros(size(t));


col = t;         % This is the color, vary with x in this case.
surface([x1;x1],[y1;y1],[z;z],[col;col],'facecol','no','edgecol','inte
rp','linewidth',5);
ax=gca;
ax.XTick=[];
ax.YTick=[];
hold on
quiver3(x1(end-1), y1(end-1), z(end-1), x1(end)-x1(end-1), y1(end)-
y1(end-1), z(end)-z(end-1),10,'LineWidth',5,'MaxHeadSize',50);
title('\fontsize{30} b) anti-clockwise spiral')
```

A-2) Matlab Codes to calculate Chirality index of a triangle (Figure 6.3).

```matlab
%%% program to calculate the relationship between chirality and the
angles of a triangle with consideration of the mass m1=m2=m3=M/3 in
each triangle and a2=0.5*a1 %%%
%%% by Huda Alzahrani 23/1/2018 %%%
=============================================


a1=1;
th3=0:10:360;
for n=1:length(th3);
a2=0.5*a1;

X(:,:,n)=[0,a1,a2*cosd(th3(n))];%x1,x2,x3 of the triangle ABC
Y(:,:,n)=[0,0,a2*sind(th3(n))];%y1,y2,y3 of the triangle ABC
  points(:,:,n)=[X(:,:,n);Y(:,:,n)];


Area(n) = polyarea(X(:,:,n),Y(:,:,n));%Area(of the angle ABC)
```

```matlab
        mass=1/length(points(1,:,1));
ka(n)=0;
kb(n)=0;
kc(n)=0;
kd(n)=0;
 for m1=1:length(points(1,:,n));
  for m2=1:length(points(1,:,n));
    for  m3=1:length(points(1,:,n));

         %          %clockwise condition
        x2x1=( points(1,m2,n)-
points(1,m1,n))*(points(2,m2,n)+points(2,m1,n));
        x3x2= (points(1,m3,n)-
points(1,m2,n))*(points(2,m3,n)+points(2,m2,n));
        x1x3=( points(1,m1,n)-
points(1,m3,n))*(points(2,m1,n)+points(2,m3,n));
        order=x2x1+x3x2+x1x3;
         if m1==m2|m1==m3|m2==m3|order<=0
        ka(n)=ka(n);
        kb(n)=kb(n);
        kc(n)=kc(n);
        kd(n)=kd(n);
         else

ka(n)=ka(n)+(mass^3)*chirala(points(:,m1,n),points(:,m2,n),points(:,m3
,n));
kb(n)=kb(n)+(mass^3)*chiralb(points(:,m1,n),points(:,m2,n),points(:,m3
,n));
kc(n)=kc(n)+(mass^3)*chiralc(points(:,m1,n),points(:,m2,n),points(:,m3
,n));
kd(n)=kd(n)+(mass^3)*chirald(points(:,m1,n),points(:,m2,n),points(:,m3
,n));



    end
   end
  end
 end
 kd1(n)=10*kd(n);
ka1(n)=ka(n)/5;
end


figure
plot(th3,ka1,'m-.x',th3,kb,'-s',th3,kc,'r--
o',th3,kd1,'b:d','MarkerSize',10,'LineWidth',3)
legend('Osipov model','1st model','2nd model','3rd model')
title('Potts models')
grid on

xlabel('\theta_3 \circ')
ylabel('K')

 set(gca,'xlim',[0
360],'XTick',[0:30:360],'FontSize',26,'LineWidth',2)
```

A-3) Matlab Codes to calculate Chirality index of a triangle (Figure 6.4).

```matlab
%%% program to calculate the relationship between chirality and the
angle of a triangle with consideration of the mass m1=m2=m3=M/3 in
each triangle. and a2=0.7*a1%%%
%%% by Huda Alzahrani 2/2/2018 %%%
=============================================

a1=1;
th3=0:10:360;
for n=1:length(th3);
a2=0.7*a1;

X(:,:,n)=[0,a1,a2*cosd(th3(n))];       %x1,x2,x3 of the triangle ABC
Y(:,:,n)=[0,0,a2*sind(th3(n))];        %y1,y2,y3 of the triangle ABC
  points(:,:,n)=[X(:,:,n);Y(:,:,n)];


Area(n) = polyarea(X(:,:,n),Y(:,:,n));%Area(of the riangle ABC)



      mass=1/length(points(1,:,1));
ka(n)=0;
kb(n)=0;
kc(n)=0;
kd(n)=0;
 for m1=1:length(points(1,:,n));
  for m2=1:length(points(1,:,n));
    for  m3=1:length(points(1,:,n));

       %          %clockwise condition
       x2x1=( points(1,m2,n)-
points(1,m1,n))*(points(2,m2,n)+points(2,m1,n));
       x3x2= (points(1,m3,n)-
points(1,m2,n))*(points(2,m3,n)+points(2,m2,n));
       x1x3=( points(1,m1,n)-
points(1,m3,n))*(points(2,m1,n)+points(2,m3,n));
       order=x2x1+x3x2+x1x3;
        if m1==m2|m1==m3|m2==m3|order<=0
       ka(n)=ka(n);
       kb(n)=kb(n);
       kc(n)=kc(n);
       kd(n)=kd(n);
        else

ka(n)=ka(n)+(mass^3)*chirala(points(:,m1,n),points(:,m2,n),points(:,m3
,n));
kb(n)=kb(n)+(mass^3)*chiralb(points(:,m1,n),points(:,m2,n),points(:,m3
,n));
kc(n)=kc(n)+(mass^3)*chiralc(points(:,m1,n),points(:,m2,n),points(:,m3
,n));
kd(n)=kd(n)+(mass^3)*chirald(points(:,m1,n),points(:,m2,n),points(:,m3
,n));



    end
   end
```

```
   end
  end
 kd1(n)=10*kd(n);
ka1(n)=ka(n)/5;
end


figure
plot(th3,ka1,'m-.x',th3,kb,'-s',th3,kc,'r--
o',th3,kd1,'b:d','MarkerSize',10,'LineWidth',3)
legend('Osipov model','1st model','2nd model','3rd model')
title('Potts models')
grid on

xlabel('\theta_3 \circ')
ylabel('K')

 set(gca,'xlim',[0
360],'XTick',[0:30:360],'FontSize',26,'LineWidth',2)
```

A-4) Matlab Codes to calculate Chirality index of similar triangles (Figure 6.7).

```
 %%% program to calculate the relationship between chirality and the
area of a triangle with consideration of the mass m1=m2=m3=M/3 in each
triangle.%%%
%%% by Huda Alzahrani 11/4/2018 %%%
```

```
 p1=[0,0];        % the first point(x1,y1) of the triangle ABC
 p2=[1,0];        % the second point(x2,y2) of the triangle ABC
 p3=[1,0.7];         % the third point(x3,y3) of the triangle ABC
X=[0,1,1];%x1,x2,x3 of the triangle ABC
 Y=[0,0,0.7];%y1,y2,y3 of the triangle ABC
a1=1:1:10;
 th3=45;
 d=0.1;
 for n=1:length(a1);
 a2(n)=0.7*a1(n);
% a triangle with pixliting the sides to many pointts

 x1(:,:,n)=linspace(0,a1(n),20);
   y1(:,:,n)=zeros(1,20);
   x2(:,:,n)=linspace(0,a2(n)*cosd(th3),20);
     y2(:,:,n)=linspace(0,a2(n)*sind(th3),20);
 x3(:,:,n)=linspace(a2(n)*cosd(th3),a1(n),20);
 y3(:,:,n)=linspace(a2(n)*sind(th3),0,20);%
 points(:,:,n)=[x1(:,:,n),x2(:,:,n),x3(:,:,n);y1(:,:,n),y2(:,:,n),y3(:
,:,n)];


     mass=1/length(points(1,:,1));
ka(n)=0;
kb(n)=0;
kc(n)=0;
```

```matlab
kd(n)=0;
 for m1=1:length(points(1,:,n));
  for m2=1:length(points(1,:,n));
    for  m3=1:length(points(1,:,n));

         %           %clockwise condition
        x2x1=( points(1,m2,n)-
points(1,m1,n))*(points(2,m2,n)+points(2,m1,n));
        x3x2= (points(1,m3,n)-
points(1,m2,n))*(points(2,m3,n)+points(2,m2,n));
        x1x3=( points(1,m1,n)-
points(1,m3,n))*(points(2,m1,n)+points(2,m3,n));
        order=x2x1+x3x2+x1x3;
         if m1==m2|m1==m3|m2==m3|order<=0
        ka(n)=ka(n);
        kb(n)=kb(n);
        kc(n)=kc(n);
        kd(n)=kd(n);
         else

ka(n)=ka(n)+(mass^3)*chirala(points(:,m1,n),points(:,m2,n),points(:,m3
,n));
kb(n)=kb(n)+(mass^3)*chiralb(points(:,m1,n),points(:,m2,n),points(:,m3
,n));
kc(n)=kc(n)+(mass^3)*chiralc(points(:,m1,n),points(:,m2,n),points(:,m3
,n));
kd(n)=kd(n)+(mass^3)*chirald(points(:,m1,n),points(:,m2,n),points(:,m3
,n));


    end
   end
  end
 end
end


figure
 plot(Area,ka,'-.x',Area,kb,'-s',Area,kc,'r--
o',Area,kd,'b:d','MarkerSize',10,'LineWidth',3)
legend('1st model','2nd model','3rd model')
grid on
% xlabel('a1')
 xlabel('Area')
 ylabel('K')

 set(gca,'FontSize',26,'LineWidth',2)

 hold on
 figure
 plot(Area,kc,'-''LineWidth',3)
%
 xlabel('Area')
ylabel('K')
```

A-5) Matlab Codes to calculate Chirality index of a triangle with a constant area (Figure 6.8).

```matlab
%% calculate the chirality of triangles with constant area =1
%   by Huda Alzahrani 12/5/2018

p1=[0,0];
p2=[1,0];
x3=[-10:.5:10];
for n=1:length(x3);
p3(:,:,n)=[x3(n),2];
X(:,:,n)=[0,1,x3(n),0];
Y(:,:,n)=[0,0,2,0];

 points(:,:,n)=[X(:,:,n);Y(:,:,n)];
plot(points(1,:),points(2,:),'*r','MarkerSize',20);
 set(gca,'FontSize',26,'LineWidth',2)


Area(n) = polyarea(X(:,:,n),Y(:,:,n));%Area(of the riangle ABC)


      mass=1/length(points(1,:,1));
ka(n)=0;
kb(n)=0;
kc(n)=0;
kd(n)=0;
 for m1=1:length(points(1,:,n));
  for m2=1:length(points(1,:,n));
    for  m3=1:length(points(1,:,n));

      %         %clockwise condition
      x2x1=( points(1,m2,n)-
points(1,m1,n))*(points(2,m2,n)+points(2,m1,n));
      x3x2= (points(1,m3,n)-
points(1,m2,n))*(points(2,m3,n)+points(2,m2,n));
      x1x3=( points(1,m1,n)-
points(1,m3,n))*(points(2,m1,n)+points(2,m3,n));
      order=x2x1+x3x2+x1x3;
       if m1==m2|m1==m3|m2==m3|order<=0
      ka(n)=ka(n);
      kb(n)=kb(n);
      kc(n)=kc(n);
      kd(n)=kd(n);
       else

ka(n)=ka(n)+(mass^3)*chirala(points(:,m1,n),points(:,m2,n),points(:,m3
,n));
kb(n)=kb(n)+(mass^3)*chiralb(points(:,m1,n),points(:,m2,n),points(:,m3
,n));
kc(n)=kc(n)+(mass^3)*chiralc(points(:,m1,n),points(:,m2,n),points(:,m3
,n));
kd(n)=kd(n)+(mass^3)*chirald(points(:,m1,n),points(:,m2,n),points(:,m3
,n));


    end
```

```matlab
    end
   end
  end
 ka1(n)=5*ka(n);
kc1(n)=kc(n)/20;
kd1(n)=10*kd(n);
end
figure
plot(x3,ka1,'m-.x',x3,kb,'-s',x3,kc1,'r--
o',x3,kd1,'b:d','MarkerSize',10,'LineWidth',3)
legend('Osipov model','1st model','2nd model','3rd model')
title('Potts models')
grid on

 set(gca,'FontSize',26,'LineWidth',2)
xlabel('a1')
ylabel('K')

xlabel('x3')
```

A-6) Matlab Codes to calculate Mueller matrix (Figure 7-12).

```matlab
% % % Mueller Matrix %%%
% % % program to find m00, m01,m02, m03 %%%
% % % Huda Alzahrani 29/12/2020 %%%
clear all
format long g;
format compact;
fontSize = 20;

 %% Stokes parameters foe the air, the polariser at 0, 20, 40, 60, 80
I00=fitsread('I00.fits');
I02=fitsread('I02.fits');
I04=fitsread('I04.fits');
I06=fitsread('I06.fits');
I08=fitsread('I08.fits');
Q00=fitsread('Q00.fits');
Q02=fitsread('Q02.fits');
Q04=fitsread('Q04.fits');
Q06=fitsread('Q06.fits');
Q08=fitsread('Q08.fits');
U00=fitsread('U00.fits');
U02=fitsread('U02.fits');
U04=fitsread('U04.fits');
U06=fitsread('U06.fits');
U08=fitsread('U08.fits');
V00=fitsread('V00.fits');
V02=fitsread('V02.fits');
V04=fitsread('V04.fits');
V06=fitsread('V06.fits');
V08=fitsread('V08.fits');

  %% Stokes parameters foe the sample, the polariser at 0, 20, 40, 60,
80
Is0=fitsread('Is0.fits');
Is2=fitsread('Is2.fits');
Is4=fitsread('Is4.fits');
```

```matlab
Is6=fitsread('Is6.fits');
Is8=fitsread('Is8.fits');

 %% solving five equations to calculate four of Mueller elements
syms m00 m01 m02 m03

q1=Is0==m00*I00+m01*Q00+m02*U00+m03*V00;
q2=Is2==m00*I02+m01*Q02+m02*U02+m03*V02;
q3=Is4==m00*I04+m01*Q04+m02*U04+m03*V04;
q4=Is6==m00*I06+m01*Q06+m02*U06+m03*V06;
q5=Is8==m00*I08+m01*Q08+m02*U08+m03*V08;
Q=[q1 q2 q3 q4 q5];
S = solve(Q,[m00 m01 m02 m03],'ReturnConditions',true);
```

Appendix B

Calculation of Stokes parameters for dual photoelastic modulator polarimeter:

$$\begin{pmatrix} I' \\ Q' \\ U' \\ V' \end{pmatrix} = \begin{Bmatrix} m_{11} & m_{12} & m_{13} & m_{14} \\ m_{21} & m_{22} & m_{23} & m_{24} \\ m_{31} & m_{32} & m_{33} & m_{34} \\ m_{41} & m_{42} & m_{43} & m_{44} \end{Bmatrix} \begin{pmatrix} I \\ Q \\ U \\ V \end{pmatrix} = \begin{pmatrix} m_{11}I + m_{12}Q + m_{13}U + m_{14}V \\ m_{21}I + m_{22}Q + m_{23}U + m_{24}V \\ m_{31}I + m_{32}Q + m_{33}U + m_{34}V \\ m_{41}I + m_{42}Q + m_{43}U + m_{44}V \end{pmatrix}$$

$$M_{PEM1} = \begin{Bmatrix} 1 & 0 & 0 & 0 \\ 0 & cos(4\alpha)\,sin^2\left(\frac{\delta_1}{2}\right) + cos^2\left(\frac{\delta_1}{2}\right) & sin(4\alpha)sin^2\left(\frac{\delta_1}{2}\right) & -sin(2\alpha)\,sin\,(\delta_1) \\ 0 & sin(4\alpha)sin^2\left(\frac{\delta_1}{2}\right) & -cos(4\alpha)\,sin^2\left(\frac{\delta_1}{2}\right) + cos^2\left(\frac{\delta_1}{2}\right) & cos(2\alpha)\,sin\,(\delta_1) \\ 0 & sin(2\alpha)\,sin\,(\delta_1) & -cos(2\alpha)\,sin\,(\delta_1) & cos\,(\delta_1) \end{Bmatrix}$$

$$M_{PEM2} = \begin{Bmatrix} 1 & 0 & 0 & 0 \\ 0 & 1 & 0 & 0 \\ 0 & 0 & cos(\delta_2) & sin\,(\delta_2) \\ 0 & 0 & -sin\,(\delta_2) & cos\,(\delta_2) \end{Bmatrix}$$

$$M_{analyser} = \frac{1}{2}\begin{Bmatrix} 1 & cos(2\beta) & sin(2\beta) & 0 \\ cos(2\beta) & cos^2(2\beta) & cos(2\beta)\,sin(2\beta) & 0 \\ sin(2\beta) & cos(2\beta)\,sin(2\beta) & sin^2(2\beta) & 0 \\ 0 & 0 & 0 & 0 \end{Bmatrix}$$

$$M_A M_{PEM2} = \frac{1}{2}$$

$$\begin{Bmatrix} 1 & cos(2\beta) & sin(2\beta) & 0 \\ cos(2\beta) & cos^2(2\beta) & cos(2\beta)\,sin(2\beta) & 0 \\ sin(2\beta) & cos(2\beta)\,sin(2\beta) & sin^2(2\beta) & 0 \\ 0 & 0 & 0 & 0 \end{Bmatrix}\begin{pmatrix} 1 & 0 & 0 & 0 \\ 0 & 1 & 0 & 0 \\ 0 & 0 & cos(\delta_2) & sin(\delta_2) \\ 0 & 0 & -sin(\delta_2) & cos(\delta_2) \end{pmatrix}$$

$$= \frac{1}{2}\begin{Bmatrix} 1 & cos(2\beta) & sin(2\beta)\,cos(\delta_2) & sin(2\beta)\,sin(\delta_2) \\ cos(2\beta) & cos^2(2\beta) & cos(2\beta)\,sin(2\beta)\,cos(\delta_2) & cos(2\beta)\,sin(2\beta)\,sin(\delta_2) \\ sin(2\beta) & cos(2\beta)\,sin(2\beta) & sin^2(2\beta)\,cos(\delta_2) & sin^2(2\beta)sin(\delta_2) \\ 0 & 0 & 0 & 0 \end{Bmatrix}$$

$$M_A M_{PEM2} M_{PEM1} =$$

$$= \frac{1}{2}\begin{Bmatrix} 1 & cos(2\beta) & sin(2\beta)\,cos(\delta_2) & sin(2\beta)\,sin(\delta_2) \\ cos(2\beta) & cos^2(2\beta) & cos(2\beta)\,sin(2\beta)\,cos(\delta_2) & cos(2\beta)\,sin(2\beta)\,sin(\delta_2) \\ sin(2\beta) & cos(2\beta)\,sin(2\beta) & sin^2(2\beta)\,cos(\delta_2) & sin^2(2\beta)sin(\delta_2) \\ 0 & 0 & 0 & 0 \end{Bmatrix}$$
$$\begin{pmatrix} 1 & 0 & 0 & 0 \\ 0 & cos(4\alpha)\,sin^2\left(\frac{\delta_1}{2}\right)+cos^2\left(\frac{\delta_1}{2}\right) & sin(4\alpha)sin^2\left(\frac{\delta_1}{2}\right) & -sin(2\alpha)\,sin(\delta_1) \\ 0 & sin(4\alpha)sin^2\left(\frac{\delta_1}{2}\right) & -cos(4\alpha)\,sin^2\left(\frac{\delta_1}{2}\right)+cos^2\left(\frac{\delta_1}{2}\right) & cos(2\alpha)\,sin(\delta_1) \\ 0 & sin(2\alpha)\,sin(\delta_1) & -cos(2\alpha)\,sin(\delta_1) & cos(\delta_1) \end{pmatrix}$$

$$= \begin{Bmatrix} m_{11} & m_{12} & m_{13} & m_{14} \\ m_{21} & m_{22} & m_{23} & m_{24} \\ m_{31} & m_{32} & m_{33} & m_{34} \\ m_{41} & m_{42} & m_{43} & m_{44} \end{Bmatrix}$$

By using the following trigonometric functions:

$$cos^2(a) = \frac{1 + \cos{(2a)}}{2}$$

$$\sin(2a) = 2\sin(a)\cos{(a)}$$

$$\cos(2a) = \cos^2(a) - sin^2{(a)}$$

$$\sin(a \pm b) = \sin(a)\cos{(b)} \pm \cos(a)\sin(b)$$

$$\cos(a \pm b) = \cos(a)\cos{(b)} \mp \sin(a)\sin(b)$$

$$\cos[x\sin(a)] = J_0(x) + 2\sum_{n=1}^{\infty} J_{2n}(x)\cos(2na)$$

$$\sin[x\sin(a)] = 2\sum_{n=0}^{\infty} J_{2n+1}(x)\cos\big((2n+1)a\big)$$

$$m_{11} = 1$$

$$m_{12} = \cos(2\beta)\left[\cos(4\alpha)\sin^2\left(\frac{\delta_1}{2}\right) + \cos^2\left(\frac{\delta_1}{2}\right)\right] + \sin(2\beta)\,cos(\delta_2)\sin(4\alpha)\sin^2\left(\frac{\delta_1}{2}\right) + \sin(2\beta)\sin(\delta_2)\sin(2\alpha)\sin(\delta_1)$$

$$= \cos(2\beta)\,[\cos^2(2\alpha) - \sin^2(2\alpha)]\left[\frac{1}{2} - \frac{1}{2}cos(\delta_1)\right] + \cos(2\beta)\left[\frac{1}{2} + \frac{1}{2}cos(\delta_1)\right] + 2\sin(2\beta)\,cos(\delta_2)\sin(2\alpha)\,cos(2\alpha)\left[\frac{1}{2} - \frac{1}{2}cos(\delta_1)\right]$$
$$+ \sin(2\beta)\,sin\,(\delta_2)\sin(2\alpha)\sin{(\delta_1)}$$

$$= \frac{1}{2}\cos(2\beta)cos^2(2\alpha) - \frac{1}{2}\cos(2\beta)\sin^2(2\alpha) - \frac{1}{2}\cos(2\beta)\cos^2(2\alpha)cos(\delta_1) + \frac{1}{2}\cos(2\beta)\sin^2(2\alpha)cos(\delta_1) + \frac{1}{2}\cos(2\beta) + \frac{1}{2}\cos(2\beta)cos(\delta_1)$$
$$+ \sin(2\beta)\,cos(\delta_2)\sin(2\alpha)\,cos(2\alpha) - \sin(2\beta)\,cos(\delta_2)\sin(2\alpha)\,cos(2\alpha)\,cos(\delta_1) + \sin(2\beta)\,sin\,(\delta_2)\sin(2\alpha)\sin{(\delta_1)}$$

$$= \frac{1}{2}\cos(2\beta)\cos^2(2\alpha) - \frac{1}{2}\cos(2\beta)[1 - \cos^2(2\alpha)] + \frac{1}{2}\cos(2\beta) - \frac{1}{2}\cos(2\beta)[1 - \sin^2(2\alpha)]\cos(\delta_1) + \frac{1}{2}\cos(2\beta)\sin^2(2\alpha)\cos(\delta_1)$$

$$+ \frac{1}{2}\cos(2\beta)\cos(\delta_1) + \sin(2\beta)\sin(2\alpha)\cos(2\alpha)\cos(\delta_2) - \sin(2\beta)\sin(2\alpha)\,[\,\cos(2\alpha)\cos(\delta_1)\cos(\delta_2) - \sin(\delta_1)\sin(\delta_2)\,]$$

$$= \cos(2\beta)\cos^2(2\alpha) - \cos(2\beta)\,\sin^2(2\alpha)\cos(\delta_1)$$
$$+ \sin(2\beta)\sin(2\alpha)\cos(2\alpha)\cos(\delta_2) - \sin(2\beta)\sin(2\alpha)\,[\,\cos(2\alpha)\cos(\delta_1)\cos(\delta_2) - \sin(\delta_1)\sin(\delta_2)\,]$$

$$= \cos(2\beta)\cos^2(2\alpha) - \cos(2\beta)\,\sin^2(2\alpha)\left[J_0(\delta_{10}) + 2\sum_{n=1}^{\infty} J_{2n}(\delta_{10})\cos(2n\Omega_{10}t)\right]$$

$$+ \sin(2\beta)\sin(2\alpha)\cos(2\alpha)\left[J_0(\delta_{20}) + 2\sum_{n=1}^{\infty} J_{2n}(\delta_{20})\cos(2n\Omega_{20}t)\right]$$

$$- \sin(2\beta)\sin(2\alpha)\left[\cos(2\alpha)\left[J_0(\delta_{10}) + 2\sum_{n=1}^{\infty} J_{2n}(\delta_{10})\cos(2n\Omega_{10}t)\right]\left[J_0(\delta_{20}) + 2\sum_{n=1}^{\infty} J_{2n}(\delta_{20})\cos(2n\Omega_{20}t)\right]\right.$$

$$\left. - \left[2\sum_{n=1}^{\infty} J_{2n+1}(\delta_{10})\cos\big((2n+1)\Omega_{10}t\big)\right]\left[2\sum_{n=1}^{\infty} J_{2n+1}(\delta_{20})\cos\big((2n+1)\Omega_{20}t\big)\right]\right]$$

$$= \cos(2\beta)\cos^2(2\alpha) - \cos(2\beta)\,\sin^2(2\alpha)J_0(\delta_{10}) - 2\cos(2\beta)\sin^2(2\alpha)\sum_{n=1}^{\infty} J_{2n}(\delta_{10})\,\cos(2n\Omega_1 t)$$

$$+ \sin(2\beta)\sin(2\alpha)\,\cos(2\alpha)J_0(\delta_{20}) + 2\sin(2\beta)\sin(2\alpha)\cos(2\alpha)\sum_{n=1}^{\infty} J_{2n}(\delta_{20})\,\cos(2n\Omega_2 t)$$

$$- \sin(2\beta)\sin(2\alpha)\,\cos(2\alpha)J_0(\delta_{10})J_0(\delta_{20}) - 2\sin(2\beta)\sin(2\alpha)\,\cos(2\alpha)J_0(\delta_{10})\sum_{n=1}^{\infty} J_{2n}(\delta_{20})\,\cos(2n\Omega_2 t)$$

$$- 2\sin(2\beta)\sin(2\alpha)\,\cos(2\alpha)J_0(\delta_{20})\sum_{n=1}^{\infty} J_{2n}(\delta_{10})\,\cos(2n\Omega_1 t)$$

$$- 4\sin(2\beta)\sin(2\alpha)\,\cos(2\alpha)\sum_{n=1}^{\infty} J_{2n}(\delta_{10})\,\cos(2n\Omega_1 t)\sum_{n=1}^{\infty} J_{2n}(\delta_{20})\,\cos(2n\Omega_2 t)$$

$$- 4\sin(2\beta)\sin(2\alpha)\sum_{n=0}^{\infty} J_{2n+1}(\delta_{10})\,\cos\big((2n+1)\Omega_1 t\big)\sum_{n=1}^{\infty} J_{2n+1}(\delta_{20})\,\cos\big((2n+1)\Omega_2 t\big)$$

$$= \cos^2(2\alpha)\cos(2\beta) - \sin^2(2\alpha)\,\cos(2\beta)J_0(\delta_{10}) + \sin(2\alpha)\sin(2\beta)\,\cos(2\alpha)J_0(\delta_{20}) - \cos(2\alpha)\sin(2\beta)\sin(2\alpha)J_0(\delta_{10})J_0(\delta_{20})$$

$$+ 2\sin(2\alpha)\sin(2\beta)\,[1 - J_0(\delta_{10})]\cos(2\alpha)\sum_{n=1}^{\infty} J_{2n}(\delta_{20})\,\cos(2n\Omega_2 t)$$

$$+ 2[-\sin^2(2\alpha)\cos(2\beta)$$

$$+ \sin(2\alpha)\cos(2\alpha)\sin(2\beta)\,J_0(\delta_{20})]\sum_{n=1}^{\infty} J_{2n}(\delta_{10})\,\cos(2n\Omega_1 t) - 4\sin(2\beta)\sin(2\alpha)\sum_{n=0}^{\infty} J_{2n+1}(\delta_{10})\,\cos\big((2n+1)\Omega_1 t\big)\sum_{n=1}^{\infty} J_{2n+1}(\delta_{20})\,\cos\big((2n$$

$$+1)\Omega_2 t\big) - 4\sin(2\beta)\sin(2\alpha)\,\cos(2\alpha)\sum_{n=1}^{\infty} J_{2n}(\delta_{10})\,\cos(2n\Omega_1 t)\sum_{n=1}^{\infty} J_{2n}(\delta_{20})\,\cos(2n\Omega_2 t) - \sum_{n=1}^{\infty} J_{2n}(\delta_{10})\,\cos(2n\Omega_1 t)$$

$$m_{13} = \cos(2\beta)\sin(4\alpha)\sin^2\left(\frac{\delta_1}{2}\right) + \sin(2\beta)\cos(\delta_2)\left[-\cos(4\alpha)\sin^2\left(\frac{\delta_1}{2}\right) + \cos^2\left(\frac{\delta_1}{2}\right)\right] - \sin(2\beta)\sin(\delta_2)\cos(2\alpha)\sin(\delta_1)$$

$$= 2\cos(2\beta)\sin(2\alpha)\cos(2\alpha)\left[\frac{1}{2} - \frac{1}{2}\cos(\delta_1)\right] - \sin(2\beta)\cos(\delta_2)\left[\cos^2(2\alpha) - \sin^2(2\alpha)\right]\left[\frac{1}{2} - \frac{1}{2}\cos(\delta_1)\right] + \sin(2\beta)\cos(\delta_2)\left[\frac{1}{2} + \frac{1}{2}\cos(\delta_1)\right]$$
$$- \sin(2\beta)\sin(\delta_2)\sin(2\alpha)\sin(\delta_1)$$

$$= \cos(2\beta)\sin(2\alpha)\cos(2\alpha)$$
$$- \cos(2\beta)\sin(2\alpha)\cos(2\alpha)\cos(\delta_1) - \frac{1}{2}\sin(2\beta)\cos^2(2\alpha)\cos(\delta_2)$$
$$+ \frac{1}{2}\sin(2\beta)\cos^2(2\alpha)\cos(\delta_1)\cos(\delta_2) + \frac{1}{2}\sin(2\beta)\sin^2(2\alpha)\cos(\delta_1)\cos(\delta_2) - \frac{1}{2}\sin(2\beta)\sin^2(2\alpha)\cos(\delta_1)\cos(\delta_2)$$
$$+ \frac{1}{2}\sin(2\beta)\cos(\delta_2) + \frac{1}{2}\sin(2\beta)\cos(\delta_1)\cos(\delta_2) - \sin(2\beta)\sin(2\alpha)\sin(\delta_1)\sin(\delta_2)$$

$$= \cos(2\beta)\sin(2\alpha)\cos(2\alpha) - \cos(2\beta)\sin(2\alpha)\cos(2\alpha)\cos(\delta_1)$$
$$+ \frac{1}{2}\sin(2\beta)\cos(\delta_2)[1 - \cos^2(2\alpha)] + \frac{1}{2}\sin(2\beta)\cos^2(2\alpha)\cos(\delta_1)\cos(\delta_2) - \sin(2\beta)\sin(2\alpha)\sin(\delta_1)\sin(\delta_2)$$

$$= \cos(2\beta)\sin(2\alpha)\cos(2\alpha) - \cos(2\beta)\sin(2\alpha)\cos(2\alpha)\left[J_0(\delta_{10}) + 2\sum_{n=1}^{\infty} J_{2n}(\delta_{10})\cos(2n\Omega_1 t)\right]$$

$$+ \frac{1}{2}\sin(2\beta)\sin^2(2\alpha)\left[J_0(\delta_{20}) + 2\sum_{n=1}^{\infty} J_{2n}(\delta_{20})\cos(2n\Omega_2 t)\right]$$

$$+ \frac{1}{2}\sin(2\beta)\cos^2(2\alpha)\left[J_0(\delta_{10}) + 2\sum_{n=1}^{\infty} J_{2n}(\delta_{10})\cos(2n\Omega_1 t)\right]\left[J_0(\delta_{20}) + 2\sum_{n=1}^{\infty} J_{2n}(\delta_{20})\cos(2n\Omega_2 t)\right] - 4\sin(2\beta)\sin(2\alpha)\sum_{n=0}^{\infty} J_{2n+1}(\delta_{10})\cos\big((2n$$

$$+ 1)\Omega_1 t\big)\sum_{n=0}^{\infty} J_{2n+1}(\delta_{20})\cos\big((2n+1)\Omega_2 t\big)$$

103

$$= sin(2\alpha)cos(2\alpha)cos(2\beta) - sin(2\alpha)cos(2\beta)\ cos(2\alpha)J_0(\delta_{10})$$

$$+ \frac{1}{2}\ sin^2(2\alpha)sin(2\beta)J_0(\delta_{20})$$

$$+ \frac{1}{2}sin(2\beta)cos^2(2\alpha)J_0(\delta_{10})J_0(\delta_{20})$$

$$+ [\ sin^2(2\alpha)$$

$$+ cos^2(2\alpha)J_0(\delta_{10})]\ sin(2\beta)\sum_{n=1}^{\infty} J_{2n}(\delta_{20})\ cos(2n\Omega_2 t) + [-2sin(2\alpha)\ cos(2\beta)cos(2\alpha) + sin(2\beta)cos^2(2\alpha)\ J_0(\delta_{20})] \sum_{n=1}^{\infty} J_{2n}(\delta_{10})\ cos(2n\Omega_1 t)J_0(\delta_{10})$$

$$+ 2\ sin(2\beta)cos^2(2\alpha) \sum_{n=1}^{\infty} J_{2n}(\delta_{10})\ cos(2n\Omega_1 t) \sum_{n=1}^{\infty} J_{2n}(\delta_{20})\ cos(2n\Omega_2 t)$$

$$-4\ sin(2\beta)sin(2\alpha) \sum_{n=0}^{\infty} J_{2n+1}(\delta_{10})\ cos\big((2n+1)\Omega_1 t\big) \sum_{n=0}^{\infty} J_{2n+1}(\delta_{20})\ cos\big((2n+1)\Omega_2 t\big)$$

$$m_{14} = -\cos(2\beta)\ sin(2\alpha)\ sin(\delta_1) + sin(2\beta)\ cos(\delta_2)\ cos(2\alpha)\ sin(\delta_1) + sin(2\beta)\ sin(\delta_2)cos(\delta_1)$$

$$= -2\cos(2\beta)\ sin(2\alpha) \sum_{n=0}^{\infty} J_{2n+1}(\delta_{10})\ cos\big((2n$$

$$+ 1)\Omega_1 t\big)\ + 2\ sin(2\beta)\ cos(2\alpha) \sum_{n=0}^{\infty} J_{2n+1}(\delta_{10})\ cos\big((2n$$

$$+ 1)\Omega_1 t\big) \left[J_0(\delta_{20}) + 2\sum_{n=1}^{\infty} J_{2n}(\delta_{20})\ cos(2n\Omega_2 t)\right] + 2\ sin(2\beta) \sum_{n=0}^{\infty} J_{2n+1}(\delta_{20})\ cos\big((2n+1)\Omega_2 t\big) \left[J_0(\delta_{10})\right.$$

$$\left. + 2\sum_{n=1}^{\infty} J_{2n}(\delta_{10})\ cos(2n\Omega_1 t)\right]$$

$$= 2\sin(2\beta)\ J_0(\delta_{10}) \sum_{n=0}^{\infty} J_{2n+1}(\delta_{20})\ cos\big((2n+1)\Omega_2 t\big) + 2cos(2\alpha)\sin(2\beta)J_0(\delta_{20}) \sum_{n=0}^{\infty} J_{2n+1}(\delta_{10})\ cos\big((2n+1)\Omega_1 t\big) - 2\cos(2\beta)\ sin(2\alpha) \sum_{n=1}^{\infty} J_{2n}(\delta_{10})\ cos\ (2n\Omega_1 t)$$

$$+ 2\sin(2\beta)\cos(2\alpha) \sum_{n=0}^{\infty} J_{2n+1}(\delta_{10})\ cos\big((2n+1)\Omega_1 t\big) + 2sin(2\beta) \sum_{n=0}^{\infty} J_{2n+1}(\delta_{20})\ cos\big((2n+1)\Omega_2 t\big) \sum_{n=1}^{\infty} J_{2n}(\delta_{10})\ cos(2n\Omega_1 t)$$

$$I' = \frac{1}{2}[m_{11}I + m_{12}Q + m_{13}U + m_{14}V]$$

To simplify this equation the retardation amplitudes of the PEMs set where satisfy the condition:

$$J_0(\delta_{10}) = J_0(\delta_{20}) = 0$$

m_{12}

$$= \cos^2(2\alpha)\cos(2\beta) \quad +2\sin(2\alpha)\sin(2\beta)\ cos(2\alpha) \sum_{n=1}^{\infty} J_{2n}(\delta_{20})\ cos(2n\Omega_2 t)$$

$$+ 2[-\sin^2(2\alpha)cos(2\beta)] \sum_{n=1}^{\infty} J_{2n}(\delta_{10})\ cos(2n\Omega_1 t) - 4\sin(2\beta)\sin(2\alpha) \sum_{n=0}^{\infty} J_{2n+1}(\delta_{10})\ cos\big((2n+1)\Omega_1 t\big) \sum_{n=0}^{\infty} J_{2n+1}(\delta_{20})\ cos\ \big((2n$$

$$+ 1)\Omega_2 t\big) - 4\sin(2\beta)\sin(2\alpha)\ cos(2\alpha) \sum_{n=1}^{\infty} J_{2n}(\delta_{10})\ cos(2n\Omega_1 t) \sum_{n=1}^{\infty} J_{2n}(\delta_{20})\ cos(2n\Omega_2 t) - \sum_{n=1}^{\infty} J_{2n}(\delta_{10})\ cos(2n\Omega_1 t)$$

$$= \cos(2\beta)\cos^2(2\alpha) - \cos(2\beta)\,\sin^2(2\alpha)\left[2\sum_{n=1}^{\infty} J_{2n}(\delta_{10})\,\cos(2n\Omega_{10}t)\right]$$

$$+ \sin(2\beta)\sin(2\alpha)\,\cos(2\alpha)\left[2\sum_{n=1}^{\infty} J_{2n}(\delta_{20})\,\cos(2n\Omega_{20}t)\right]$$

$$- \sin(2\beta)\sin(2\alpha)\left[\cos(2\alpha)\left[2\sum_{n=1}^{\infty} J_{2n}(\delta_{10})\,\cos(2n\Omega_{10}t)\right]\left[2\sum_{n=1}^{\infty} J_{2n}(\delta_{20})\,\cos(2n\Omega_{20}t)\right]\right.$$

$$\left. - \left[2\sum_{n=1}^{\infty} J_{2n+1}(\delta_{10})\,\cos\big((2n+1)\Omega_{10}t\big)\right]\left[2\sum_{n=1}^{\infty} J_{2n+1}(\delta_{20})\,\cos\big((2n+1)\Omega_{20}t\big)\right]\right]$$

And rewrite the equation as four sub-equations:

$$I_{DC} = g_1 I + g_2 Q + g_3 U$$

$$I_{QU1} = g_4 Q + g_5 U$$

$$I_{QU2} = g_6 Q + g_7 U$$

$$I_V = g_8 V$$

7The four sub-equations could be rewritten in matrix form as (Guan *et al.*, 2010):

$$\begin{pmatrix} I_{DC} \\ I_{QU1} \\ I_{QU2} \\ I_V \end{pmatrix} = \begin{pmatrix} g_1 & g_2 & g_3 & 0 \\ 0 & g_4 & g_5 & 0 \\ 0 & g_6 & g_7 & 0 \\ 0 & 0 & 0 & g_8 \end{pmatrix} \begin{pmatrix} I \\ Q \\ U \\ V \end{pmatrix}$$

Where I_{DC}, I_{QU1}, I_{QU2}, and I_V are four different signals that can be measured experimentally by using different lock-in amplifiers, while g_i (i=1, 2, …..8) are constants dependent on the retardation of the two photoelastic modulators, and also the angles between PEM2 and both PEM1 and the analyser (α and β) (Guan *et al.*, 2010).

The Stokes parameters of the entering polarised light can be obtained by calculating the matrix inversion, as follows:

$$\begin{pmatrix} I \\ Q \\ U \\ V \end{pmatrix} = \begin{pmatrix} k_1 & 0 & 0 & 0 \\ k_2 & k_3 & k_4 & 0 \\ k_5 & k_6 & k_7 & 0 \\ 0 & 0 & 0 & k_8 \end{pmatrix} \begin{pmatrix} I_{DC} \\ I_{QU1} \\ I_{QU2} \\ I_V \end{pmatrix}$$

Where k_i (i=1, 2, …..8) are eight constants related to g_i, which are could be determined experimentally through the calibration process.

The inverse matrix of the matrix *A* has the following expression:

$$A^{-1} = \frac{1}{|A|} \tilde{A}$$

Where |A/ is the determinant and Ă is the adjugate matrix. The matrix is invertible if the determinant does not equal zero. So, the determinant of K matrix should not equal zero:

Appendix C

Conference Contributions:

1) (poster) H. A. Alzahrani. "Optical Activity in Nanosize Planar Chiral Metamaterials". *Methods Fair 2017 photograph competition*. Manchester – 1 November 2017

2) (poster) H. A. Alzahrani. "Optical Activity by Nanostructure Planar Chiral Metamaterials". *10th Man Met Postgraduate Research Conference (MMUPGC18)*, Manchester, UK, 7 March 2018.

3) (poster) H. A. Alzahrani. "Nanostructure Planar Chiral Metamaterials". *Salford Postgraduate Research Conference (SPARC18)*, Manchester, UK, 4-5 July 2018.

4) (poster) H. A. Alzahrani. "A Study on Chirality and Optical Response in Planar Chiral Metamaterials". *The 2018 MMU Science and Engineering Research Conference (MMUPGC18)*, Manchester, UK, 13 September 2018.

5) (poster) H. A. Alzahrani. "Optical Response by Nanostructure Planar Chiral Metamaterials". *11th Man Met Postgraduate Research Conference (MMUPGC19)*, Manchester, UK, 6 March 2019.

6) (awarded-winning poster) H. A. Alzahrani, T. H. Shen. "Chirality and Optical Activity of 2D Chiral Metamaterials". *Photonic and Optoelectronic Materials (POEM2019)*, London, UK, 9-12 April 2019.

7) (oral) H. A. Alzahrani. "A Study of Chirality by Stokes Polarimetric Light Microscope". *Microscience Microscopy Congress (mmc2019)*, Manchester, UK, 1-4 July 2019.

8) (poster) H. A. Alzahrani, T. H. Shen, J. L. Angulo. "A Study of Chirality by Stokes Polarimetric Light Microscope". *Microscience Microscopy Congress (mmc2019)*, Manchester, UK, 1-4 July 2019.